OF **COLLEGE**
ENGINEERING

VPI-E-79-36 December, 1979

NONLINEAR TEMPERATURE DEPENDENT FAILURE ANALYSIS OF FINITE WIDTH COMPOSITE LAMINATES

Aniruddha P. Nagarkar[1]
Carl T. Herakovich[2]

VIRGINIA POLYTECHNIC INSTITUTE AND STATE UNIVERSITY

BLACKSBURG, VIRGINIA

College of Engineering
Virginia Polytechnic Institute and State University
Blacksburg, Virginia 24061

VPI-E-79-36 December, 1979

NONLINEAR TEMPERATURE DEPENDENT FAILURE ANALYSIS OF FINITE WIDTH COMPOSITE LAMINATES

Aniruddha P. Nagarkar[1]
Carl T. Herakovich[2]

Department of Engineering Science and Mechanics

NASA Grant NGR-1250 - Final Report

N80-22409#

Prepared for: Materials Application Branch
National Aeronautics & Space Administration
Langley Research Center
Hampton, Virginia 23665

[1]Graduate Student - Virginia Tech (presently at Material Sciences Corp.)
[2]Professor of Engineering Science and Mechanics - Virginia Tech

SECURITY CLASSIFICATION OF THIS PAGE *(When Data Entered)*

REPORT DOCUMENTATION PAGE

READ INSTRUCTIONS BEFORE COMPLETING FORM

1 REPORT NUMBER: VPI-E-79-36	2. GOVT ACCESSION NO.
3 RECIPIENT'S CATALOG NUMBER	
4 TITLE *(and Subtitle)*: NONLINEAR TEMPERATURE DEPENDENT FAILURE ANALYSIS OF FINITE WIDTH COMPOSITE LAMINATES	5 TYPE OF REPORT & PERIOD COVERED
	6. PERFORMING ORG. REPORT NUMBER: VPI-E-79-36
7. AUTHOR(s): Aniruddha P. Nagarkar and Carl T. Herakovich	8. CONTRACT OR GRANT NUMBER(s): NASA Grant NGR-1250
9 PERFORMING ORGANIZATION NAME AND ADDRESS: Virginia Polytechnic Institute & State University, Engineering Science and Mechanics, Blacksburg, Virginia 24061	10 PROGRAM ELEMENT, PROJECT, TASK AREA & WORK UNIT NUMBERS
11 CONTROLLING OFFICE NAME AND ADDRESS: National Aeronautics & Space Administration, Langley Research Center, Hampton, Virginia 23665	12 REPORT DATE: December, 1979
	13 NUMBER OF PAGES
14 MONITORING AGENCY NAME & ADDRESS *(if different from Controlling Office)*: Virginia Polytechnic Institute & State University, Engineering Science & Mechanics, Blacksburg, Virginia 24061	15 SECURITY CLASS *(of this report)*: unclassified
	15a DECLASSIFICATION/DOWNGRADING SCHEDULE

16 DISTRIBUTION STATEMENT *(of this Report)*

Approved for public release, distribution unlimited

17 DISTRIBUTION STATEMENT *(of the abstract entered in Block 20, if different from Report)*

Approved for public release, distribution unlimited

18 SUPPLEMENTARY NOTES

19 KEY WORDS *(Continue on reverse side if necessary and identify by block number)*

composites, edge effects, nonlinear behavior, thermal stresses, failure, finite elements

20 ABSTRACT *(Continue on reverse side if necessary and identify by block number)*

See page iv

DD FORM 1 JAN 73 1473 EDITION OF 1 NOV 65 IS OBSOLETE

SECURITY CLASSIFICATION OF THIS PAGE *(When Data Entered)*

FORWARD

This final report for NASA Grant NGR-1250 represents technical progress made during the period September, 1978 through December, 1979. Mr. Jerry Deaton of NASA Langley served as the technical monitor. The authors would also like to acknowledge Ms. Fran Carter for her overall assistance in the preparation of this report.

NONLINEAR TEMPERATURE DEPENDENT FAILURE ANALYSIS
OF FINITE WIDTH COMPOSITE LAMINATES

ABSTRACT

A quasi-three dimensional, nonlinear elastic finite element stress analysis of finite width composite laminates including curing stresses is presented.

Cross-ply, angle-ply, and two quasi-isotropic graphite/epoxy laminates are studied. Curing stresses are calculated using temperature dependent elastic properties that are input as percent retention curves, and stresses due to mechanical loading in the form of an axial strain are calculated using tangent moduli obtained by Ramberg-Osgood parameters. It is shown that curing stresses and stresses due to tensile loading are significant as edge effects in all types of laminate studies.

The tensor polynomial failure criterion is used to predict the initiation of failure. The mode of failure is predicted by examining individual stress contributions to the tensor polynomial. Failure is predicted to always initiate at the free edge, but not always at ply interfaces. The location and mode of failure is shown to be laminate dependent.

TABLE OF CONTENTS

LIST OF TABLES

LIST OF FIGURES

1. INTRODUCTION

The fabrication of laminated fibrous composites involves curing the fiber-matrix system at an elevated temperature. Cure temperatures for resin matrix systems vary from 350°F for epoxies to 650°F for polyimides. The mismatch of thermal expansion coefficients between fiber and matrix (or, alternatively, the orthotropic properties of the lamina) coupled with the large temperature drop from the maximum cure temperature can result in relatively high residual curing stresses in laminates at room temperature. These thermal stresses are often large enough to cause transverse microcracking or ply delamination prior to the application of mechanical load. Residual thermal stresses are also present in metal matrix composites such as boron-aluminum, in which their effect is manifested as yielding of the matrix material.

The development of residual stresses in composites does not have a direct counterpart in homogeneous, isotropic media and there are relatively few studies of the subject reported in the literature. All the studies are based upon the assumption that the total strain is the sum of two distinct parts: the mechanical strain which is related to the stresses through the constitutive equation, and the "free" thermal strain which, in itself, does not cause stress in the laminate.

The purpose of this study is to analyze the thermo-mechanical response of resin matrix composites and to predict the occurrence and mode of first failure in finite width laminates. Previous researchers have proposed various methods for calculating residual stresses, and there have been a few studies of stress-strain response to mechanical

load which included residual stresses. Most previous studies typically perform the residual thermal analysis and the mechanical load analysis separately assuming linear elastic behavior. The principal of superposition is used to predict the combined effect of mechanical load and curing stresses. The present study treats the thermal and mechanical behavior separately, but does not make the assumption of linear elasticity. The residual stress field therefore cannot be superposed on the mechanical load, but is used as an initial condition. Special attention is given to the influence of edge effects on the stress field and the occurrence of first failure.

The finite element program NONCOM2 [1,2,3] was modified for this analysis. The efficiency and capability of the program were increased so as to handle a larger number of nodes (with a choice for an in-core or an out-of-core equation solver) and a detailed failure analysis using the tensor polynomial failure criterion for predicting first failure. The modified program is designated NONCOM3. Results were obtained for cross-ply, angle-ply and quasi-isotropic laminates of T300/5208 graphite epoxy.

2. LITERATURE REVIEW

Most previous theoretical studies are lamination theory solutions. They are based upon the classical plate theory assumptions and, therefore, valid only in interior regions away from the free edges of finite width laminates; they yield only laminate stresses. However, failure in laminates is often observed to initiate at the free edges [4,5] and, therefore, the stress distribution there is of paramount interest. The importance of edge effect during thermal loading of graphite-polyimide was clearly demonstrated by Herakovich, Mills and Davis [5].

Tsai [6] presented a thermoelastic formulation for calculating laminate thermal stresses in 1965. This study presents the basic lamination theory development for calculating residual stresses. A micromechanical procedure for calculating residual thermal stresses was outlined by Hashin [7]. One of the earlier reported analytical predictions of residual stresses using lamination theory is a study by Chamis [8], in which he analyzed laminates of different material systems, stacking sequences and fiber volume fractions. Extensive experimental studies were conducted at the IIT Research Center by Daniel and Liber [9]. They reported thermal stresses based upon measured strains and temperature dependent constitutive relations.

Herakovich [10] was apparently the first to consider thermal edge effects in composites. He analyzed laminates of boron-epoxy and aluminum using finite elements, and considered stress distributions due to thermal and mechanical loads. The analysis included interlaminar

stresses but was linear elastic with constant room temperature properties. A nonlinear elastic finite element analysis, which included thermal effects and temperature dependent properties was conducted by Renieri and Herakovich [1], but residual stress predictions formed only a limited part of the study and the finite element mesh used was quite coarse. Their basic formulation will be used in the present analysis with a much finer mesh, an improved equation solver and a failure criterion added to the analysis capability.

Hahn and Pagano [11] pointed out the necessity for the inclusion of terms corresponding to the stress and temperature dependence of properties. They developed a 'total strain' theory, in which the strains and stresses are calculated using temperature dependent elastic properties at the temperature of interest.

Daniel, Liber and Chamis [12] developed a technique to measure residual strain by embedding strain gages between plies in laminates. They used this technique for measuring curing strains in boron/epoxy and S glass/epoxy, and calculated stresses using temperature dependent constitutive relations. Thermal cycling suggested that residual stresses during the curing process were primarily due to thermal mismatch between adjacent plies.

Chamis and Sullivan [13] outlined a procedure for nonlinear analysis of laminates with residual thermal stresses. The laminate was loaded in increments, using stresses calculated in the most recent load step to calculate elastic moduli for the next load step. Micromechanics was used to predict lamina properties, which were used in the lamination

theory analysis.

Hahn [14] concluded that the stress free temperature in laminates is lower than the cure temperature. The method outlined in [11] was used to calculate residual strains which were compared to experimentally determined strains. Daniel and Liber [15] investigated the effect of stacking sequence on residual stresses in graphite/polyimide laminates. The strains were determined experimentally, and the stresses, calculated using constitutive relations, were found to be close to the transverse strength.

Wang and Crossman [16] studied edge effects due to thermal loading on some specific laminates. They predict a peculiar behavior for a $[\pm 45]_s$ laminate, with the existence of 'stiff' tensile and 'soft' compressive zones in the laminate.

A report by Chamis [17] summarized work done at the NASA Lewis Research Center on angle ply laminates over a period of eight years. The effect of curing stresses on laminate warpage and fracture was studied experimentally and analytically using lamination theory.

Pagano and Hahn [18] used the procedure described in [11] to calculate residual thermal stresses, and studied their effect on failure in laminates. The curing stresses were found to influence first failure in laminates greatly, often reducing the applied load to failure by about half. They note that the interlaminar normal stress σ_z is significant in some stacking sequences, especially at free edges, and that this would result in failure initiating at loads much less than their calculated values. Their analysis is based on lamination theory and thus

does not treat the free edge problem in any detail.

Farley and Herakovich [19], using a finite element analysis, compared boundary layer stress distributions due to mechanical, thermal, and moisture loads in finite width laminates. Each type of load was analyzed separately; the study concentrated on the response of laminates to different moisture gradients in the boundary layer.

Kim and Hahn [20] published results of acoustic emissions of laminates subject to mechanical loads. Curing stresses were included in the lamination theory development for predicting stress at which first failure occurred.

3. THEORETICAL BACKGROUND

The problem under consideration is the stress analysis of symmetric laminates, including thermal and free edge effects. In this study the nonlinear analysis for both mechanical and thermal loading is performed using an incremental procedure. The loading is approximated by a finite number of load steps and each step is treated as a linear problem. The applied load, whether mechanical or thermal, is assumed to be steady and uniform across the laminate.

3.1 General Formulation

A typical balanced, symmetric laminate is shown in Fig. 1. The behavior of the laminate can be assumed to be independent of the x coordinate if b and H are small compared to L. As shown by Pipes and Pagano [21] the linear strain displacement relations can be integrated and manipulated to yield the following displacement field over the cross-section of the laminate.

$$u = -(C_1 z + C_2)y + (C_4 y + C_5 z + C_6)x + U(y,z)$$

$$v = (C_1 z + C_2)x - C_4 \frac{x^2}{2} + V(y,z) \qquad (3.1)$$

$$w = -C_1 xy + C_y x - C_5 \frac{x^2}{2} + C_8 + W(y,z)$$

The displacement field has the following symmetry: with respect to the x-y plane,

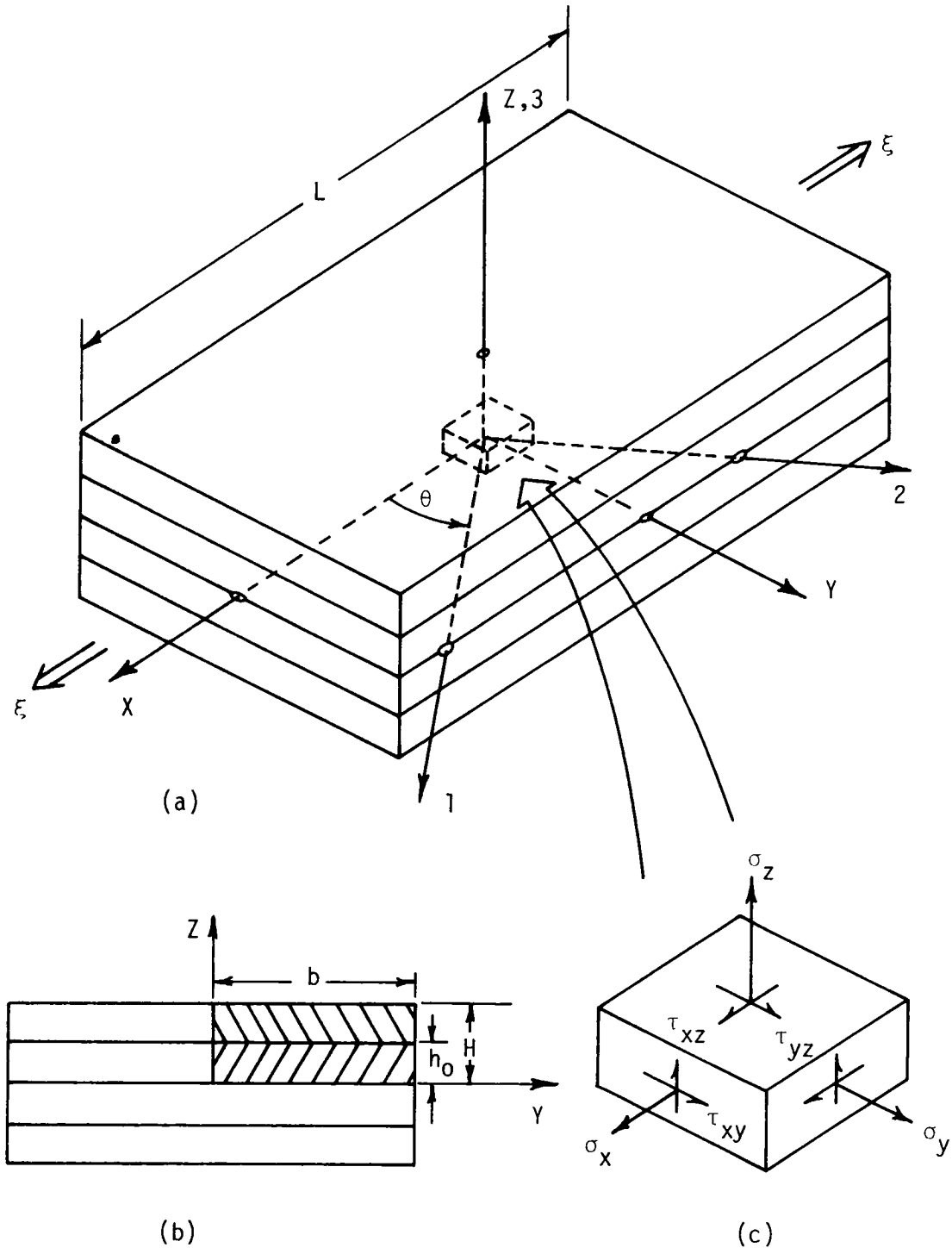

FIGURE 1. TYPICAL LAMINATE GEOMETRY

$$u(x,y,z) = u(x,y,-z)$$
$$v(x,y,z) = v(x,y,-z) \qquad (3.2a)$$
$$w(x,y,z) = -w(x,y,-z)$$

with respect to the x-z plane,

$$v(x,y,z) = -v(x,-y,z)$$
$$w(x,y,z) = w(x,-y,z) \qquad (3.2b)$$

It has been experimentally observed [22] that at $z=\pm H$

$$u(x,y,\pm H) = -u(x,-y,\pm H) \qquad (3.3)$$

As the thickness of the laminate is small, it can be assumed that

$$u(x,y,z) = -u(x,-y,z) \qquad (3.4)$$

These symmetries simplify the displacement field to

$$u = C_6 x + U(y,z)$$
$$v = V(y,z) \qquad (3.5)$$
$$w = W(y,z)$$

The analysis can now be restricted to one quarter of the cross-section (Fig. 2) with the following boundary displacement constraints:

$$V(0,z) = 0$$
$$W(y,0) = 0 \qquad (3.6)$$

The following stress boundary conditions complete the boundary value problem.

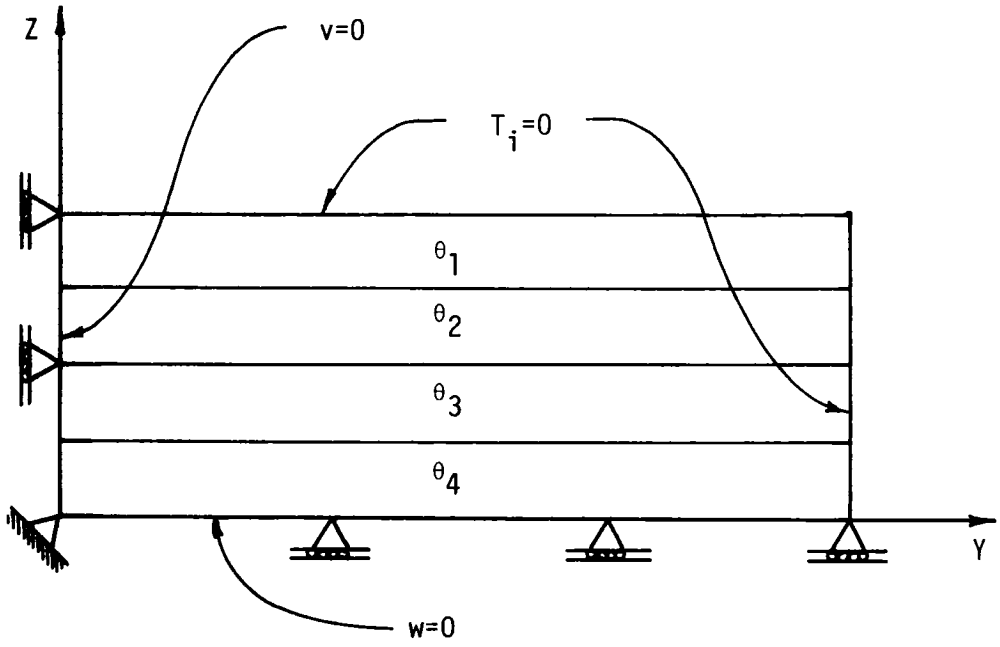

FIGURE 2. BOUNDARY CONDITIONS ON THE QUARTER SECTION OF THE LAMINATE

$$\tau_{zx}(x,y,\pm H) = \tau_{zy}(x,y,\pm H) = \sigma_z(x,y,\pm H) = 0$$
$$\tau_{xy}(x,\pm b,z) = \tau_{zy}(x,\pm b,z) = \sigma_y(x,\pm b,z) = 0 \qquad (3.7)$$

The individual laminae are orthotropic, having a stress strain relation with 9 independent constants. When referred to the laminate axis, the stress strain relation transforms to (Appendix A)

$$\begin{Bmatrix} \sigma_x \\ \sigma_y \\ \sigma_z \\ \tau_{yz} \\ \tau_{xz} \\ \tau_{xy} \end{Bmatrix} = \begin{bmatrix} \bar{C}_{11} & \bar{C}_{12} & \bar{C}_{13} & 0 & 0 & \bar{C}_{16} \\ \bar{C}_{12} & \bar{C}_{22} & \bar{C}_{23} & 0 & 0 & \bar{C}_{26} \\ \bar{C}_{13} & \bar{C}_{23} & \bar{C}_{33} & 0 & 0 & \bar{C}_{36} \\ 0 & 0 & 0 & \bar{C}_{44} & \bar{C}_{45} & 0 \\ 0 & 0 & 0 & \bar{C}_{45} & \bar{C}_{55} & 0 \\ \bar{C}_{16} & \bar{C}_{26} & \bar{C}_{36} & 0 & 0 & \bar{C}_{66} \end{bmatrix} \begin{Bmatrix} \varepsilon_x \\ \varepsilon_y \\ \varepsilon_z \\ \gamma_{yz} \\ \gamma_{xz} \\ \gamma_{xy} \end{Bmatrix} \qquad (3.8)$$

3.1.1 Finite Element Formulation

This boundary value problem is cast in the finite element framework. The cross section is subdivided into triangular elements, and the displacement field is assumed to vary linearly within each element. The elemental displacement field is represented in terms of the nodal coordinates and the nodal displacements. The total potential energy, consisting of the strain energy and the potential of external forces, is written for each element in terms of the nodal displacements and forces. The potential energy is then minimized with respect to the nodal displacements to obtain a linear set of equations relating nodal displacements to nodal forces through the element "stiffness matrix".

These elemental stiffness matrices are assembled to form a system of equations in the unknown nodal displacements. The system of equations is solved after imposition of boundary conditions. The strains and stresses in each element are calculated from the displacements of the element nodes, the strain displacement relations and the constitutive equations.

3.2 Mechanical Loading

Let the laminate in Fig. 1 be loaded with a uniform strain ξ in the x direction. The displacement field over an element at a cross section $x=x_1$ becomes

$$\begin{aligned} u &= a_1 + a_2 y + a_3 z + \xi x_1 \\ v &= a_4 + a_5 y + a_6 z \\ w &= a_7 + a_8 y + a_9 z \end{aligned} \tag{3.9}$$

When the parameters a_1-a_9 are functions of the nodal coordinates and displacements. As the laminate behavior is independent of the x coordinate, x_1 is arbitrary. Because the displacement field is assumed to vary linearly over each element and the strain displacement relations are linear, the strains over each element are constant. The elemental strains can be written in the form:

$$\begin{Bmatrix} \varepsilon_x \\ \varepsilon_y \\ \varepsilon_z \\ \gamma_{yz} \\ \gamma_{xz} \\ \gamma_{xy} \end{Bmatrix}^k = \frac{1}{A_k} \begin{Bmatrix} \xi A_k \\ av_1 + cv_2 + ev_3 \\ bw_1 + dw_2 + gw_3 \\ bv_1 + dv_2 + gv_3 + aw_1 + cw_2 + ew_3 \\ bu_1 + du_2 + gu_3 \\ au_1 + cu_2 + eu_3 \end{Bmatrix}^k \tag{3.10}$$

where A_k is the area of the element, u_i, v_i, w_i, $(i = 1,2,3)$ are the u,v, and w displacements of the nodes 1, 2 and 3, respectively, and a,b,c,d,e,g are known constants involving nodal coordinates.

The potential energy of the element is then expressed in terms of the nodal displacements and forces. Minimization with respect to the nodal displacements yields the following set of equations:

$$[K]^k \begin{Bmatrix} u_1 \\ v_1 \\ w_1 \\ u_2 \\ v_2 \\ w_2 \\ u_3 \\ v_3 \\ w_3 \end{Bmatrix}^k = \begin{Bmatrix} f_{1x} \\ f_{1y} \\ f_{1z} \\ f_{2x} \\ f_{2y} \\ f_{2z} \\ f_{3x} \\ f_{3y} \\ f_{3z} \end{Bmatrix}^k \tag{3.11}$$

where [K] is the 9x9 element stiffness given in Appendix B.

The stiffness matrices of all the elements are superposed to obtain the global stiffness matrix. Boundary conditions are imposed as follows (Fig. 2):

Displacement Boundary Conditions:

$$V=0 \text{ along } y=0 \text{ and } W=0 \text{ along } z=0$$

This is achieved by constraining all the nodes on the line y=0 against displacement in the y direction, and those on z=0 against displacement in the z direction. Due to the assumed linear variation of the displacement field, constraining two adjacent nodes also constrains the line joining them.

Traction Boundary Conditions:

$$T_1=0 \text{ on } z=H \text{ and } y=b$$

The traction boundary conditions are imposed by applying statically equivalent nodal forces. The surfaces at z=H and y=b are stress free and equivalent nodal forces are therefore zero.

The reader is refered to [1] for a more detailed discussion of the finite element formulation.

3.3 Thermal Loading

The basic assumption in the thermal formulation is that the total strain can be written as a sum of a stress related mechanical strain and a free thermal strain.

The displacement field over the element has the same form as (3.5) but the uniform strain ξ, instead of being known, is treated as an

additional unknown that is common to all the elements. It is equivalent to the total laminate strain during the thermal loading.

The mechanical strain $\{\varepsilon\}^{\sigma}$ is used to calculate the strain energy of the element.

$$\{\varepsilon\}^{\sigma} = \{\varepsilon\}^{\circ} - \{\varepsilon\}^{T} \tag{3.12}$$

where $\{\varepsilon\}^{\circ}$ is the total strain, and $\{\varepsilon\}^{T}$ the thermal strain. In terms of the displacement field and coefficients of expansion, the mechanical strain in the k^{th} layer is:

$$\begin{Bmatrix} \varepsilon_x \\ \varepsilon_y \\ \varepsilon_z \\ \gamma_{yz} \\ \gamma_{xz} \\ \gamma_{xy} \end{Bmatrix}^{k} = \begin{Bmatrix} \xi - (m^2\alpha_1 + n^2\alpha_2)\Delta T \\ (av_1 + cv_2 + ev_3)/A_k - (n^2\alpha_1 + m^2\alpha_2)\Delta T \\ (bw_1 + dw_2 + gw_3)/A_k - \alpha_3\Delta T \\ (bv_1 + dv_2 + gv_3 + aw_1 + cw_2 + ew_3)/A_k \\ (bu_1 + du_2 + gu_3)/A_k \\ (au_1 + cu_2 + eu_3)/A_k + 2mn(\alpha_1 - \alpha_2)\Delta T \end{Bmatrix}^{k} \tag{3.13}$$

Minimizing the potential energy of the element with respect to the nodal displacements and the unknown strain ξ, results in the following set of equations

$$[K]^k \begin{Bmatrix} u_1 \\ v_1 \\ w_1 \\ u_2 \\ v_2 \\ w_2 \\ u_3 \\ v_3 \\ w_3 \\ \xi \end{Bmatrix}^k = \begin{Bmatrix} f_{1x} \\ f_{1y} \\ f_{1z} \\ f_{2x} \\ f_{2y} \\ f_{2z} \\ f_{3x} \\ f_{3y} \\ f_{3z} \\ f_k \end{Bmatrix}^k \tag{3.14}$$

where [K] is the 10x10 element stiffness given in Appendix B.

The global stiffness matrix is obtained by the superposition of the element stiffness matrices. Boundary conditions are imposed as in the case of the mechanical load. There is one additional equation in the thermal problem for determining the uniform unknown strain ξ. It is equivalent to the force equilibrium equation for the thermal load

$$\sum_{k=1}^{n} f_k = F = 0 \tag{3.15}$$

The system of equations is solved for displacements and, as in the case of the mechanical loading, the strains and stresses calculated.

The thermal response is assumed to be linear elastic in this study. The stress state resulting from some temperature change from

T_i to T_f is given by

$$\{\sigma\} = \int_{T_i}^{T_f} [C(\tau)]\{\frac{d\varepsilon^{\sigma}}{d\tau}(\tau)\}d\tau \tag{3.16}$$

As exact mathematical forms for [C] and $\{\frac{d\varepsilon}{d\tau}\}^{\sigma}$ are not known, continuous integration cannot be performed, and for an incremental solution (3.16) must be evaluated as a summation.

$$\{\sigma\} = \sum_{i=1}^{nsteps} \{\Delta\sigma_i\} \tag{3.17}$$

Consider the ith load step in which the laminate is subject to a temperature change from T_1 to T_2. By the incremental strain theory, the increment of stress is given by

$$\{\Delta\sigma_i\}\Big|_T = [C(T)]\{\Delta\varepsilon^{\sigma}(T)\} \tag{3.18}$$

However, as pointed out by Hahn and Pagano [11] this equation does not take into account the temperature dependence of elastic properties. Their total strain theory gives the expression for the incremental stress to be

$$\{\Delta\sigma_i\}\Big|_T = [C(T)\{\Delta\varepsilon^{\sigma}(T)\} + (\frac{d}{dT}[C(T)])\varepsilon^{\sigma}(T)\Delta T \tag{3.19}$$

The second term of (3.19) is difficult to evaluate accurately in view of the limited data available for C(T). Further, for properties which do not exhibit large temperature dependence, the second term will be small for small ΔT. Thus the incremental stresses were approximated as

$$\{\Delta\sigma_i\}\Big|_{T_2} \simeq [C(T_m)]\{\Delta\varepsilon^{\sigma}(T_m)\} \tag{3.20}$$

where T_m is some intermediate temperature between T_1 and T_2, chosen to be the mean in this study. The temperature dependence of properties is included in the formulation through the term C(T).

3.4 Nonlinear Analysis

3.4.1 Mechanical Loading

The nonlinear analysis is carried out in an incremental fashion using data obtained in the previous load step to calculate the material constants for the current load step.

Ramberg Osgood parameters [23] are used to represent the nonlinear stress strain relations. Typically

$$\varepsilon = \frac{\sigma}{E} + k_i\sigma^{n_i} \qquad i=1,2 \tag{3.21}$$

The tangent modulus is defined as

$$\bar{E} = \frac{d\sigma}{d\varepsilon} = \frac{E}{k_i E n_i \sigma_i^{n_{i-1}+1}} \tag{3.22}$$

The stress at load step i is

$$\sigma_i = \sum_{j=1}^{i} \Delta\varepsilon^j \bar{E}_j \tag{3.23}$$

and the tangent modulus for the i+1 step is

$$\bar{E}_{i+1} = \frac{E}{k_i E n_i \left(\sum_{j=1}^{i} \Delta\varepsilon^j \bar{E}_j\right)^{n_{i-1}+1}} \tag{3.24}$$

The tangent modulus for each elastic constant is calculated assuming that there is no interaction between the various stresses during nonlinear behavior.

As indicated in Fig. 3 there is some error in following the stress-strain curve. This error can be minimized by iterating the solution in every load step, or by using smaller load steps, as is done in this study.

3.4.2 Thermal Loading

Temperature dependent elastic properties are used for the analysis of thermal loading. The elastic moduli E_{11}, E_{22}, G_{12}, etc., Poisson's ratios ν_{12}, ν_{23}, etc., and strengths X, Z, S_{13}, etc., are input at various temperatures, in the form of percent retentions, as shown in Fig. 4. In a given thermal load step, the mean temperature T_m is found and the property linearly interpolated between the nearest higher and lower temperatures (T_1,T_2) for which properties have been input. These interpolated values are then used to evaluate the stiffness matrices. The analysis accuracy improves with a larger number of input points, since the retention curves for elastic properties and strengths are approximated to greater accuracy.

3.5 Failure Criterion

The finite element analysis provides a three dimensional state of stress, presenting a unique opportunity to study stress interaction and failure.

Tsai and Wu [24] proposed that the failure surface be represented in the form of a tensor polynomial

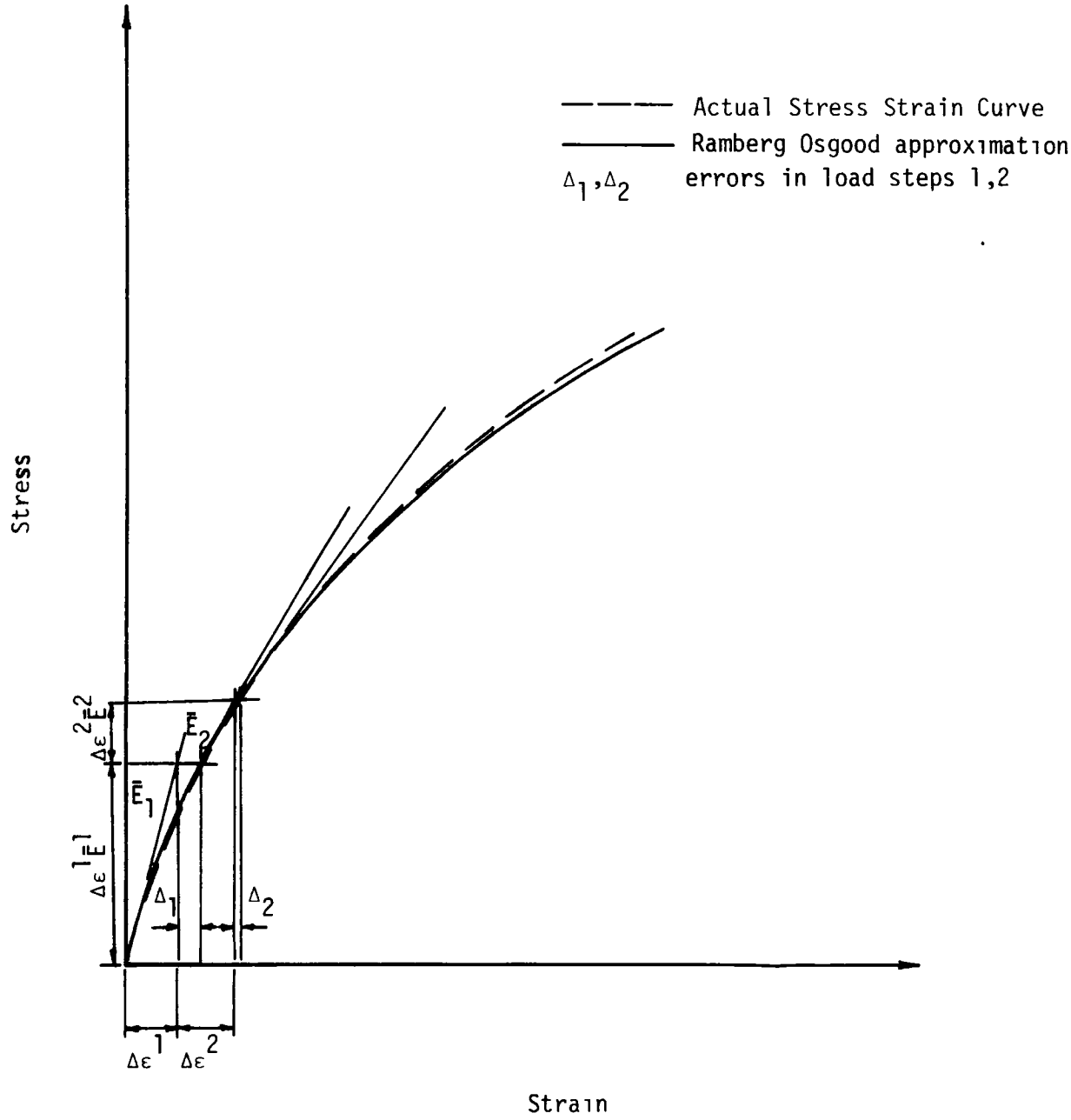

FIGURE 3. DETERMINATION OF TANGENT MODULI WITH RAMBERG-OSGOOD APPROXIMATIONS

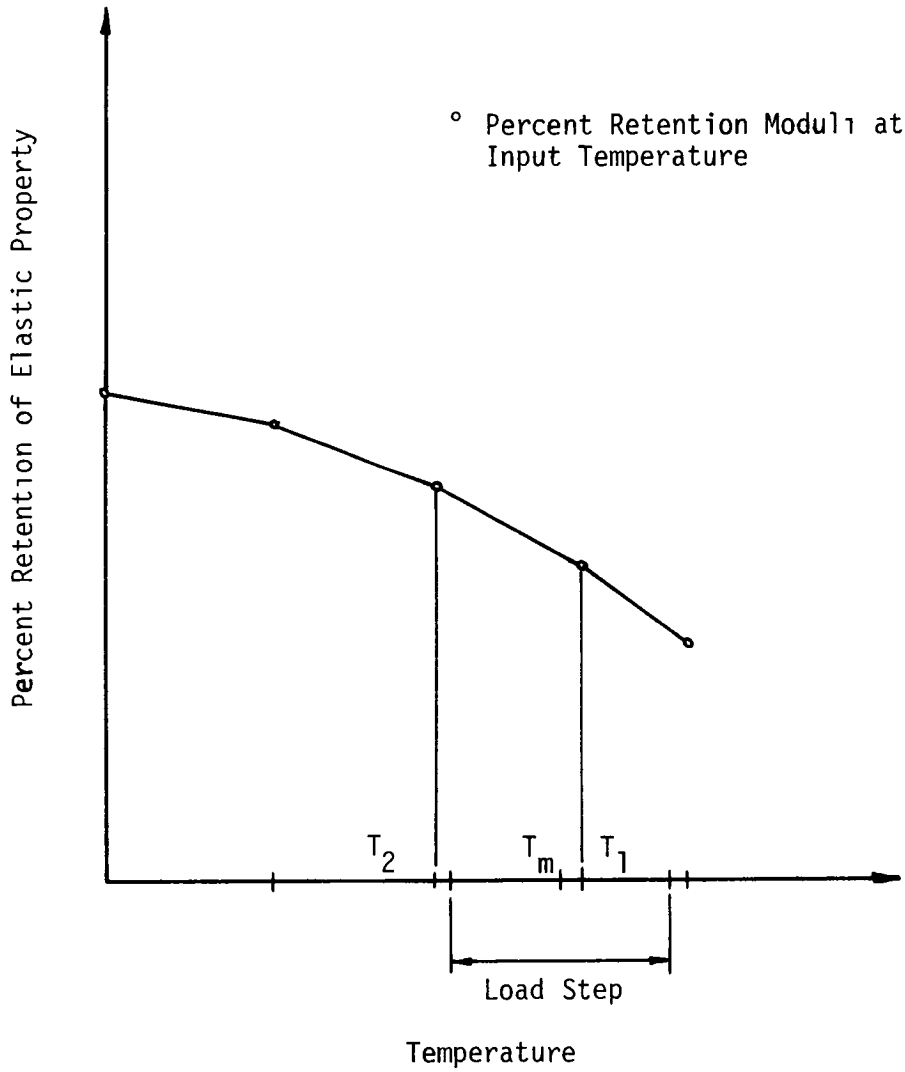

FIGURE 4. TYPICAL PERCENT RETENTION CURVE

$$F_{ij}\sigma_{ij} + F_{ijkl}\sigma_{ij}\sigma_{kl} = 1 \qquad (3.25)$$

The F_{ij} is a second order tensor and F_{ijkl} a fourth order tensor. The numerical values of the terms are obtained from the material principal strengths. The tensors simplify greatly for orthotropic material. The transformations of the nonzero terms in these tensors, in the contracted notation, are given in Appendix C. The strength parameters F_{12}, F_{23} and F_{13} require special biaxial loading tests unlike all other parameters which can be obtained from tensile, compressive and shear tests. Failure is predicted to occur when the value of the polynomial is equal to or greater than 1.0. The failure mode can be predicted by comparing the individual contributions of the stress components to the polynomial [25].

4. PRELIMINARY STUDIES

4.1 Mesh Size

The present analysis is conducted at the lamina level, (treating the fiber matrix system as a continuum) and not at the micromechanical level. The finite element method discretizes the domain being analyzed. Using finer grids, one can get a better representation of gradients and hence better results. The problem is deciding on the appropriate size of elements for the problem being studied.

Lamination theory results are accurate in the interior of the laminate. The elements in that region can be much larger than those near the free edge where large stress gradients exist and a finer mesh is necessary. The effect of mesh size was studied by using various meshes for a $[90/0]_s$ laminate that was loaded with the same strain of 0.1 percent, keeping all the material properties constant. It was observed that not only do the stresses in the region near the free edge change, but the maximum value of the tensor polynomial used to predict failure changes with mesh size. A linear elastic analysis also predicts different first failure location, for the same laminate and the same loading, depending on the mesh used. Table 1 shows the location and maximum value of the tensor polynomial for various meshes (Appendix E1, E2, E3, E4, E5) for a tensile load of 0.1 percent strain. The meshes were generated using the mesh generation code devloped by Bergner et al [26].

The stress distribution is also a function of mesh. For example,

TABLE 1

INFLUENCE OF MESH SIZE ON FIRST FAILURE IN A $[90/0]_s$ LAMINATE

Mesh	Elements	Failure Location on Free Edge	Tensor Polynomial
E1	124	center of top layer	.238776
E2	230	center of top layer	.238876
E3	326	near interface in top layer	.256435
E4	598	near interface in top layer	.266231
E5	878	near interface in top layer	.280495

Linear Elastic; Applied Strain Loading

σ_z for a $[90/0]_s$ laminate exhibits singular behavior, with a large tensile value, at the free edge [25,27]. However, if the grid used is not fine enough, it is compressive rather than large tensile (Fig. 5).

In Gr/E laminates, there are approximately 20-25 filaments through the thickness in each ply. Fig. 6 shows the smallest elements in the grid drawn on the photograph of a typical Gr/E ply. In the finest mesh used in this study, there are 16 elements through each ply for four ply laminates and 32 elements through the thickness for two ply laminates. Therefore, per element, there is just over one filament in the thickness direction. For a laminate aspect ratio of 25, the number of filaments calculated to be in the smallest element is approximately 3.75, assuming a fiber volume fraction of 0.5. This mesh (Fig. E5) was modified so that it could also be used for a four layered laminate (Fig. 7).

4.2 Averaging Finite Element Results

The finite element formulation used in this investigation yields constant values for stresses over each element. Two adjacent elements, in general, give different values for the stress at points on their common boundary. In order to eliminate the discontinuity of the stresses, most finite element analyses use an averaging technique.

The following averaging scheme is used in this study (Fig. 8). The interlaminar stresses σ_z, τ_{yz}, τ_{xz} must be continuous throughout the laminate. At a point A, these stresses are averaged over the elements 11, 12, 13, 14. The laminate stresses σ_x, σ_y, τ_{xy} may be discontinuous across laminate interfaces, but within each ply, they

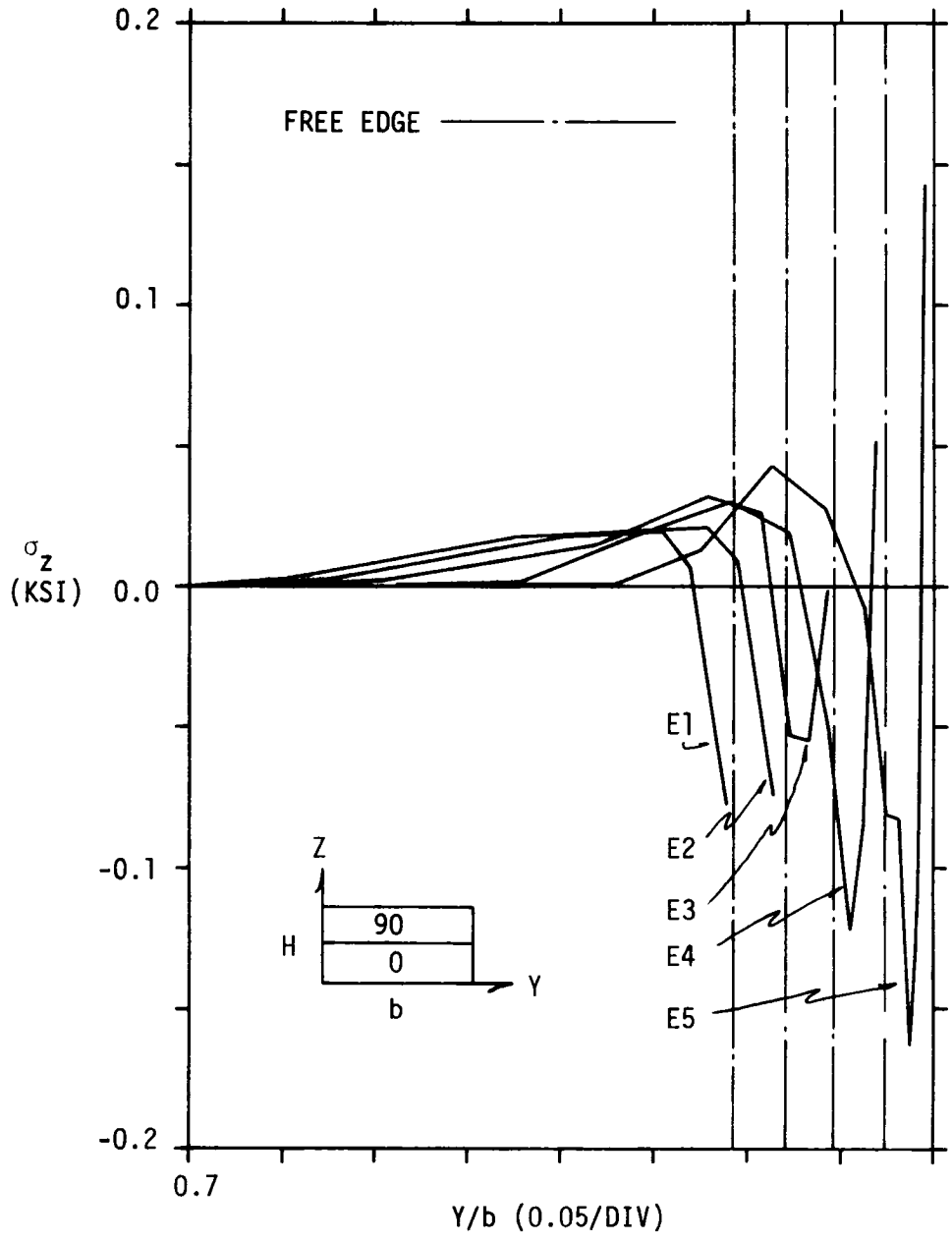

FIGURE 5. VARIATION OF σ_z AT THE INTERFACE OF A $[90/0]_s$ GR/E LAMINATE WITH MESH SIZE

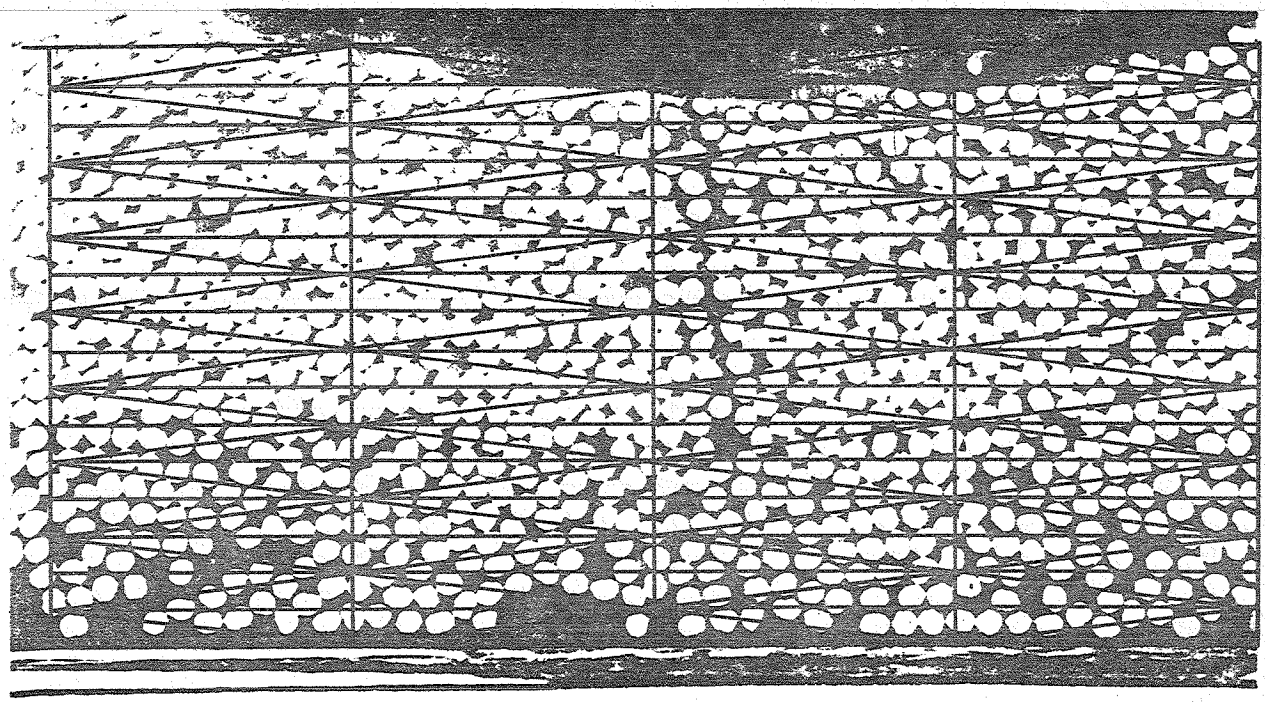

FIGURE 6. TYPICAL GRAPHITE/EPOXY PLY WITH SMALLEST ELEMENTS SUPERIMPOSED

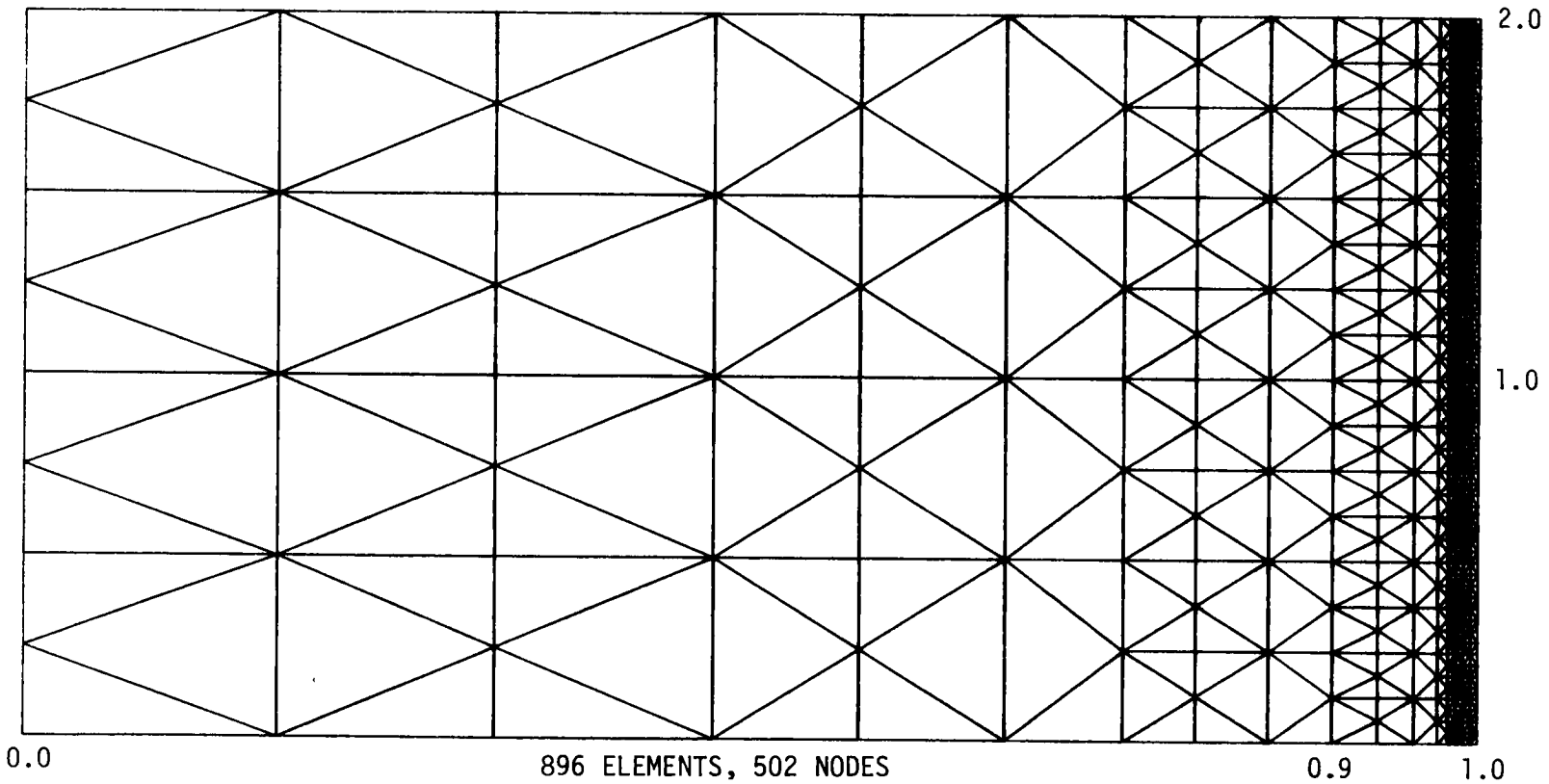

FIGURE 7. MESH E6

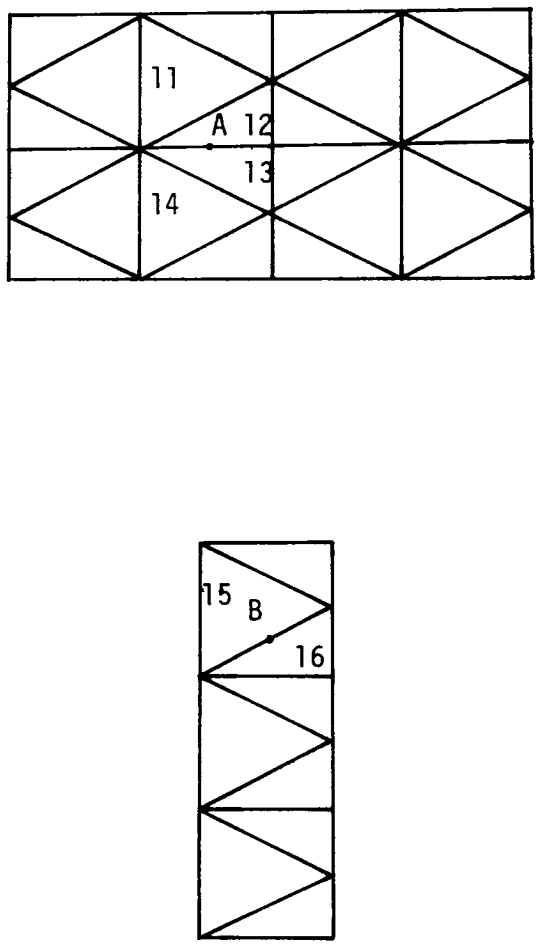

FIGURE 8. AVERAGING SCHEME

are continuous. At a point B they are averaged over elements 15 and 16.

4.3 Linear Elastic Analysis

The tensor polynomial predicts failure to occur when it attains the value 1.0. Suppose that for an applied strain ξ, the stress state is determined and the tensor polynomial calculated as

$$F_{ij}\sigma_{ij} + F_{ijkl}\sigma_{ij}\sigma_{kl} = \alpha + \beta = \gamma \tag{4.1}$$

Let failure occur at a strain of $k\xi$, i.e.

$$k\alpha + k^2\beta = 1 \tag{4.2}$$

This quadratic equation is solved for k, and the strain at first failure determined.

The stresses and tensor polynomial were evaluated for various laminates loaded with an axial strain of 0.1 percent. Based on these results, 'k' was calculated for the element which had the highest value of the tensor polynomial function for each laminate.

These values are presented in Table 2, and were used to estimate the mechanical load for first failure, and the number of load increments in the nonlinear analysis.

4.4 Stress Free Temperature

During manufacture, laminates are heated to some maximum elevated temperature; however, bonding usually takes place at some lower temperature. At that temperature, the laminate is in a stress free

TABLE 2

LINEAR ELASTIC PREDICTIONS OF FIRST FAILURE

Laminate	Strain at First Failure*
$[0/90]_s$	0.327956
$[90/0]_s$	0.375117
$[\pm 10]_s$	0.253761
$[\pm 15]_s$	0.22304
$[\pm 30]_s$	0.481329
$[\pm 45]_s$	0.476636
$[\pm 60]_s$	0.456682
$[\pm 75]_s$	0.423255
$[90/0/\pm 45]_s$	0.318849
$[\pm 45/0/90]_s$	0.149065

* Mesh E6

state. This stress free temperature T_o is the reference temperature for calculating the residual stresses. T_o depends on the material system of the laminate, and the cure cycle used. Tsai [6] suggested that T_o be experimentally determined from a $[\pm\theta]$ unsymmetrical laminate which warps on cooling. The temperature at which the laminate becomes flat on reheating is T_o. T300/5208 is cured at 350°F, but the suggested values for T_o vary widely. Renieri and Herakovich [1] used a value of 270°F, while Chamis always uses the highest temperature attained in the cure cycle as the value for T_o. A stress free temperature of 250°F is suggested in [18,20]. Hahn [14] reheated warped unsymmetrical laminates, but found values of T_o varying from 250 to 300 degrees. T_o was choosen to be 250°F for the present analysis.

4.5 Load Steps for Thermal Load

A study was conducted to evaluate the effect of cooling the laminate in different load steps. A $[90/0]_s$ laminate was chosen because it exhibits the maximum mismatch in expansion coefficients and material properties. This laminate was analyzed assuming the cooling from T_o to room temperature in 1, 2, 3, 4, 5, 6, 8, and 10 load steps, and the resulting distributions of σ_x plotted. Typical variation of the stress is presented in Fig. 9. The largest value of the tensor polynomial was also determined for these case studies. The results presented in Table 3 show that the maximum value decreased with increasing number of load steps. The location of the largest tensor

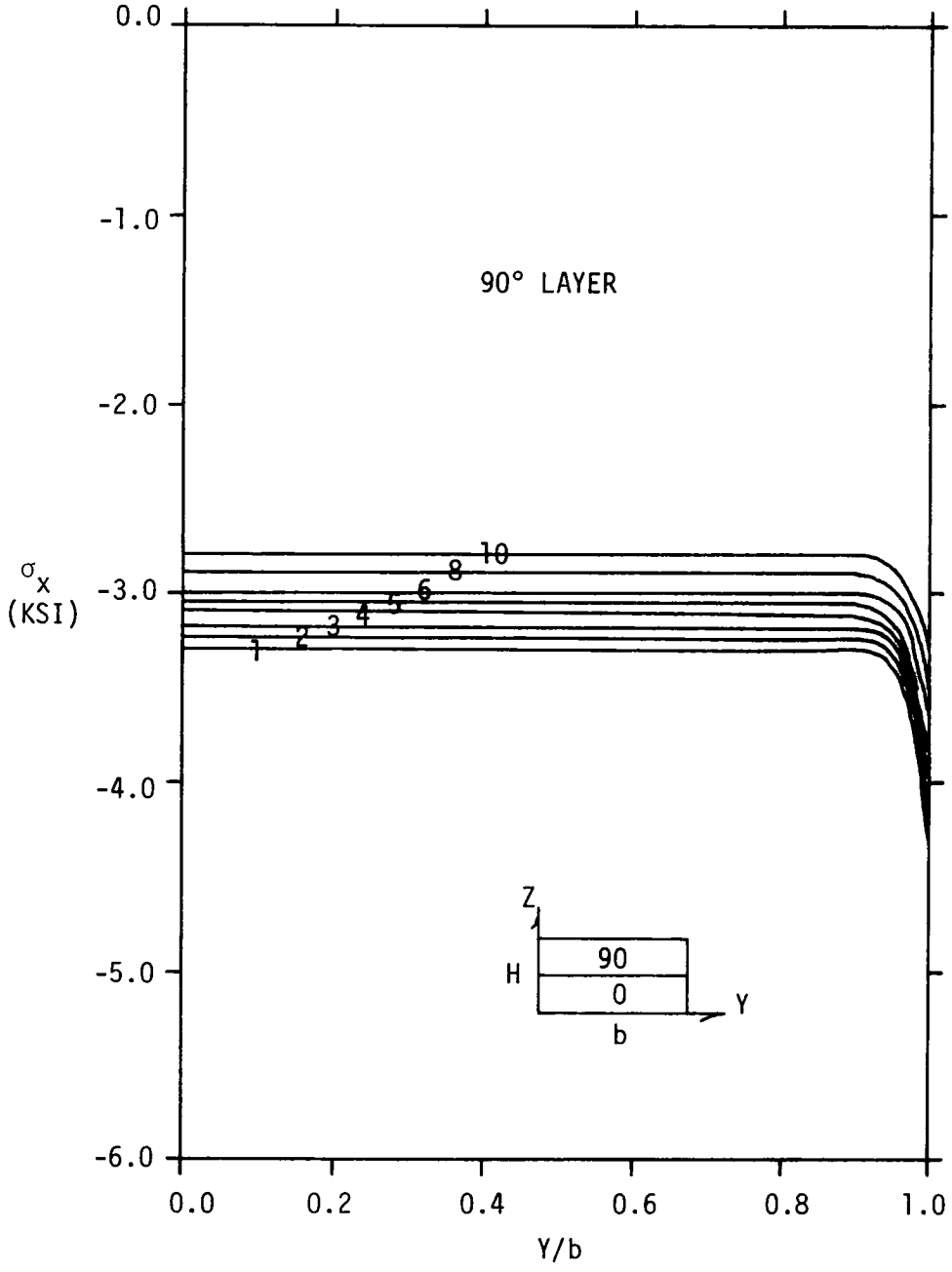

FIGURE 9. TYPICAL σ_x CURING STRESS DISTRIBUTIONS AS A FUNCTION OF THE NUMBER OF THERMAL LOAD STEPS

TABLE 3

EFFECT OF LOAD STEPS ON THE TENSOR POLYNOMIAL

$[90/0]_s$ LAMINATE

No. of Load Steps	Maximum Value of Tensor Polynomial
1	.8767522
2	.7699715
3	.7252781
4	.6949252
5	.6705358
6	.6497218
8	.6132286
10	.5822445

polynomial value was independent of the number of load steps. As seen from Fig. 9, the stress distribution appears to converge with increasing number of load steps. In this finite element analysis, the stiffness matrix must be recalculated for each load step. Using a grid with 896 elements therefore involves an enormous amount of expensive computation. It was decided to cool the laminate in 6 load steps of -30°F each, a compromise between satisfactory convergence and computer cost.

5. STRESS AND FAILURE ANALYSIS OF LAMINATES

Cross-ply, angle-ply, and two quasi-isotropic graphite/epoxy laminates were analyzed in this study. In order to obtain the total stress state in the laminate, the process of cooling to room temperature was modelled in thermal load steps with temperature dependent properties and the nonlinear analysis of subsequent mechanical loading was modelled as a number of linear elastic load steps. Stress distributions were plotted at the strain at which the first element was predicted to fail using the tensor polynomial failure criterion. Damage is predicted to initiate at this strain. This study does not predict the ultimate failure strain, but does predict the mode of first failure. Each load step for the mechanical load was taken to be 0.05 percent strain, the choice guided by the linear elastic predictions for the strain at first failure in each laminate and computer cost.

5.1 Cross-Ply Laminates

5.1.1 Stress Distributions

The mismatch of the expansion coefficients between adjacent layers is maximum in these laminates and results in very high curing stresses. For the purpose of comparison, distributions of non-zero laminate stresses are presented in Figures 10-13 for the following three cases:

1. residual thermal stresses.
2. nonlinear analysis of mechanical load at first failure (including residual stresses).

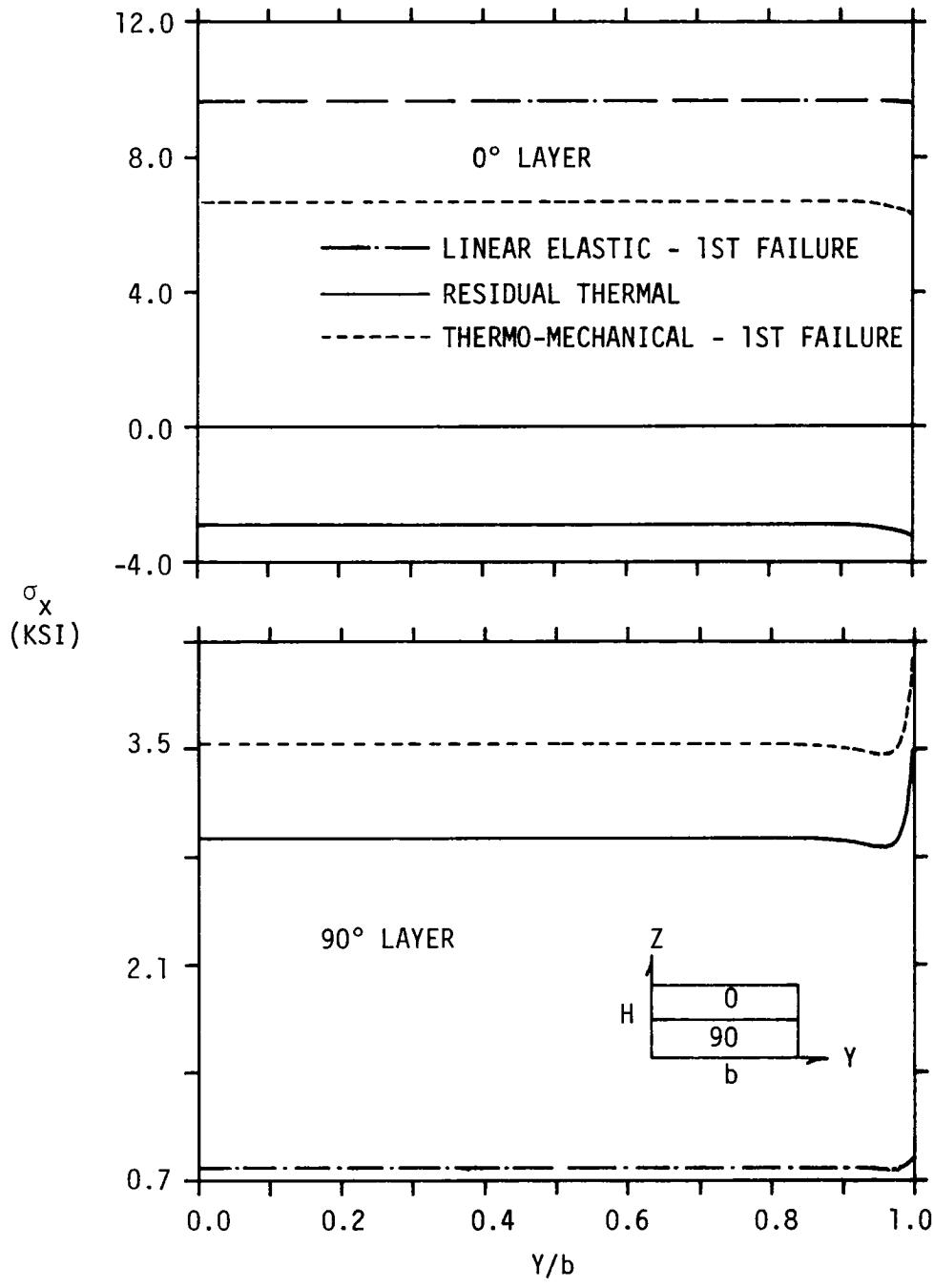

FIGURE 10. THERMO-MECHANICAL σ_x STRESSES IN A $[0/90]_s$ LAMINATE

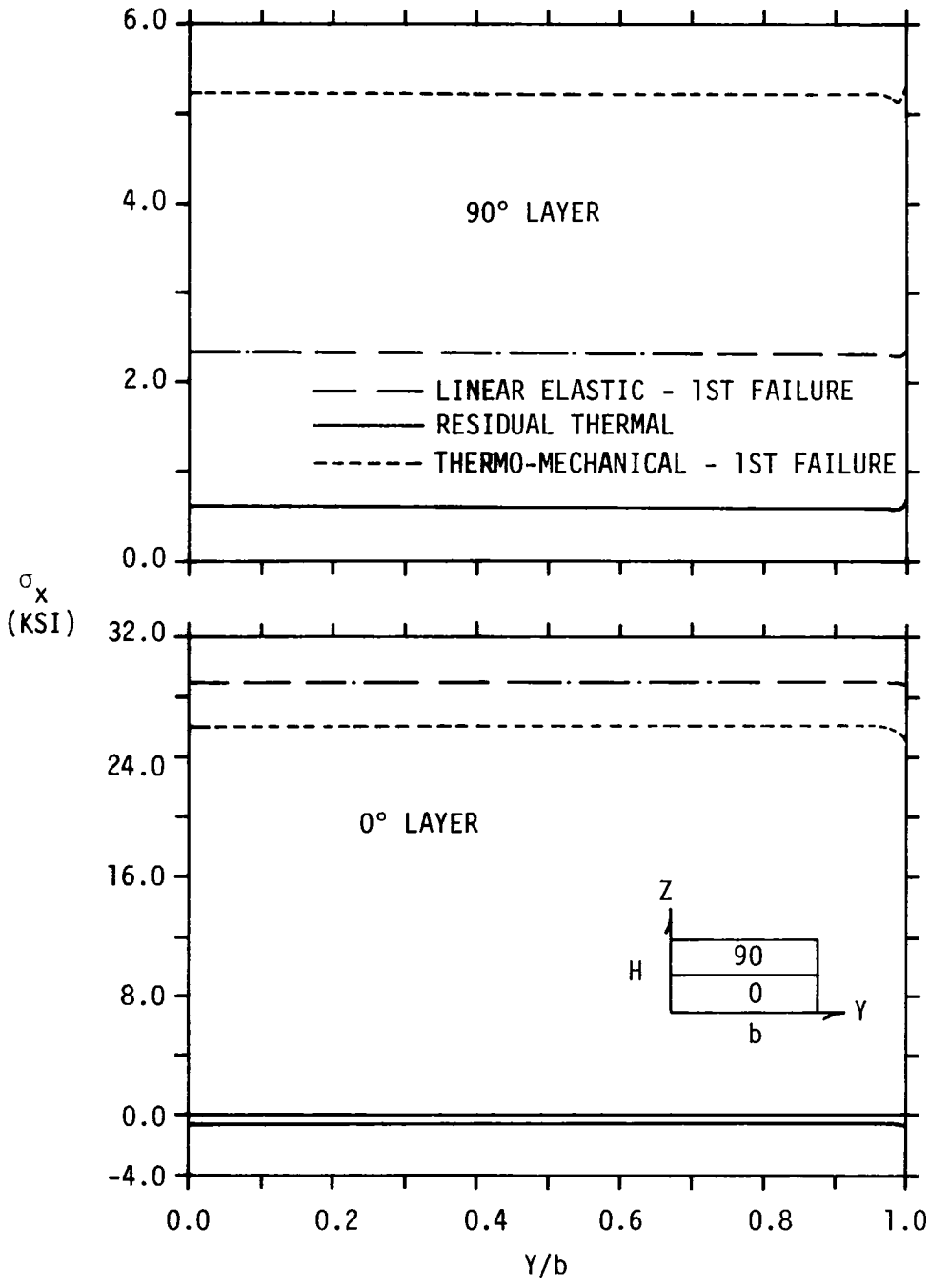

FIGURE 11. THERMO-MECHANICAL σ_x STRESSES IN A $[90/0]_s$ LAMINATE

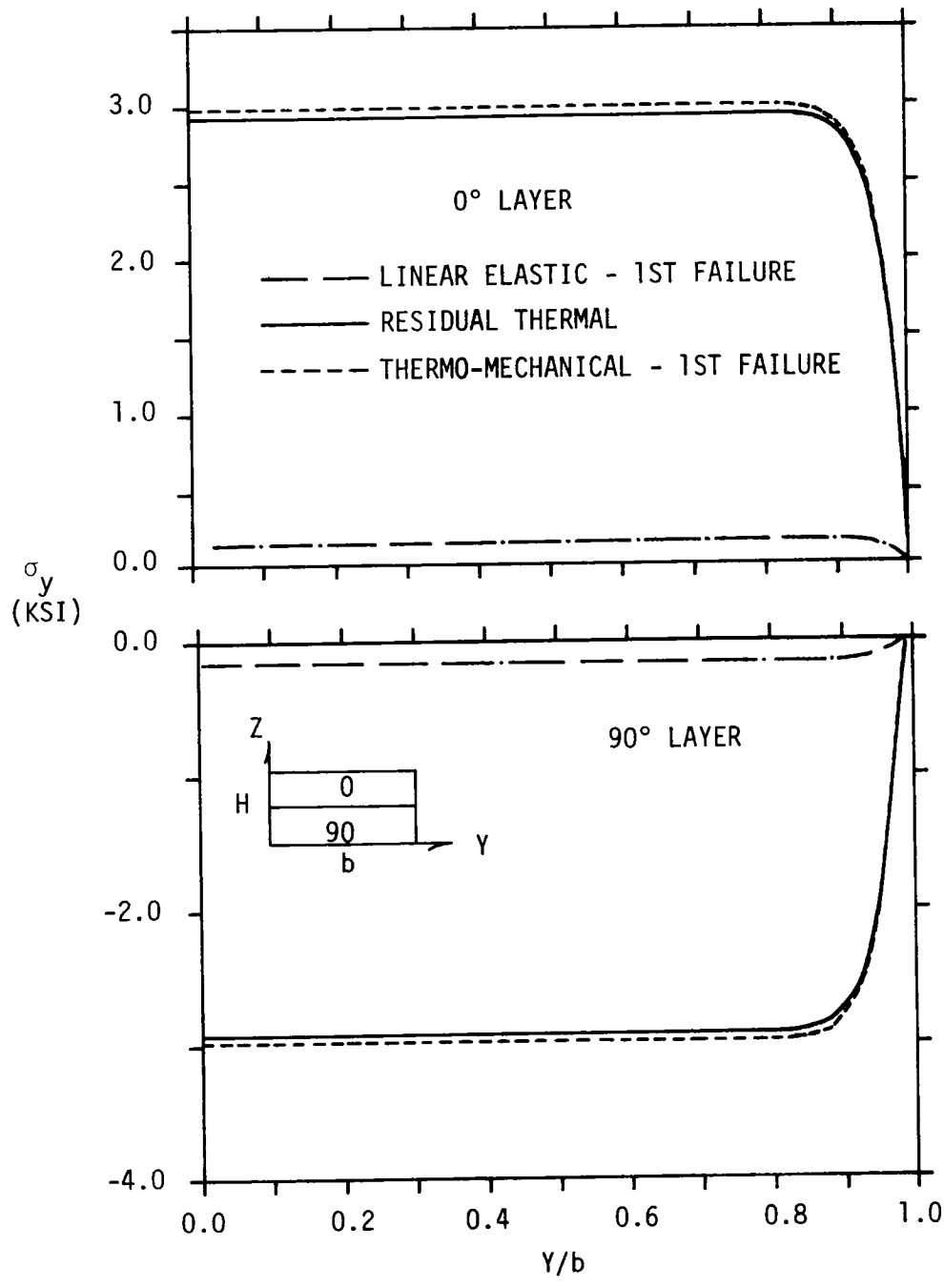

FIGURE 12. THERMO-MECHANICAL σ_y STRESSES IN A $[0/90]_s$ LAMINATE

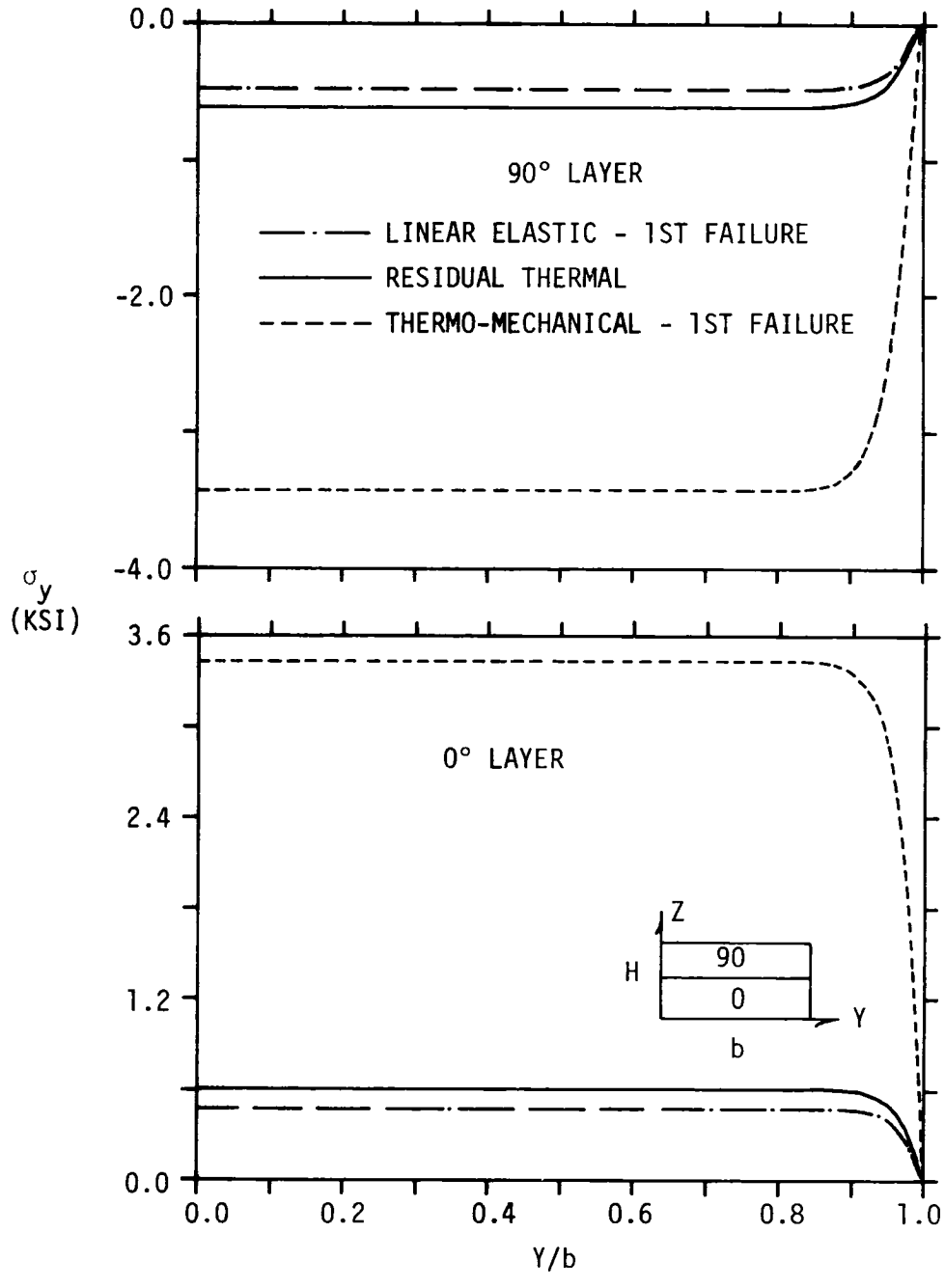

FIGURE 13. THERMO-MECHANICAL σ_y STRESSES IN A $[90/0]_s$ LAMINATE

3. stresses obtained from a linear elastic analysis of pure mechanical load, scaled to the first failure strain as predicted by the nonlinear analysis.

The laminate stresses σ_x and σ_y for the $[0/90]_s$ and $[90/0]_s$ laminates are shown in Figures 10-13. As a result of cooling, the laminate shrinks and σ_x is compressive in the 0° layers and tensile in the 90° layers, while σ_y is tensile in the 0° layers and compressive in the 90° layers. The stress magnitudes are equal for both layers and stacking sequences. The signs are opposite, thus satisfying equilibrium. With the application of an axial strain load, stress reversal occurs for σ_x in the 0° layers, but the 90° layers experience increased stress magnitude (Figs. 10, 11). Inclusion of thermal stresses is shown to have a significant influence on the overall state of stress at first failure. Comparison of the linear elastic and thermo-mechanical results for σ_x at first failure shows that the $[0/90]_s$ laminate is preferred with σ_x in the 0° layer being more than three times that in the $[0/90]_s$ laminate at first failure.

Edge effects are seen to be present for these laminate stresses. The axial stress (σ_x) is higher in the boundary layer of the 90° layers and lower in the 0° layers. The transverse stress (σ_y) decreases to zero at the free edge for both laminates and layers as required by the boundary conditions. Careful examination of the figure indicates that the boundary layer for thermal and thermo-mechanical loading is generally three to eight times that for the linear elastic analysis.

Interlaminar normal stress distributions are presented in

Figures 5 and 14 for the three loading cases. Moment and force equilibrium of the free body diagram in Figure 15 requires that

$$\Sigma M = 0 \Rightarrow \int_{z_1}^{z_1} \sigma_y z dz = \int_0^b \sigma_z y dy$$

$$\Sigma F_z = 0 \Rightarrow \int_{-b}^{b} \sigma_z dy = 0$$

Thus, the σ_z distribution along the 0/90 interface should be equivalent to a pure couple which balances the moment due to σ_y. Since the sign of σ_y changes when the stacking sequence is reversed, the direction of the σ_z couple should also be reversed. As indicated in Figure 14, this condition is satisfied in principle by the σ_z distributions for the two stacking sequences, for both thermal and thermo-mechanical loading. The results in Figure 5 for linear elastic loading of a $[90/0]_s$ laminate also indicate satisfaction of these equilibrium requirements.

As mentioned in section 4.1, the σ_z distribution near the free edge is very dependent on mesh size. The general character of the distribution is such that the equilibrium requirement are not grossly violated for any of the meshes studied in this investigation, however the magnitude σ_z at the free edge varied from -80 psi for the coarse mesh to +145 psi for the finest mesh for a linear elastic analysis and axial strain of 0.1 percent. These results confirm those of Wang and Dickson [27] that σ_z attains a tensile value at the free edge for

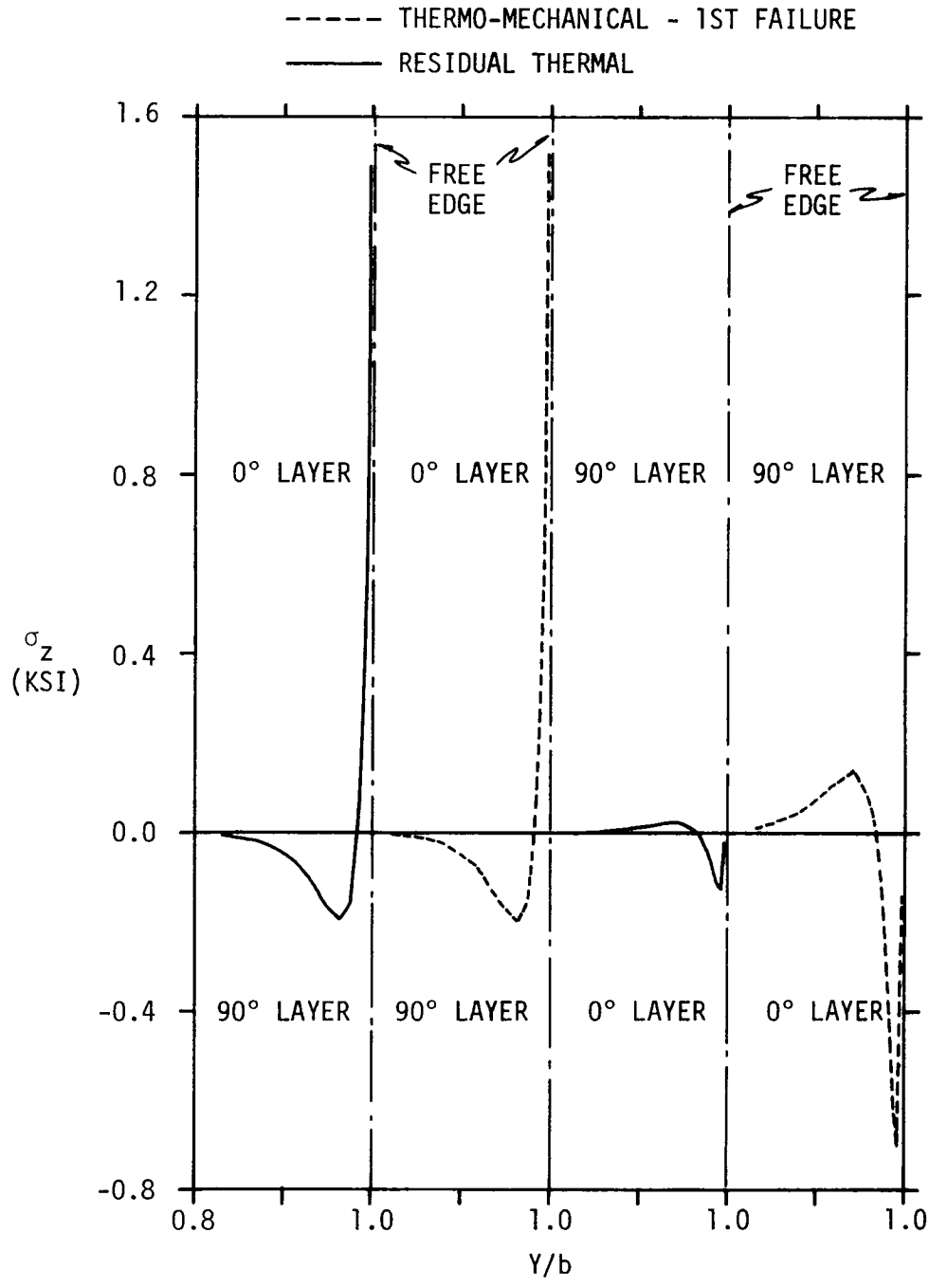

FIGURE 14. σ_z AT THE INTERFACE NEAR THE FREE EDGE IN $[0/90]_s$ AND $[90/0]_s$ LAMINATES

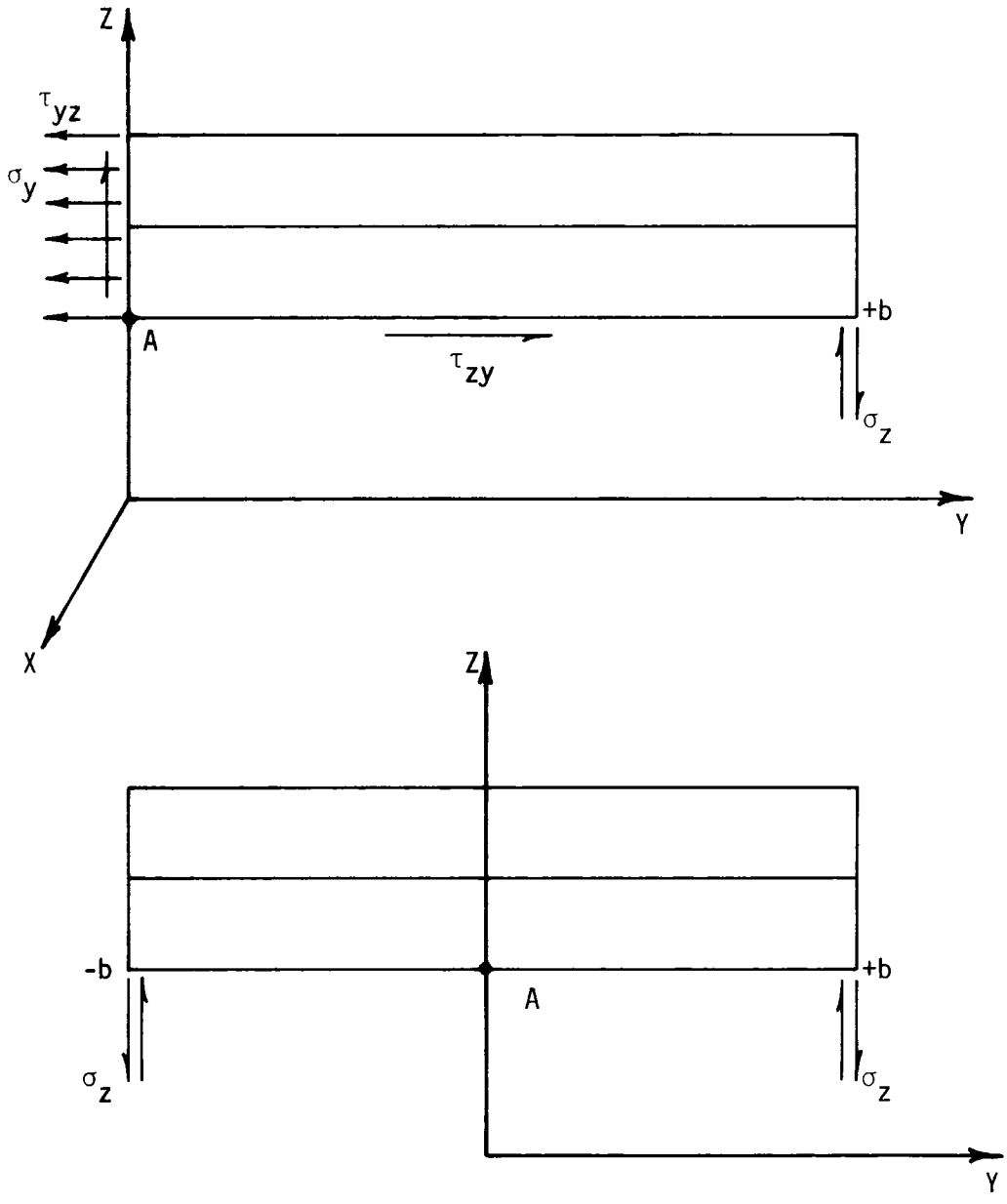

FIGURE 15. PARTIAL FREE BODY DIAGRAMS OF A LAMINATE

a $[90/0]_s$ as well as the $[0/90]_s$ laminate.

The results in Figure 14 were obtained with the finest finite element mesh from Figure 5 (i.e. E5). They show that σ_z in the $[0/90]_s$ laminate is tensile with singular behavior for both thermo and thermo-mechanical loading. It is also apparent that the thermal effects dominate the boundary layer stress distribution for the $[0/90]_s$ laminate. Reversing the stacking sequence does not result in a mirror image of the stress distributions. Figures 5 and 14 both indicate a second reversal of the gradient of σ_z near the free edge. The linear elastic results (Figure 5) predict a tensile σ_z near the free edge whereas the thermal and thermo-mechanical results show that thermal effects and nonlinear behavior have a beneficial effect on the magnitude of σ_z at the free edge of a $[90/0]_s$ laminate.

It is also apparent from Figure 14 that the significance of thermal effects is laminate dependent. Thermal effects dominate the σ_z distribution in $[0/90]_s$ laminates, but mechanical effects are more dominate in the $[90/0]_s$ laminate. Boundary layer width is, however, essentially the same for both types of loading and both laminates extending over approximately 15-20 percent of the laminate width. The width of the boundary layer in the $[90/0]_s$ laminate is essentially the same for all three types of loading (Figures 5 and 14).

Through-the-thickness variations of σ_z and σ_x for the residual stress state are compared to the distribution obtained by Wang and Crossman [16] using a linear elastic thermal analysis in Figures 16 and 17. Though the shape of the stress distributions is approximately

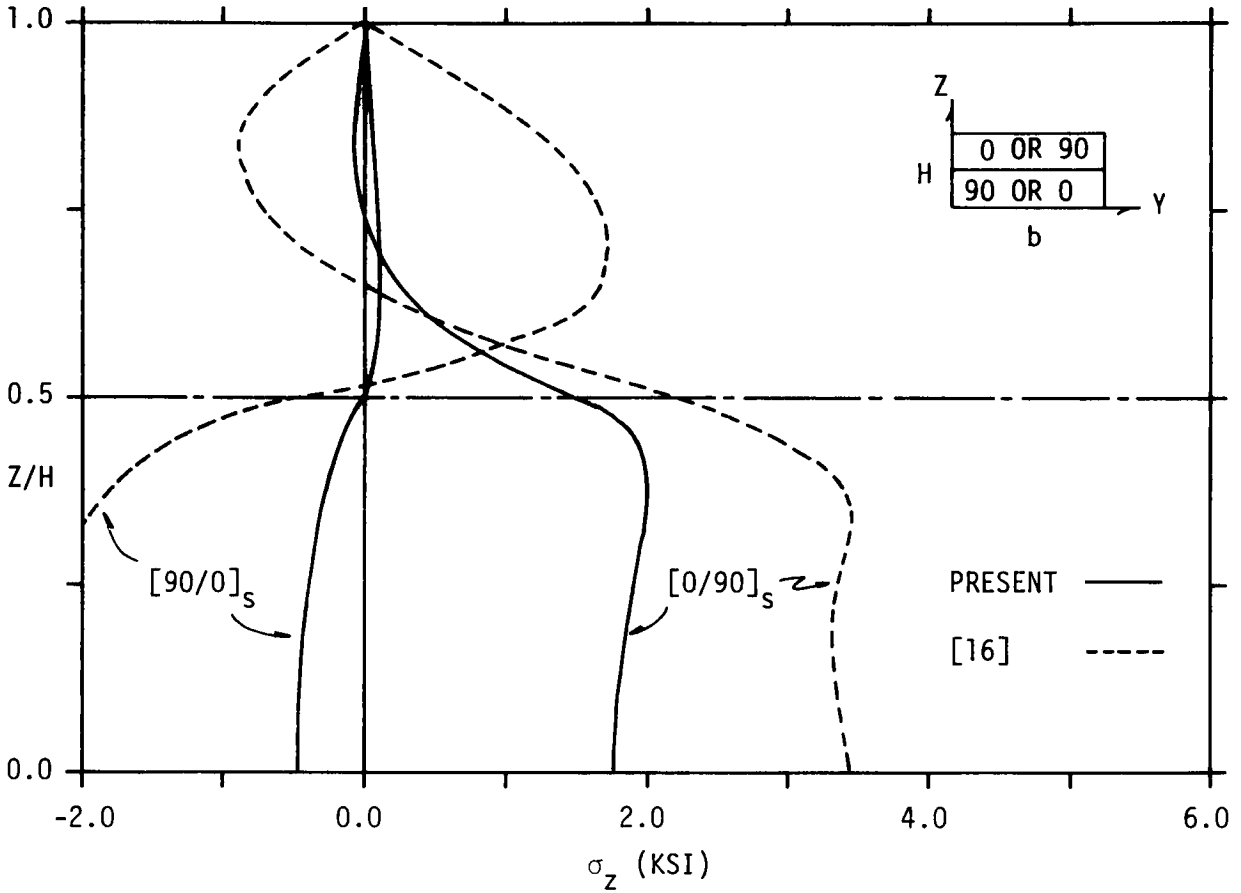

FIGURE 16. RESIDUAL σ_z THROUGH-THE-THICKNESS DISTRIBUTIONS NEAR THE FREE EDGE OF $[0/90]_s$ AND $[90/0]_s$ GR/E LAMINATES

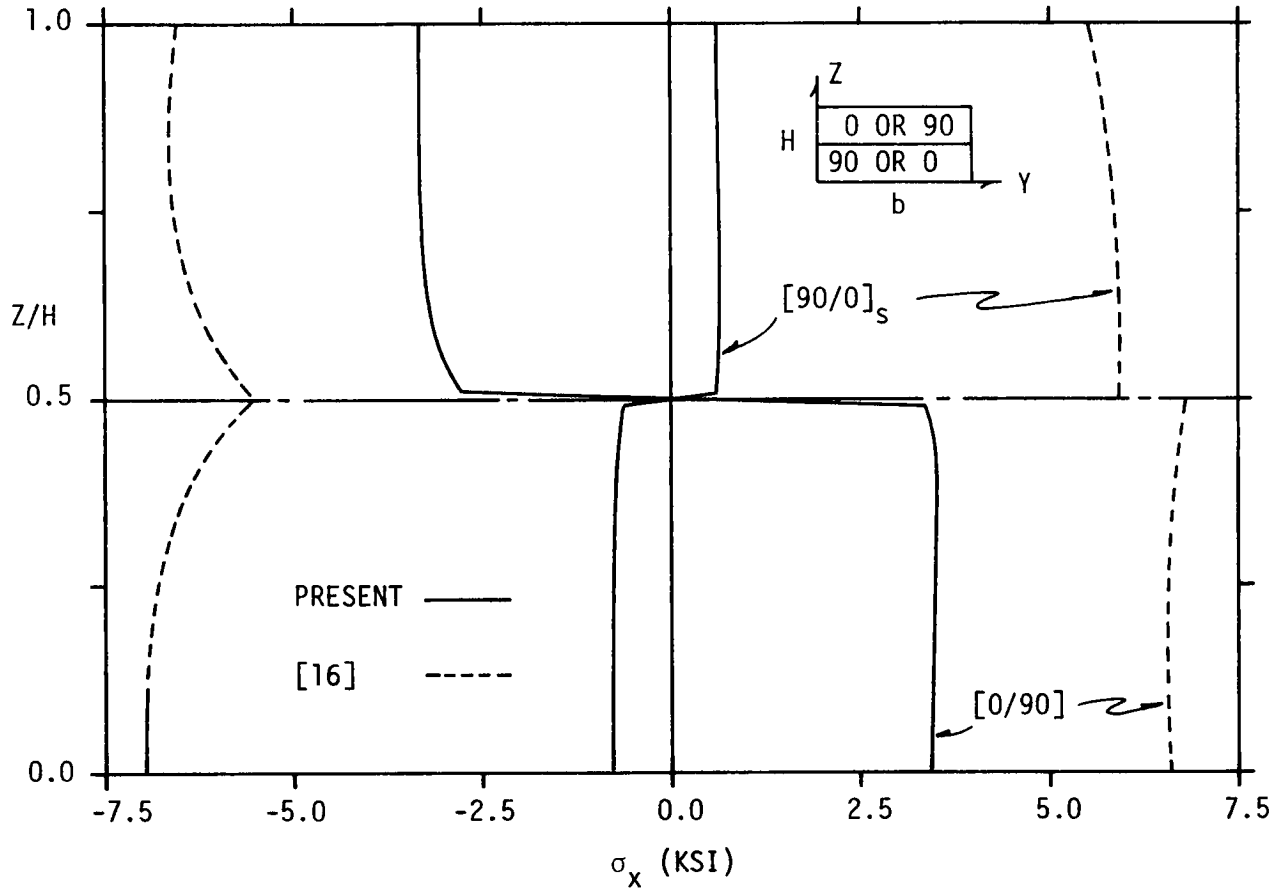

FIGURE 17. RESIDUAL σ_x THROUGH-THE-THICKNESS DISTRIBUTIONS NEAR THE FREE EDGE OF $[0/90]_s$ AND $[90/0]_s$ GR/E LAMINATES

the same, there is significant difference in the magnitude of the stresses. The maximum value of σ_z in a $[0/90]_s$, for example, is predicted to be 2.01 ksi by this analysis compared to a value of 5.4 ksi from [16]. This difference can be attributed to the incremental analysis using temperature dependent elastic properties. It should also be observed from Fig. 16 that, in all cases, the maximum positive value of σ_z occurs within a layer and not at the ply interface.

5.1.2 Failure Analysis

The curing stresses in cross-ply laminates are very high. In a $[0/90]_s$ laminate, the stresses resulting from cooling the laminate in six load steps were high enough for the tensor polynomial to predict failure. (In fact, cracks are sometimes observed at the free edge of cross-ply laminates [8,20].) For the purpose of this analysis, the $[0/90]_s$ laminate was cooled in eight load steps in order to reduce the step size and, thereby, eliminate the prediction of failure. All other laminates were cooled in six thermal increments. With the application of mechanical load, first failure was predicted to occur at a strain of 0.05 percent in the $[0/90]_s$ laminate and at 0.15 percent in the $[90/0]_s$ laminate.

The tensor polynomial is plotted along the interface and through the thickness for both laminates in Figures 18-20. Failure for both laminates was predicted to initiate in the 90° ply at the free edge. Figs. 18 and 19 show the variation of the tensor polynomial along the interface in the 90° ply, as determined from the curing stresses and subsequent mechanical loading. The curing stresses are predicted to

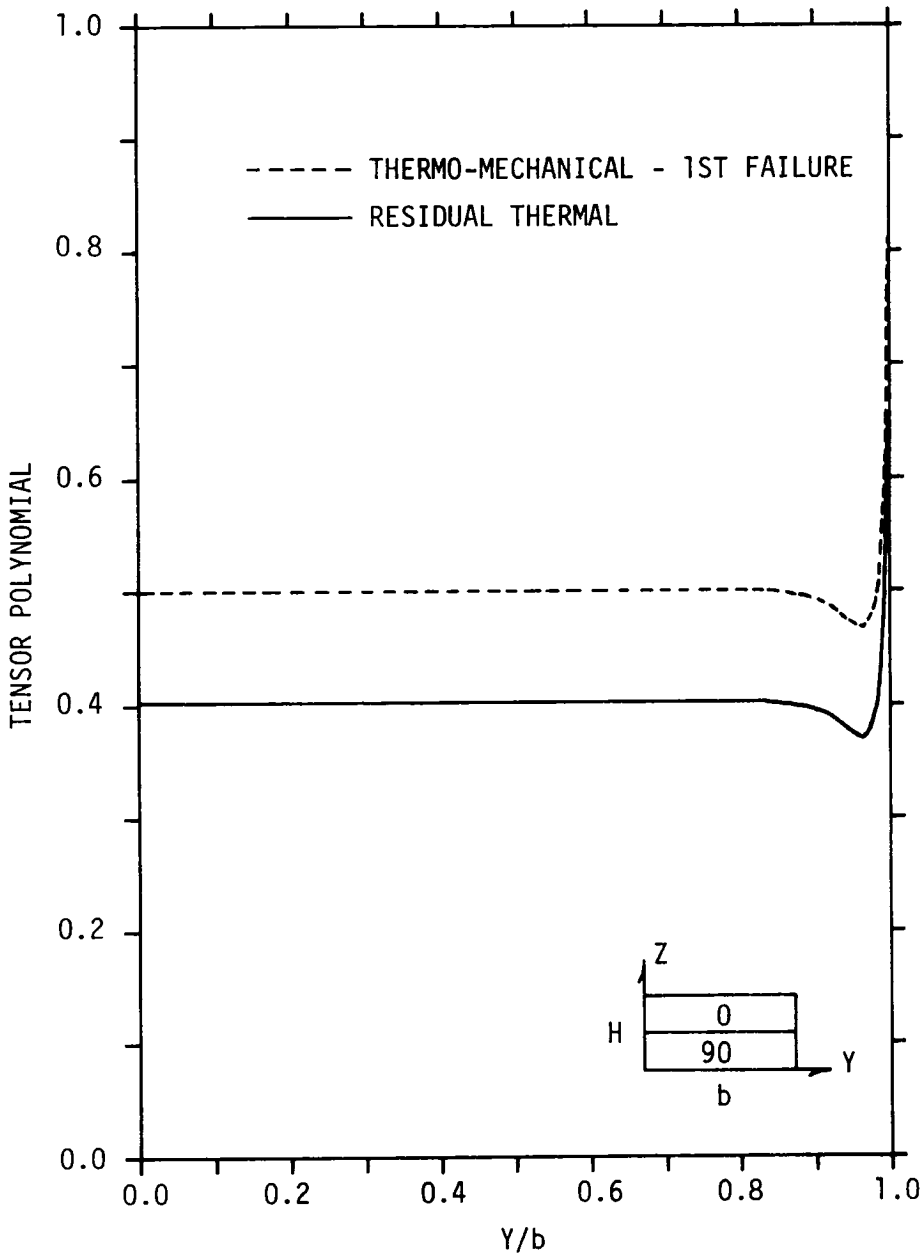

FIGURE 18. TENSOR POLYNOMIAL ALONG THE INTERFACE IN THE 90° LAYER FOR A $[0/90]_s$ LAMINATE

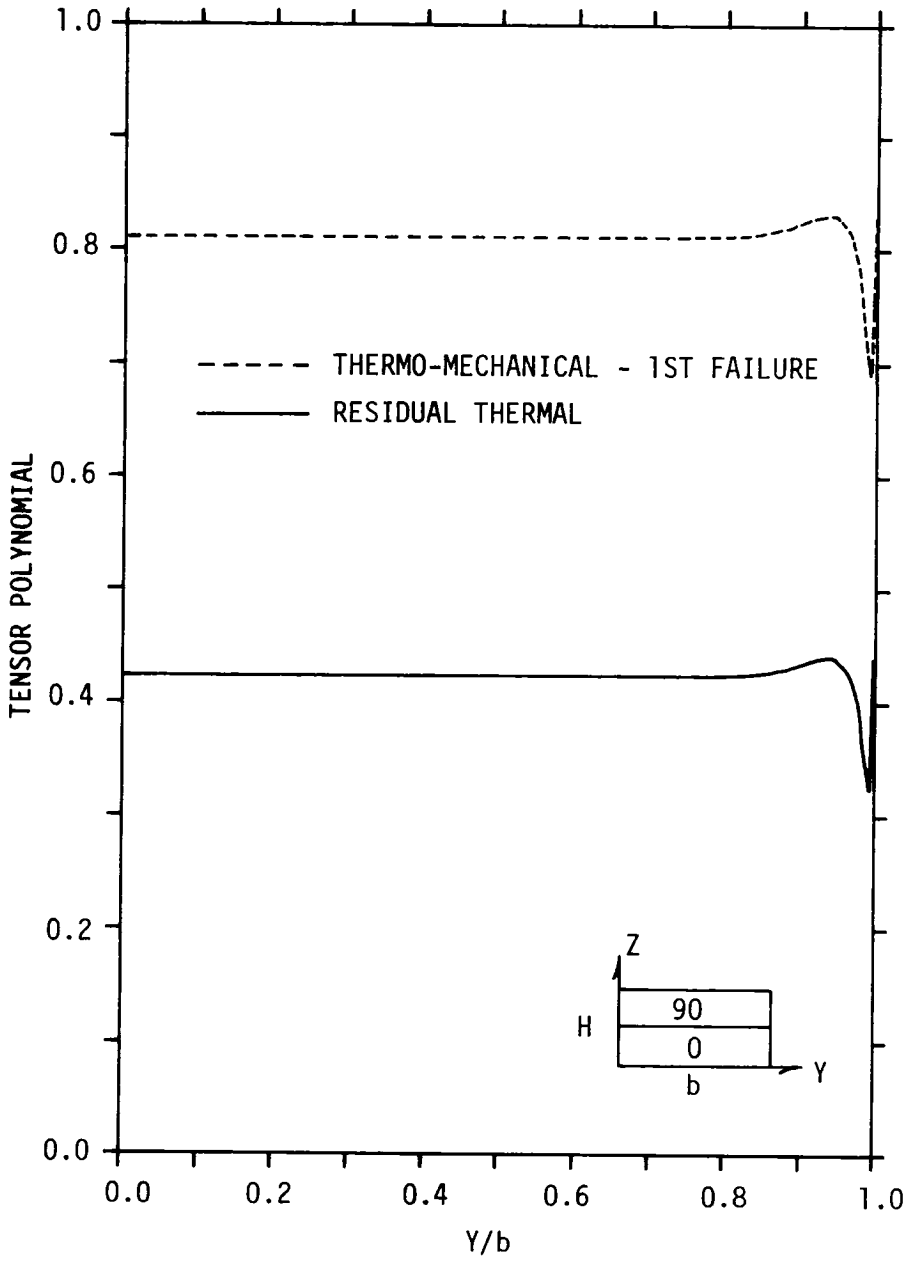

FIGURE 19. TENSOR POLYNOMIAL ALONG THE INTERFACE IN THE 90° LAYER FOR A $[90/0]_s$ LAMINATE

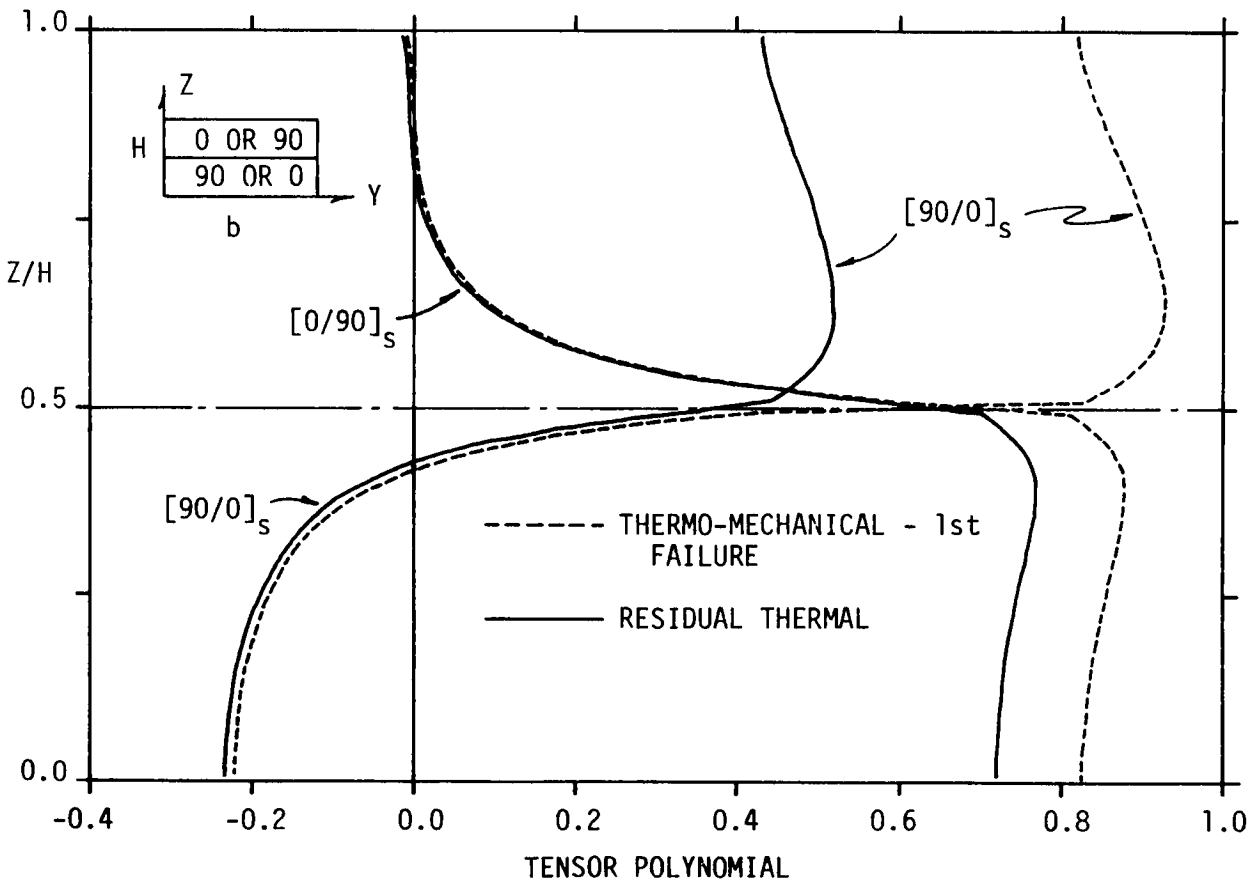

FIGURE 20. TENSOR POLYNOMIAL THROUGH-THE-THICKNESS AT THE EDGE OF $[0/90]_s$ AND $[90/0]_s$ LAMINATES

make a major contribution to initiation of failure in regions close to the free edge in both laminates. Through-the-thickness variation (Fig. 20) shows the effect of curing stresses to be significant in the 90° layers of both laminates. In the 0° layers the tensor polynomial has a negative value, which is possible when using the tensor polynomial failure criterion. The maximum value of the polynomial occurs within the 90° layer for both laminates, not at the 0/90 interface. Thus, first failure is predicted to occur within the layer and not at the interface.

The tensor polynomial for the element which was first to fail was analyzed in detail; the individual contributions from each of the contributing stresses are presented in Table 4. The table shows that while σ_z make the largest contribution to the polynomial at failure for both laminates, the contribution from σ_3 is very significant in the $[0/90]_s$ laminate. It may be said that the $[0/90]_s$ laminate fails in a mixed σ_2-σ_3 mode but the $[90/0]_s$ laminate fails primarily due to σ_2, i.e. transverse tension. The $[0/90]_s$ laminate experiences first failure at one-third the failure strain of the $[90/0]_s$. Since the $[90/0]_s$ is predicted to fail at a higher applied strain, it is prefered over the $[0/90]_s$ for tensile loading.

5.2 Angle-Ply Laminates

5.2.1 Stress Distributions

The angle-ply laminates studied were the $[\pm 10]_s$, $[\pm 15]_s$, $[\pm 30]_s$, $[\pm 45]_s$ $[\pm 60]_s$ and $[\pm 75]_s$. The thermal mismatch between adjacent plies

TABLE 4

FAILURE MODE ANALYSIS OF CROSS-PLY LAMINATES

Laminate	$F_2\sigma_2$	$F_{22}\sigma_2^2$	$F_3\sigma_3$	$F_{33}\sigma_3^2$	$F_2\sigma_2+F_{22}\sigma_2^2$	$F_3\sigma_3+F_{33}\sigma_3^2$	ε at First Failure
$[0/90]_s$	.4898	.1186	.3367	.6561	.6084	.3928	.0005
$[90/0]_s$	.6360	.2000	.1531	.0116	.8360	.1647	.0015

is not as severe as that in cross-ply laminates except for the $[\pm 45]_s$ laminate. Thus, the residual stresses are in general lower. It is interesting to note that, in the material principal coordinates, the residual stresses in the cross-ply and the $[\pm 45]_s$ laminate are the same, except at the free edges. This is of course expected because of the tensor property of the coefficient of thermal expansion.

The highest absolute value of each stress component was normalized and plotted versus the ply angle. Figs. 21 and 22 show the variation of the laminate and the interlaminar stresses for thermal and mechanical loading, respectively. The thermal mismatch in angle-ply laminates is maximum at 45°, and all thermal stresses (Fig. 21) attain their maximum values at 45°, except for σ_x which attains its maximum at 30°. This is because the stress state not only depends on the curing strain (thermal mismatch), but also on the elastic modulus and E_x decreases sharply as the ply angle increases from zero, tapering off at larger angles [29].

The maximum value of the individual stress components occur at different fiber angles for mechanical loading (Fig. 22). The magnitude of σ_x is large at low angles, with its maximum at 0°, while τ_{xz} attains its maximum at 15°. Three components, σ_z, τ_{yz}, σ_y, attain their maximum value at 30° and τ_{xy} attains its maximum at 45°. These results show that there are fundamental differences between thermal and mechanical loading of angle-ply laminates.

The distribution of curing stresses is roughly the same in all angle-ply laminates, the difference being in the magnitudes of

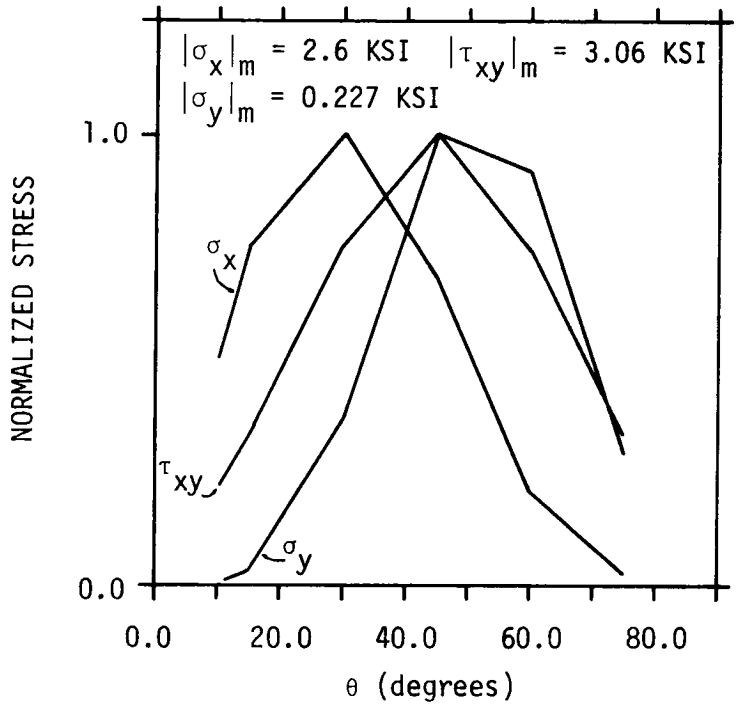

a) Intralaminar Stresses

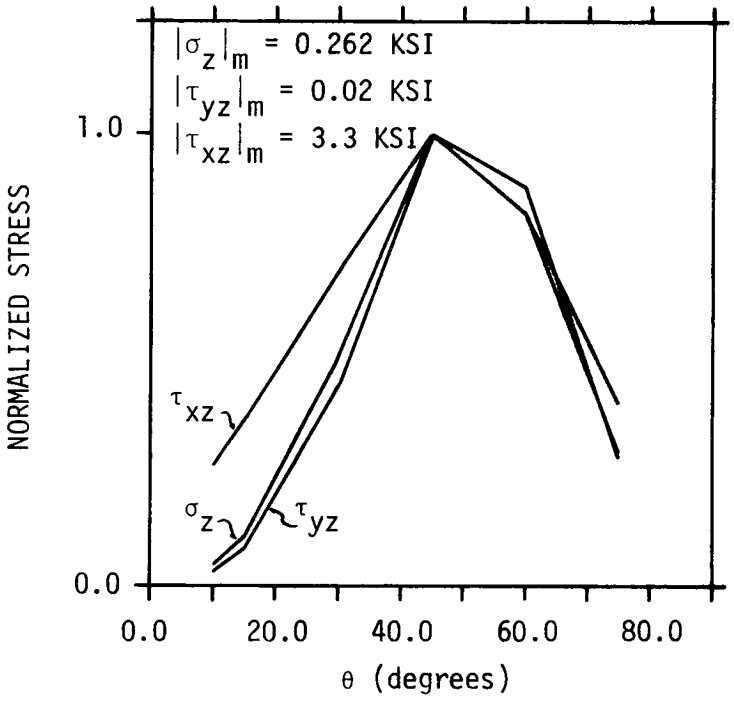

b) Interlaminar Stresses

FIGURE 21. NORMALIZED MAXIMUM CURING STRESSES IN $[\pm\theta]_s$ LAMINATES

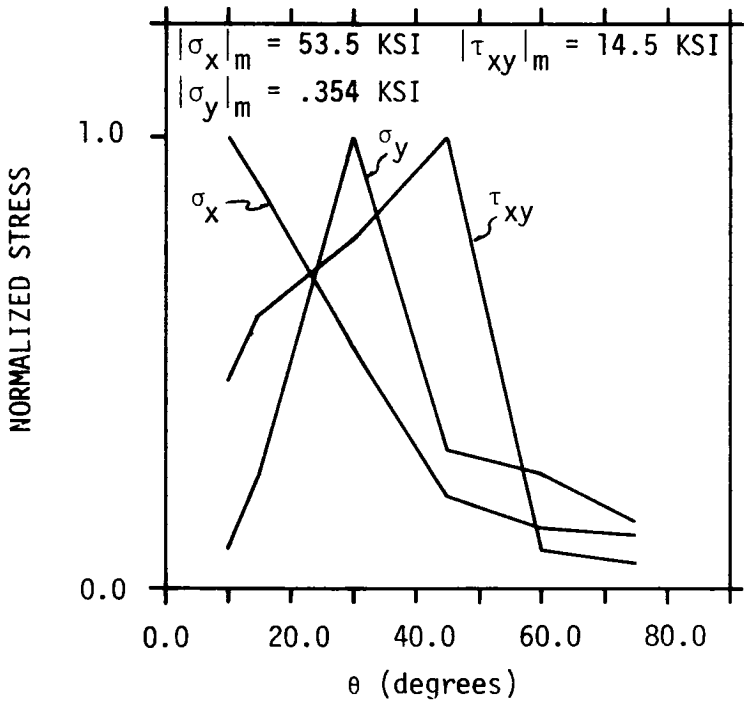

a) Intralaminar Stresses

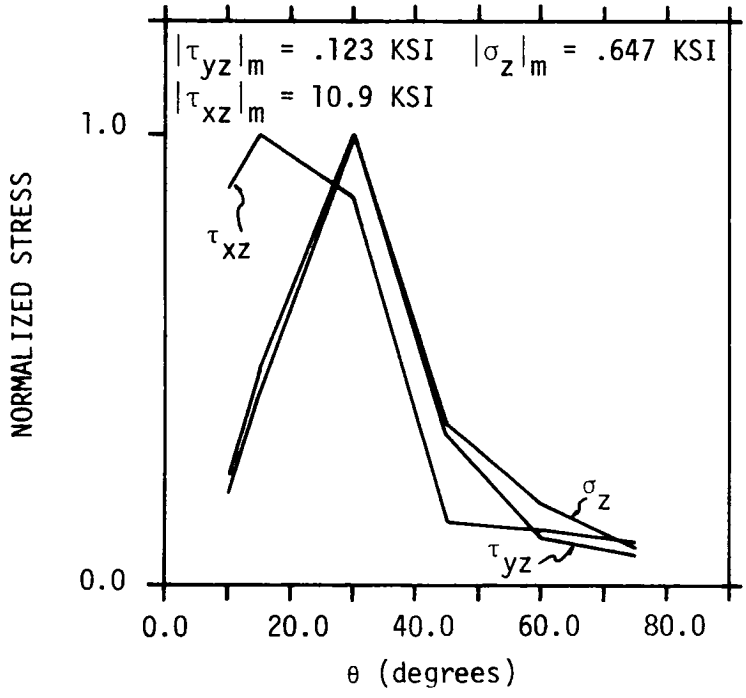

b) Interlaminar Stresses

FIGURE 22. NORMALIZED MAXIMUM STRESSES AT FIRST FAILURE IN $[\pm\theta]_s$ LAMINATES FOR THERMO-MECHANICAL LOADING

different ply orientations. The curing stresses in the $[\pm 45]_s$ are typical and are presented, Fig. 23 showing the lamina stresses and Fig. 24, the interlaminar stresses. The stresses σ_y, τ_{xy}, and τ_{yz} are seen to approach zero as required by the stress free boundary conditions. As in cross-ply laminates, the curing stresses exhibit edge effects, with the presence of a boundary layer for y/b greater than 0.9. Fig. 24 shows that the boundary layer for τ_{yz} at the ±45 interface is approximately twice that of σ_z at the midplane.

Though-the-thickness variation of σ_x and τ_{xz} near the free edge for a $[\pm 45]_s$ laminate are compared to distributions obtained by Wang and Crossman [15] in Fig. 25. As in the cross-ply laminates (Fig. 17) the present solution predicts much lower stresses. Both components of stress exhibit sharp gradients in the vicinity of the interface.

5.2.2 Failure Analysis

The interlaminar distribution of the tensor polynomial, at first failure, as determined for thermo-mechanical loading, is shown in Fig. 26 for various fiber angles. This figure demonstrates that the edge effects are dominant at small angles of orientation, and that edge stress concentrations decrease with increasing angle. At large angles, failure is first predicted at the free edge, but elements in the interior have large values for the tensor polynomial, hence the entire laminate is close to failure. The tensor polynomial exhibits a small negative value in the laminate interior for low fiber angles. This is acceptable in the failure criterion, and signifies that the region is well below failure. These results indicate that the laminate fails

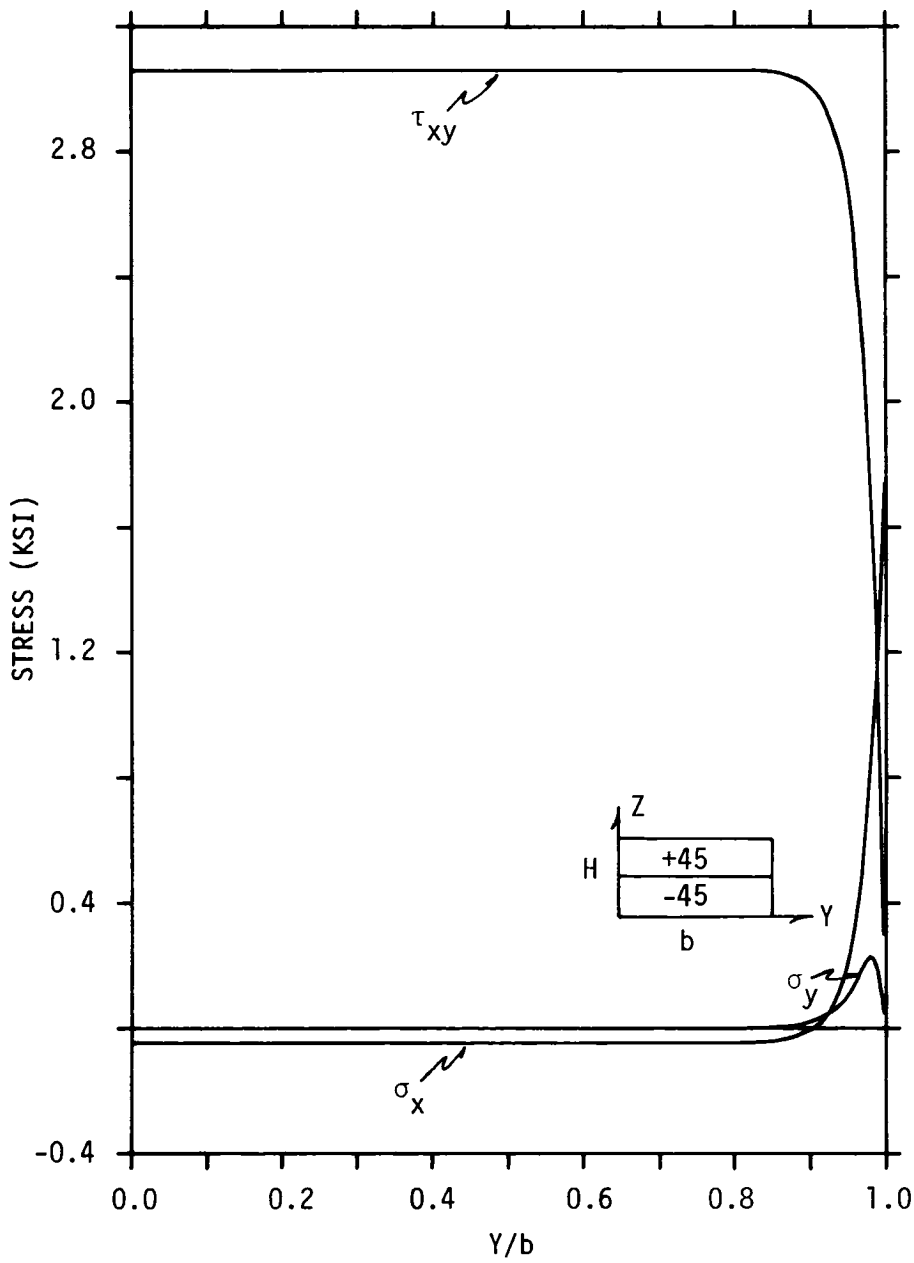

FIGURE 23. LAMINATE CURING STRESSES IN THE -45° LAYER OF A $[\pm 45]_s$ GR/E LAMINATE

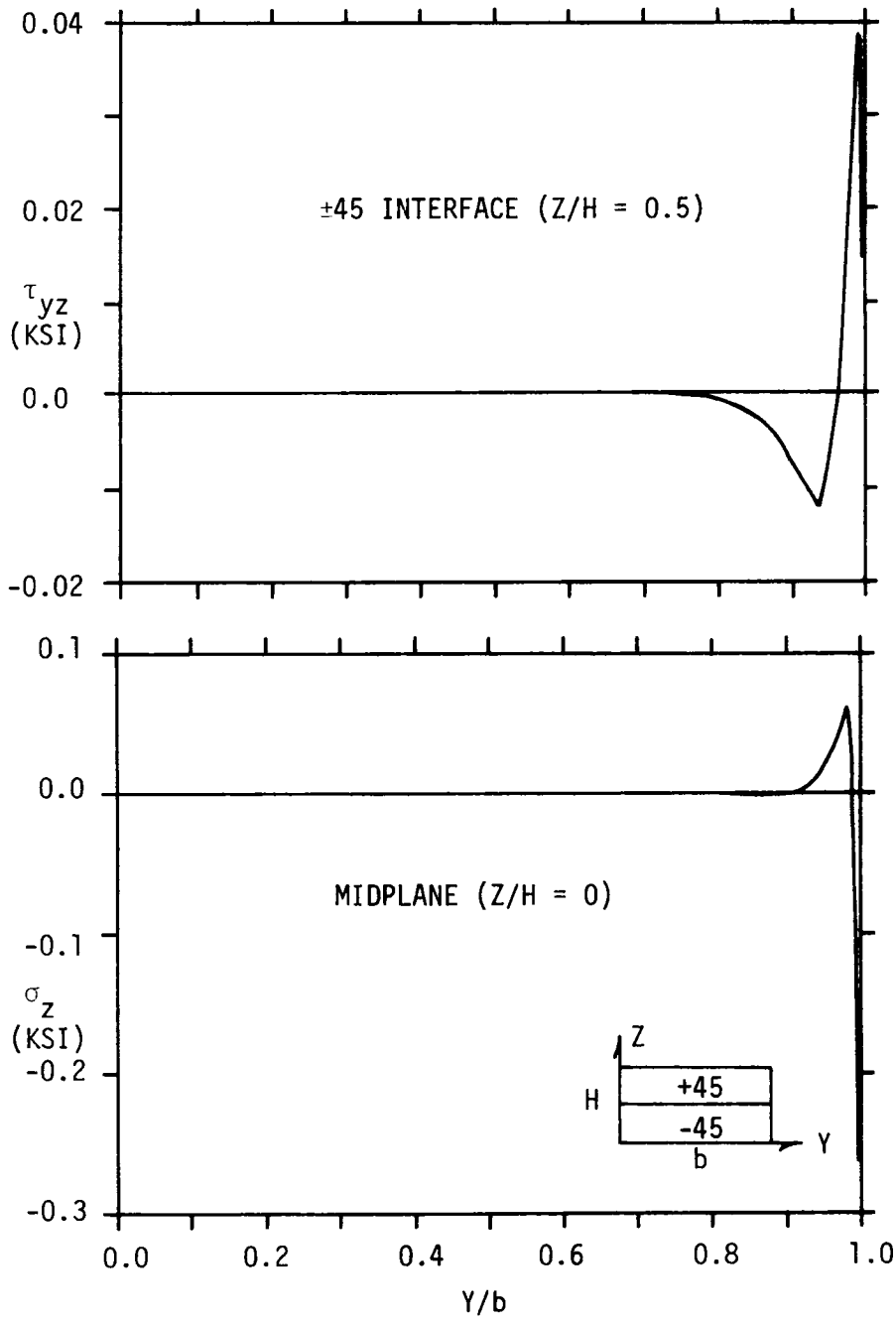

FIGURE 24. RESIDUAL σ_z AND τ_{yz} STRESSES IN A $[\pm 45]_s$ GR/E LAMINATE

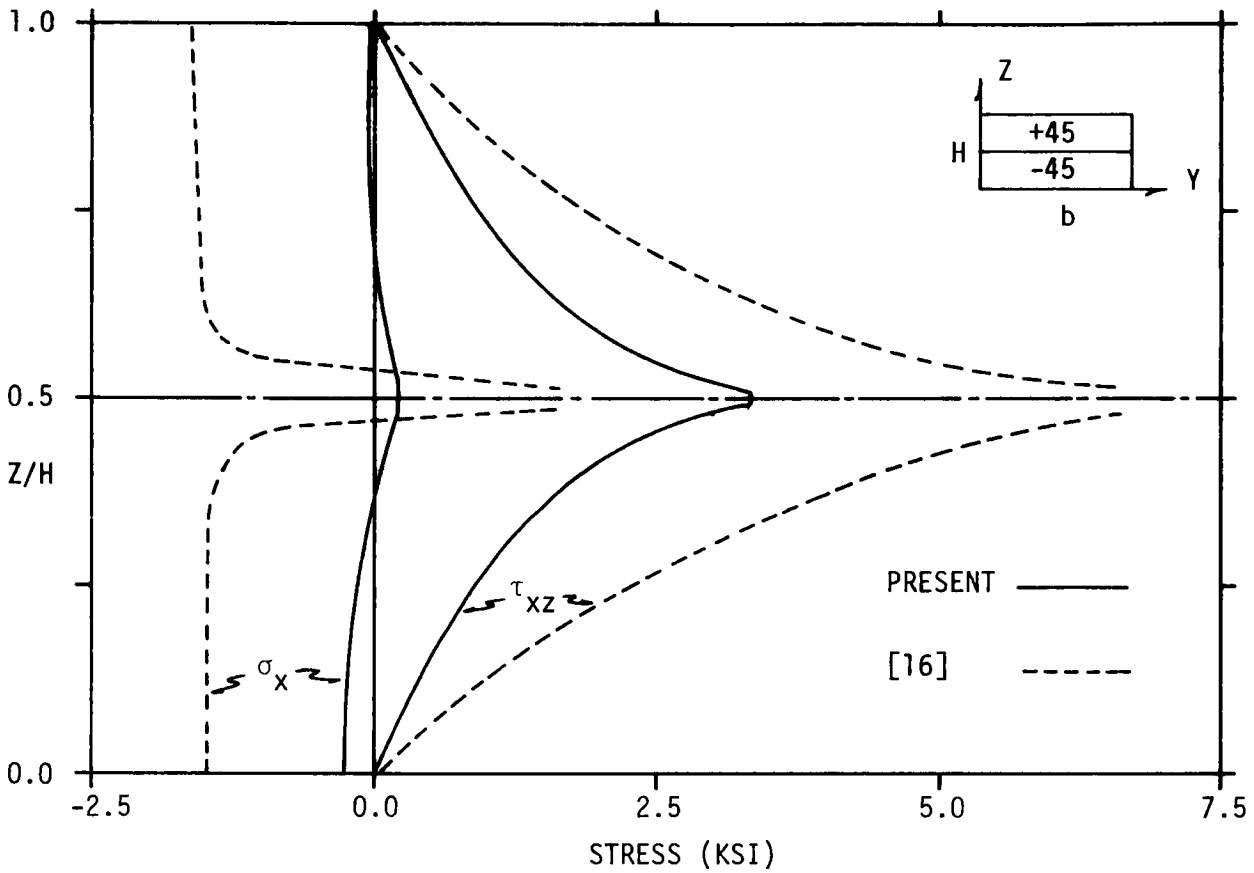

FIGURE 25. THROUGH-THE-THICKNESS DISTRIBUTIONS FOR THE RESIDUAL σ_x AND τ_{xz} ALONG THE FREE EDGE IN A $[\pm 45]_s$ GR/E LAMINATE

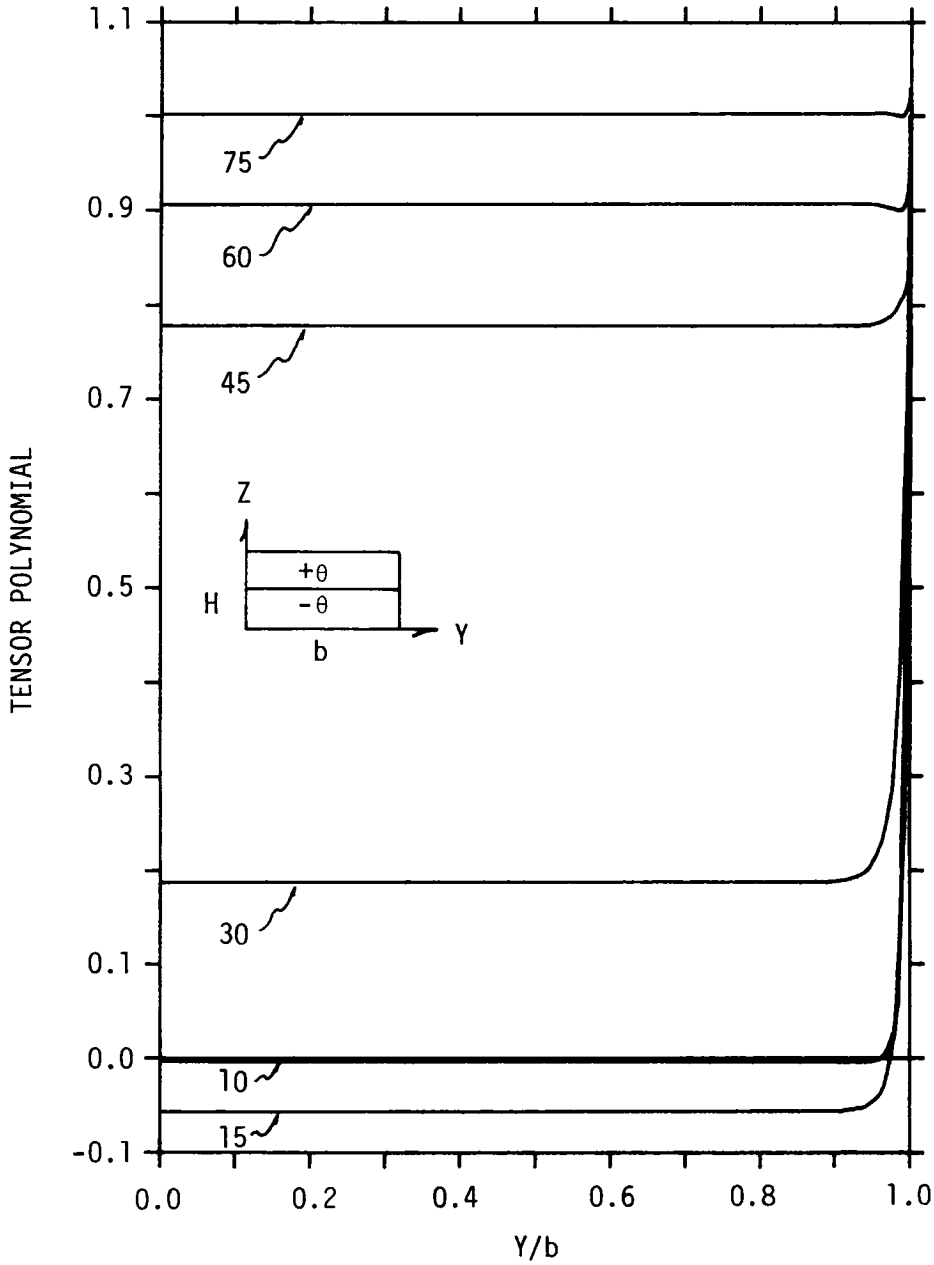

FIGURE 26. TENSOR POLYNOMIAL ALONG THE INTERFACE OF $[\pm\theta]_s$ LAMINATES AT 1ST FAILURE FOR THERMO-MECHANICAL LOADING

in an edge mode for small fiber angles and in a laminate mode for large fiber angles.

Thermal stresses in angle-ply laminates are an edge effect. This is clearly seen from Fig. 27, where the tensor polynomial has been plotted through the thickness along the free edge for several fiber angles, for the curing stresses as well as for the stress state existing at first failure. The presence of the free edge and dissimilarity of material causes additional stress gradients at the interface. Failure is predicted to initiate at the interface for low angles, shift to the midplane at 45°, and shift back to the interface for angles greater than 45°. The maximum value of the tensor polynomial for thermal loading occurs at θ=45° where the property mismatch is largest.

The stress state of the element where first failure was predicted was transformed into the material coordinate system and the individual terms of the tensor polynomial evaluated and presented in Table 5. The tensor polynomial is completely dominated by τ_{13} for the 10° and 15° degree laminates, and the mode of failure is therefore predicted to be transverse shear. With increasing angle, the contribution of τ_{13} decreases while that from τ_{23} and τ_{12} increase and the mode of failure continues to be transverse shear up to θ=30°. At 45°, the polynomial is dominated by the σ_2 terms, though there is significant contribution from τ_{12} which decreases with further increase in fiber angle. The failure mode for angles equal to or greater than 45° is predicted to be transverse tension.

Failure was predicted to initiate at the free edge for all

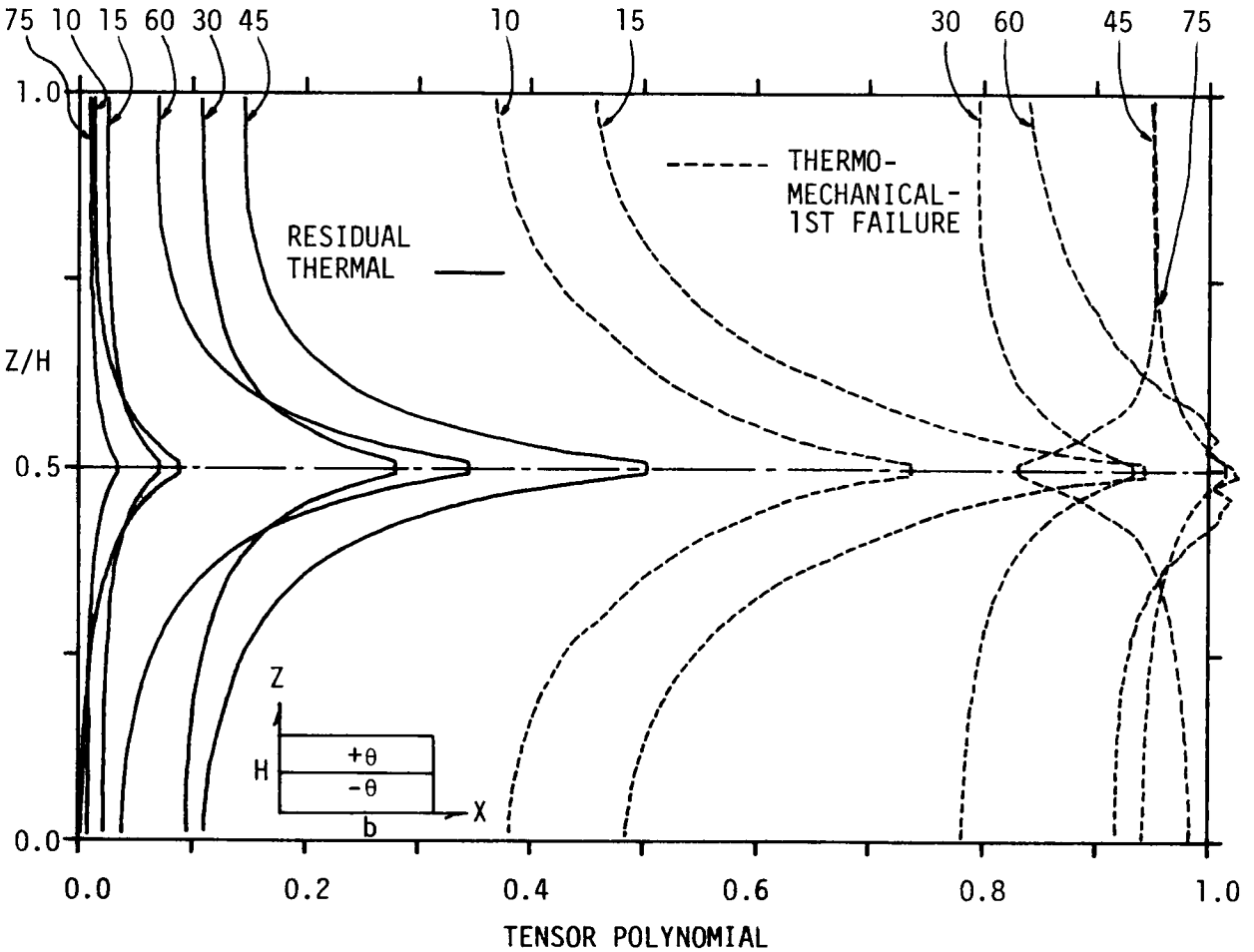

FIGURE 27. THROUGH-THE-THICKNESS TENSOR POLYNOMIAL DISTRIBUTIONS FOR CURING STRESSES AND STRESSES AT FIRST FAILURE IN ANGLE-PLY LAMINATES

TABLE 5

INDIVIDUAL TERMS OF THE TENSOR POLYNOMIAL AT FAILURE

Laminate	$F_1\sigma_1$	$F_{11}\sigma_1^2$	$F_2\sigma_2$	$F_{22}\sigma_2^2$	$F_3\sigma_3$	$F_{33}\sigma_3^2$	$F_{44}\tau_{23}^2$	$F_{55}\tau_{13}^2$	$F_{66}\tau_{12}^2$
$[\pm 10]_s$	.0273	.0576	-.0715	.0025	.0079	.0000	.0494	.9016	.0216
$[\pm 15]_s$	.0231	.0409	-.1043	-.0054	-.0101	.0001	.1145	.8808	.0443
$[\pm 30]_s$	.0163	.0204	-.1241	.0076	-.0729	.0026	.3305	.5382	.2750
$[\pm 45]_s$	.0027	.0005	.6070	.1823	.0315	.0005	.0000	.0000	.1793
$[\pm 60]_s$	-.0003	.0000	.6770	.2266	.0302	.0005	.0311	.0048	.0300
$[\pm 75]_s$	-.0002	.0000	.7135	.2517	.0115	.0001	.0179	.0006	.0048

laminates studied. In the 10° and 15° laminates first failure initiated at 0.003 percent strain, in the 45° at 0.0045 percent strain and at 0.004 for the 30°, 60° and 75° laminates. The strains at which first failure is predicted is the same for some laminates because the strain was applied in load steps of 0.05 percent. Linear elastic results in [25] indicated that the $[\pm 15]_s$ laminate was the most critical and that the strain to failure increased with increasing fiber angle.

5.3 Quasi-Isotropic Laminates

5.3.1 Stress Distributions

The quasi-isotropic laminates analyzed were the $[\pm 45/0/90]_s$ and the $[90/0/\pm 45]_s$. Laminate and interlaminar stresses for residual thermal and first failure under thermo-mechanical loading are presented in Figs. 28-33. Axial (σ_x) and transverse (σ_y) stresses in the 90° layer of both laminates are shown in Figs. 28 and 29, respectively. The results show a strong edge effect in σ_x which is tensile, and thus leads to early transverse tension failure at the free edge. The width of the boundary layer for thermo-mechanical loading is significantly larger than that for thermal loading. This is believed to be a manifestation of nonlinear material behavior. The residual stresses are shown to make a significant contribution to the stress state that exists when failure initiates.

Various interlaminar stresses are plotted at different interfaces of both laminates in Figs. 30 and 31. As indicated in the figure, the edge effects extend further into the interior for thermo-mechanical loading than they do for purely thermal loading as was the case for

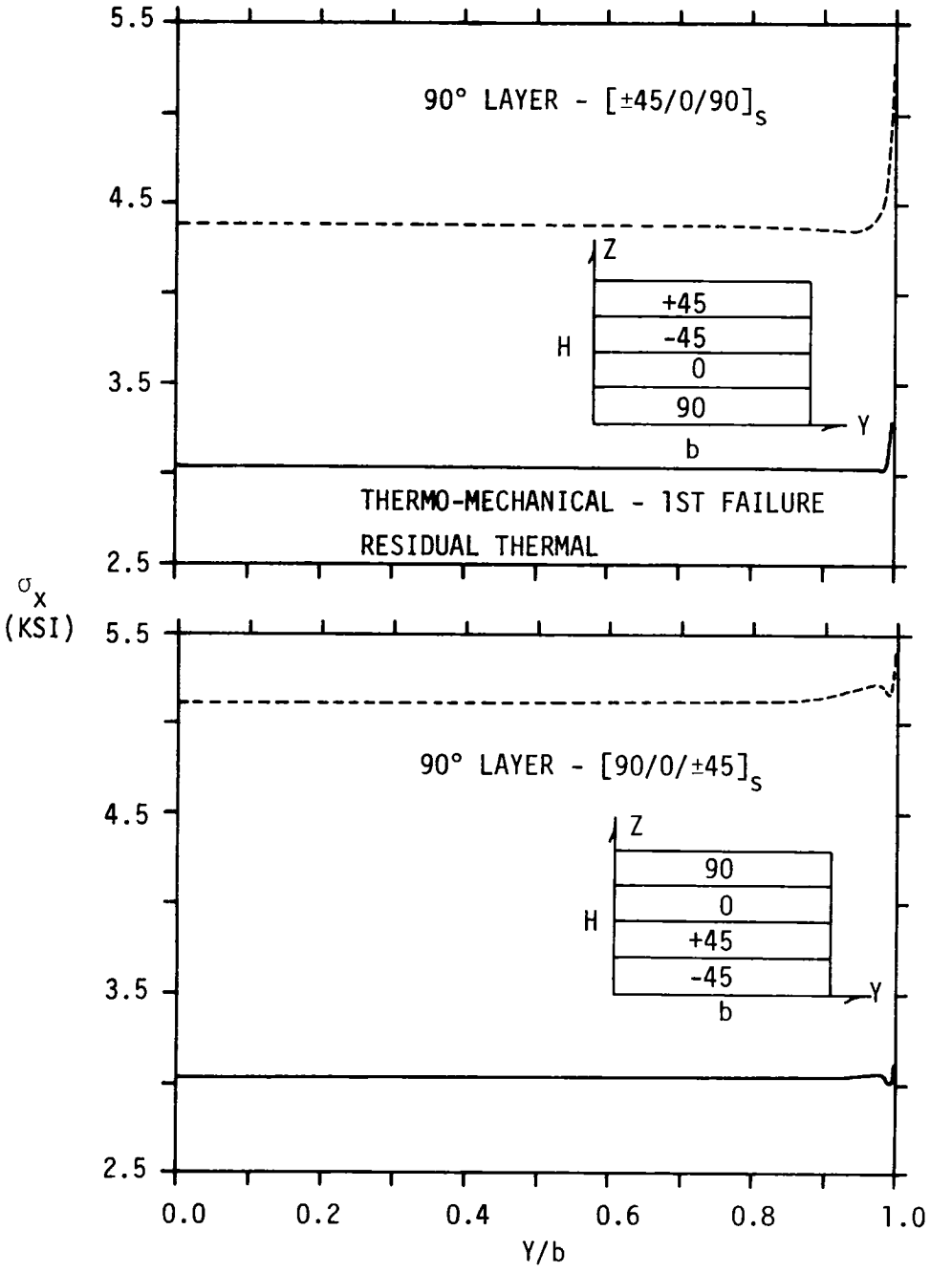

FIGURE 28. σ_x IN THE 90° LAYER OF $[\pm 45/0/90]_s$ AND $[90/0/\pm 45]_s$ LAMINATES

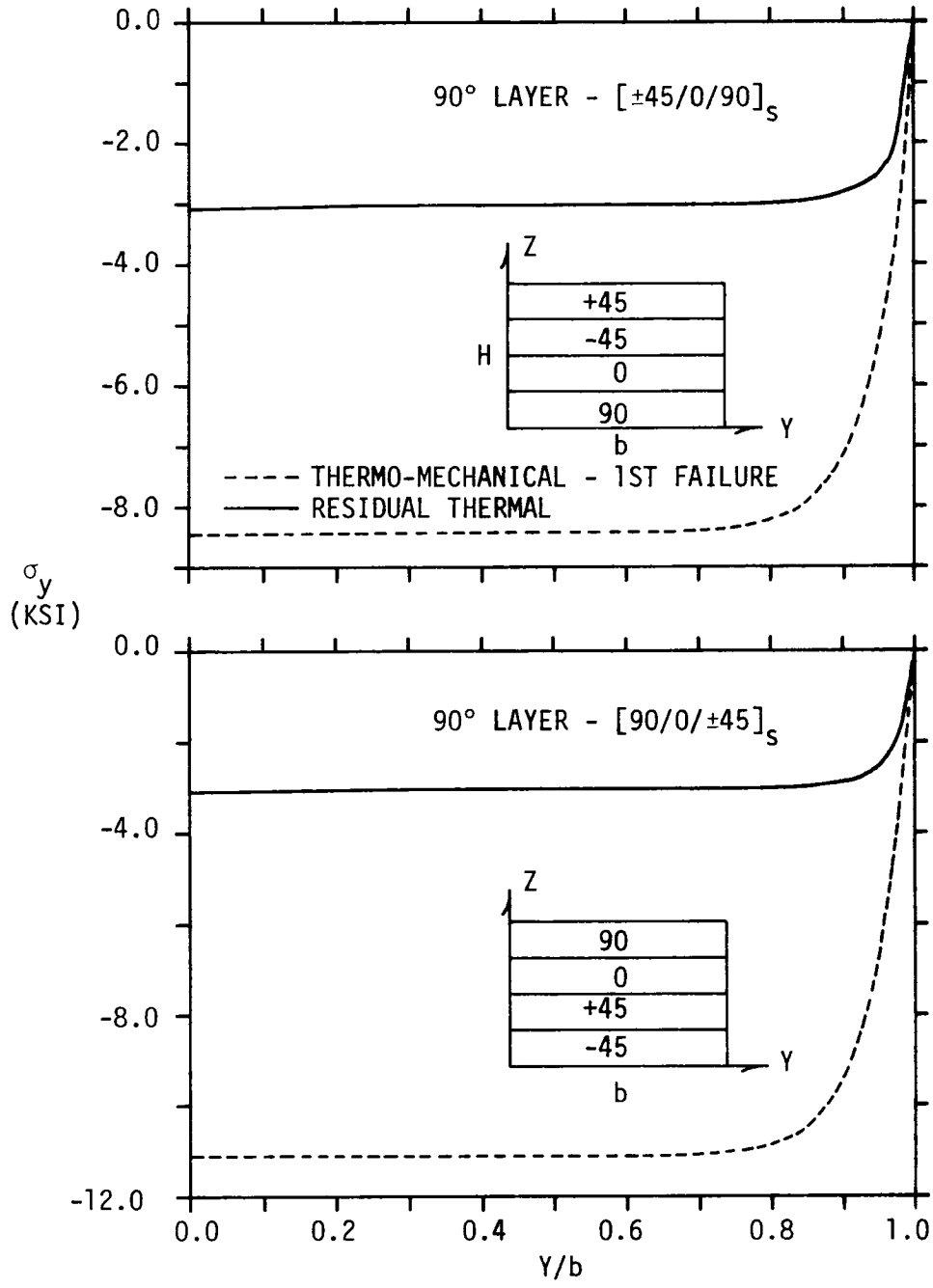

FIGURE 29. σ_y IN THE 90° LAYER OF $[\pm 45/0/90]_s$ AND $[90/0/\pm 45]_s$ LAMINATES

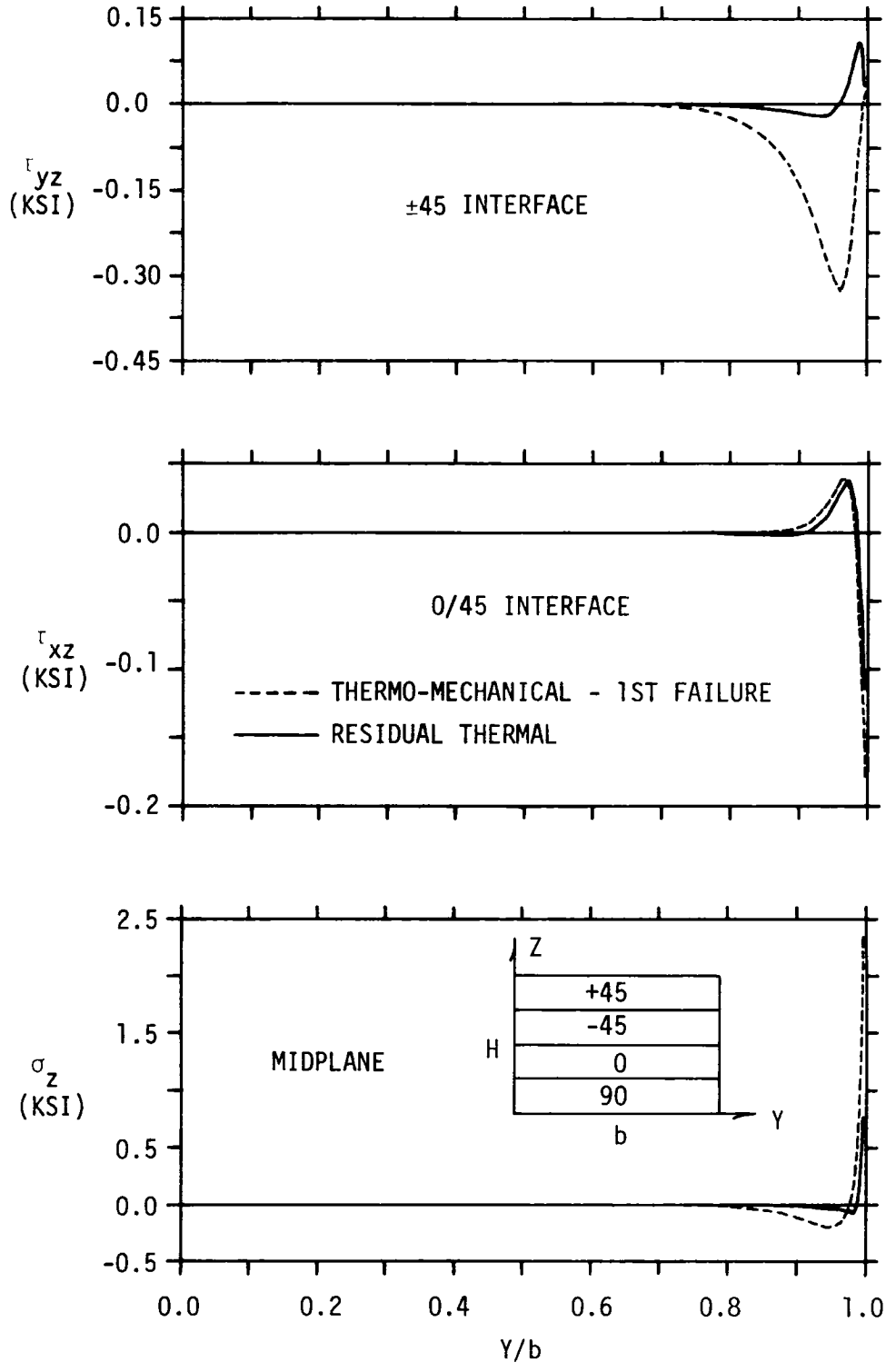

FIGURE 30. INTERLAMINAR STRESSES IN A $[\pm 45/0/90]_s$ LAMINATE

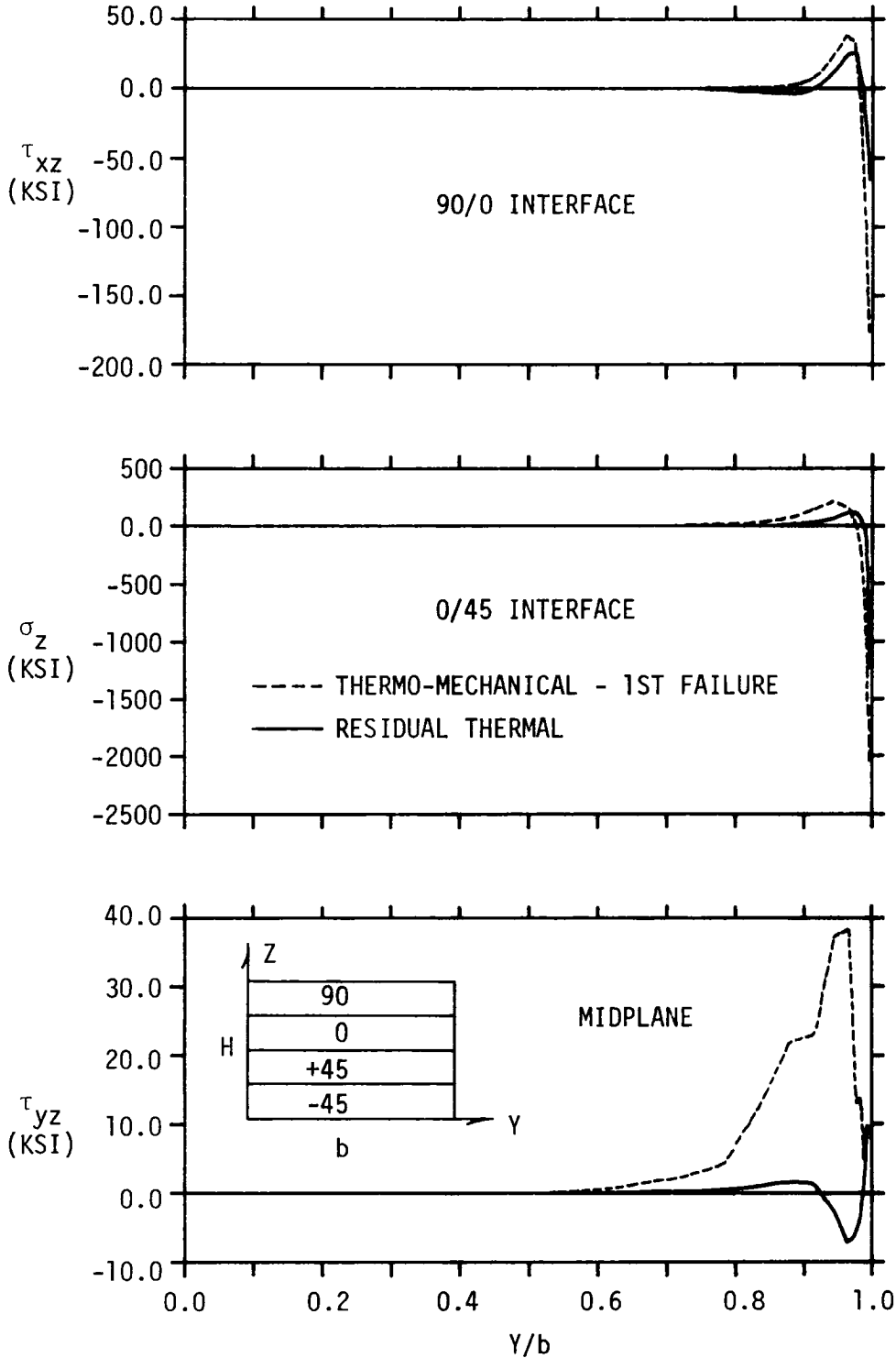

FIGURE 31. INTERLAMINAR STRESSES IN A $[90/0/\pm45]_s$ LAMINATE

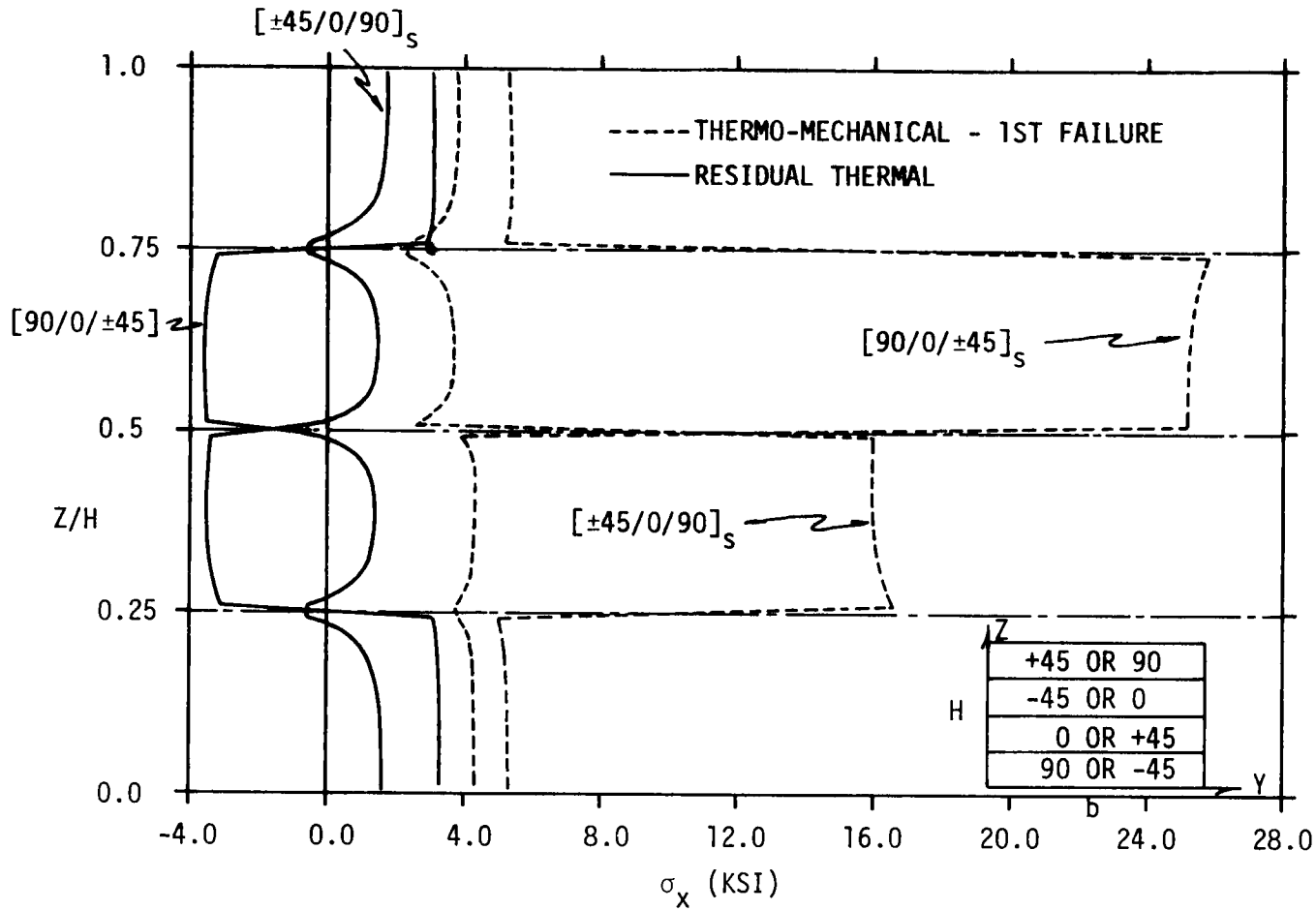

FIGURE 32. THROUGH-THE-THICKNESS σ_x DISTRIBUTION AT THE EDGE OF $[\pm 45/0/90]_s$ AND $[90/0/\pm 45]_s$ LAMINATES

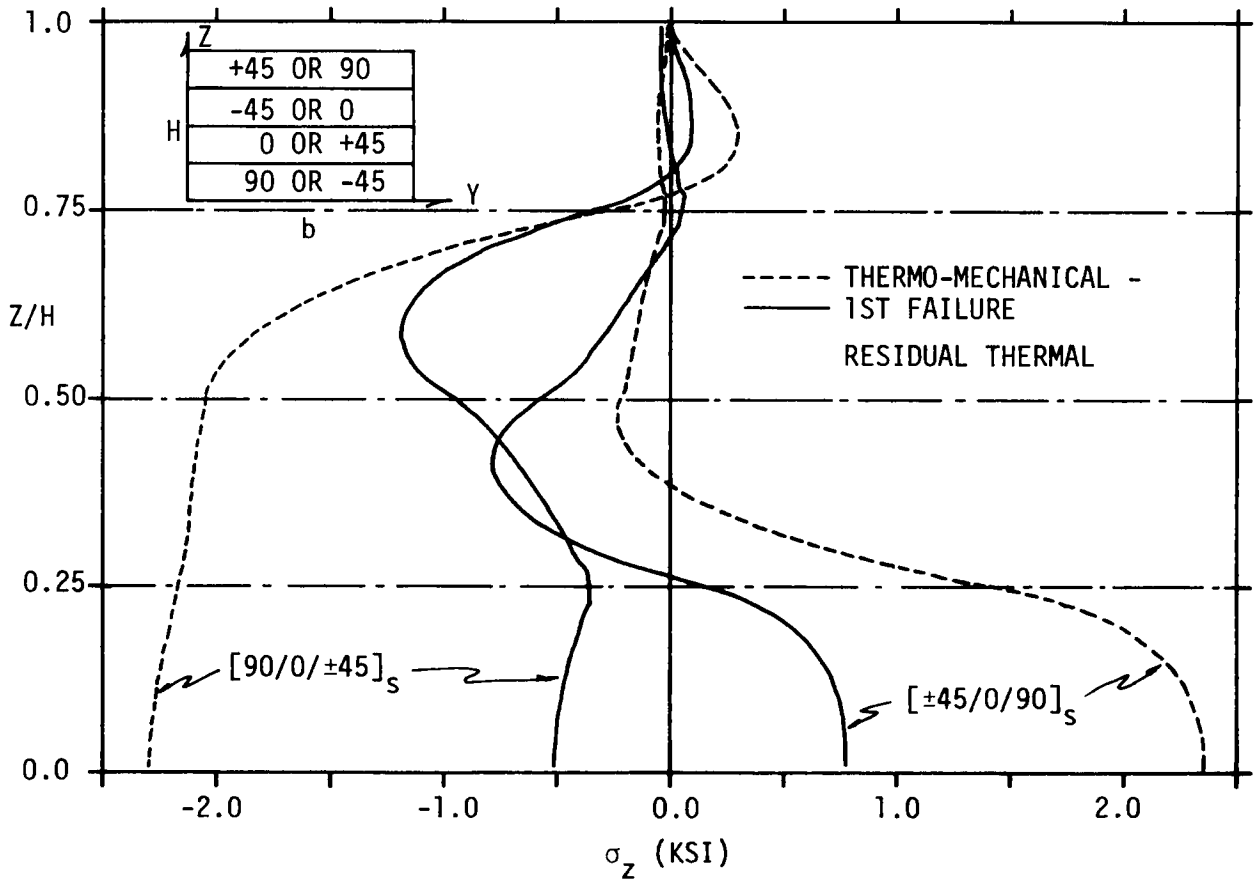

FIGURE 33. THROUGH-THE-THICKNESS σ_z DISTRIBUTION AT THE EDGE OF $[\pm 45/0/90]_s$ AND $[90/0/\pm 45]_s$ LAMINATES

laminate stresses. Though τ_{yz} tends to zero at the boundary, τ_{xz} and σ_z are singular at the free edge. This was the case at all interfaces except the 90/0 interface where σ_z reverses sign from its large negative value, tending to zero or some tensile value at the free edge. Such a behavior was also predicted for a $[90/0]_s$ laminate (Figs. 5 and 14).

Through-the-thickness distributions of σ_x and σ_z are presented for thermal and thermo-mechanical loading in Figs. 32 and 33. The σ_x stress distributions show the unloading of the 0° layers with the application of mechanical load. However, this positive feature of thermal stress is offset by the fact that the thermal stress has the same sign as the stress due to mechanical in the 90° layers and, therefore, contributes to early failure in that layer. The σ_z distributions show that the signs of the stresses due to thermal and thermo-mechanical are the same. The interlaminar normal stresses are predominately compressive for these two stacking sequences and, therefore, do not contribute to delamination. The only exception being near the midplane of the $[\pm 45/0/90]_s$ laminate. It would appear from these results that, of the two, the $[90/0/\pm 45]_s$ is the preferred laminate for tensile loading.

5.3.2 Failure Analysis

The distribution of the tensor polynomial in the 90° layer adjacent to the 0/90 interface of both laminates is shown in Fig. 34 and the through-the-thickness distributions near the free edge are shown in Fig. 35. Both figures show results for residual thermal and thermo-

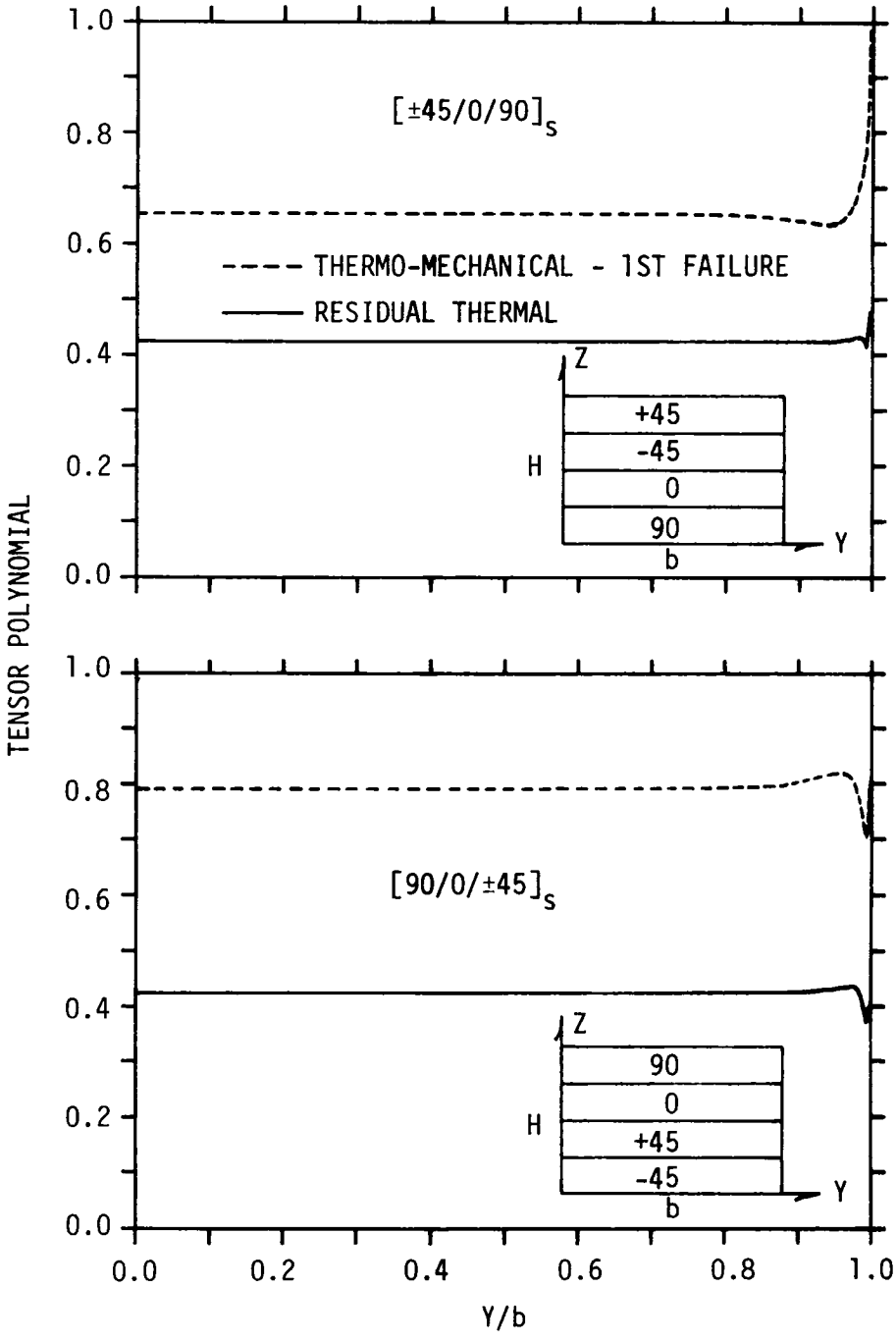

FIGURE 34. TENSOR POLYNOMIAL IN THE 90° LAYER ALONG THE 0/90 INTERFACE IN $[\pm 45/0/90]_s$ AND $[90/0/+45]_s$ LAMINATES

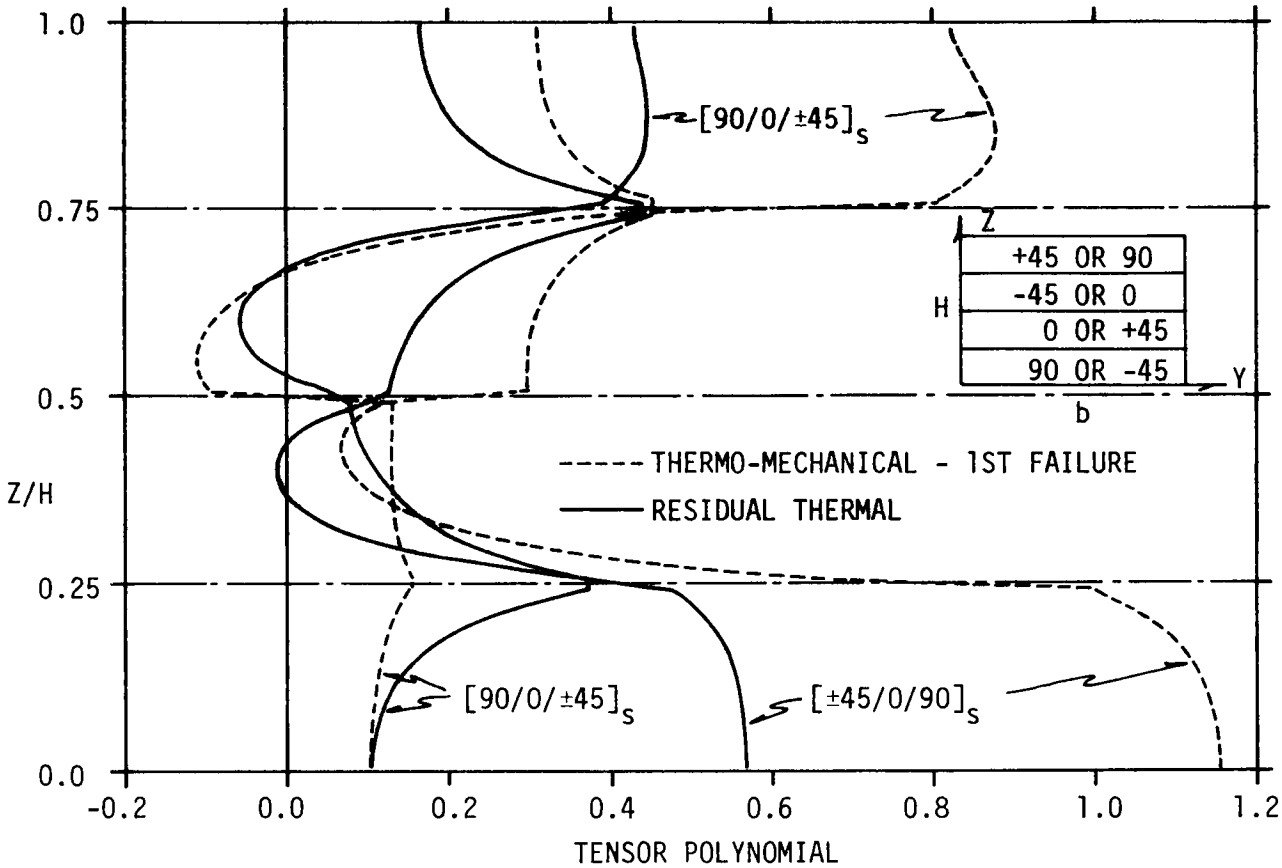

FIGURE 35. THROUGH-THE-THICKNESS TENSOR POLYNOMIAL DISTRIBUTION IN $[\pm 45/0/90]_s$ AND $[90/0/\pm 45]_s$ LAMINATES

mechanical loading. The 90° layer was chosen for illustration because, as indicated in Fig. 35, the polynomial attains its largest value in this layer. The distributions in Fig. 34 show that the polynomial attains its maximum at the free edge. A boundary layer effect is very evident with the width at the boundary layer for thermo-mechanical loading being several times that for thermal loading. This figure also shows that thermal effects make a significant contribution to the tensor polynomial, and that the boundary layer effects are much stronger in the $[\pm 45/0/90]_s$ laminate.

The through-the-thickness distributions in Fig. 35 indicate that, for both laminates, the maximum value of the polynomial occurs within the 90° layer as opposed to the 0/90 interface. In the $[90/0/\pm 45]_s$ laminate, the maximum value is just below the midpoint of the layer thickness. In the $[\pm 45/0/90]_s$, the maximum value is at the center of the 90° layer, the midplane.

The terms making significant contributions to the tensor polynomial at failure (in material coordinates) are presented in Table 6 for the element that was the first to fail in each laminate. These results show that there is significant difference in the mode of first failure of the two quasi-isotropic laminates. The $[\pm 45/0/90]_s$ laminate fails in a mixed σ_2-σ_3 mode whereas the $[90/0/\pm 45]_s$ laminate fails in a predominately σ_2 mode. The influence of the higher interlaminar normal stress in the $[\pm 45/0/90]_s$ is shown to lead to failure at a lower applied strain.

TABLE 6

FAILURE MODE ANALYSIS OF QUASI-ISOTROPIC LAMINATES

Laminate	$F_2\sigma_2$	$F_{22}\sigma_2^2$	$F_3\sigma_3$	$F_{33}\sigma_3^2$	$F_2\sigma_2+F_{22}\sigma_2^2$	$F_3\sigma_3+F_{33}\sigma_3^2$	ε at First Failure
$[\pm 45/0/90]_s$	.5228	.1351	.2992	.0443	.6579	.3435	.001
$[90/0/\pm 45]_s$	.6606	.2157	.1174	.0068	.8762	.1242	.0015

6. CONCLUSIONS

The present analysis has concentrated on the evaluation of residual thermal stresses induced during curing of composites and thermo-mechanical stresses due to combined thermal/mechanical loading. Particular attention was given to the influence that boundary layer effects near the free edge have on the initiation of failure in angle-ply, cross-ply and quasi-isotropic laminate as predicted by the tensor polynomial failure criterion. The following conclusions can be drawn as a result of the study.

1. Mesh size has a significant effect on the stress values obtained from a finite element investigation of the stress distribution near the edge of a finite width laminated composite.
2. Thermal effects are significant in the boundary layer of laminated composites.
3. The boundary layer stress distribution in cross-ply laminates is very dependent on the stacking sequence. For linear elastic material behavior, both $[0/90]_s$ and $[90/0]_s$ laminates exhibit tensile interlaminar normal stress at the free edge.
4. Failure in a $[0/90]_s$ laminate initiates at approximately one-third the initial failure strain of a $[90/0]_s$ laminate under tensile load.

5. Failure of cross-ply laminates initiates at the free edge within the 90° layer, not at the 0/90 interface.
6. Failure of a $[0/90]_s$ laminate is a mixed mode in σ_2-σ_3 whereas the $[90/0]_s$ laminate fails primarily due to transverse tension (σ_2).
7. The stress behavior in angle-ply laminates is fundamentally different for thermal and mechanical loading. The $[\pm45]_s$ laminate is most critical for thermal loading, but the $[\pm15]_s$ laminate is most critical for tensile loading.
8. Angle-ply laminates with small fiber angles fail due to interlaminar shear whereas laminates with large fiber angles fail due to transverse tension.
9. Failure of angle-ply laminates initiates at the free edge. For small and large fiber angles, failure initiates at the $\pm\theta$ interface. For intermediate angles, failure initiates at the midplane.
10. Two modes of failure are predicted for angle ply laminates, an edge mode for fiber angles equal to or less than 30° and a laminate mode for angles equal to or greater than 45°.
11. Failure in the $[\pm45/0/90]_s$ and $[90/0/\pm45]_s$ laminates initiates at the free edge near the center of the 90° layer(s). The $[\pm45/0/90]_s$ fails at a lower applied strain in a mixed σ_2-σ_3 mode whereas the

$[90/0/\pm45]_s$ laminate fails primarily in a transverse tension mode.

BIBLIOGRAPHY

1. Renieri, G. D., Herakovich, C. T., "Nonlinear Analysis of Laminated Fibrous Composites," VPI&SU Report VPI-E-76-10, June, 1976.

2. Humphreys, E. A., Herakovich, C. T., "Nonlinear Analysis of Bonded Joints with Thermal Effects," VPI&SU Report VPI-E-77-19, June, 1977.

3. O'Brien, D. A., Herakovich, C. T., "Finite Element Analysis of Idealized Composite Damage Zones," VPI&SU Report VPI-E-78-6, February, 1978.

4. Reifsnider, K. L., Henneke, E. G. II, Stinchcomb, W. W., "Delamination in Quasi-isotropic Graphite-Epoxy Laminates," Composite Materials: Testing and Design (Fourth Conference), ASTM STP 617, American Society for Testing and Materials, 1977, pp. 93-105.

5. Herakovich, C. T., Davis, J. G., Jr. and Mills, J. G., "Thermal Microcracking in Celion 6000/PMR-15 Graphite/Polyimide," Proc. of the International Conference on Thermal Stresses in Materials and Structures in Severe Thermal Environments, Blacksburg, Va., March, 1980.

6. Tsai, S. W., "Strength Characteristics of Composite Materials," NASA CR-224, April, 1965.

7. Hashin, Z., "Theory of Fiber Reinforced Materials," NASA NAS1-8818, November 1970.

8. Chamis, C. C., "Proceedings of the 26th Annual Conference of the SPI Reinforced Plastics/Composite Institute," Section 18-D, Society of the Plastics Industry, Inc., N.Y., 1971, pp. 1-12.

9. Daniel, I. M., Liber, T., Lamination Residual Stresses in Fiber Composites," NASA CR-134 826, March 1975.

10. Herakovich, C. T., "On Thermal Edge Effects in Composite Laminates," Int. J. Mech. Sci., Vol. 18, pp. 129-134, 1976.

11. Hahn, H. T., Pagano, N. J., "Curing Stresses in Composite Laminates," J. Comp. Mat., Vol. 9, 1975, pp. 91-106.

12. Daniel, I. M., Liber, T., Chamis, C. C., "Measurement of Residual Strains in Boron-Epoxy and Glass-Epoxy Laminates," Composite Reliability, ASTM STP 580, American Society for Testing Materials, 1975, pp. 340-351.

13. Chamis, C. C., Sullivan, T. L., "A Computational Procedure to Analyse Metal Matrix Composites with Nonlinear Residual Strains," Composite Reliability, ASTM STP 580, American Society for Testing Materials, 1975, pp. 327-339.

14. Hahn, H. T., "Residual Stresses in Polymer Matrix Composite Laminates," J. Comp. Mat., Vol. 10, 1976, pp. 226-278.

15. Daniel, I. M., Liber, T., "Effect of Laminate Construction on Residual Stresses in Graphite/Polyimide Composites," Experimental Mechanics, January, 1977, pp. 21-25.

16. Wang, A. S. D., Crossman, F. W., "Edge Effects on Thermally Induced Stresses in Composite Laminates," J. Comp. Mat., Vol. 11, 1977, pp. 300-312.

17. Chamis, C. C., "Residual Stresses in Angle-plied Laminates and Their Effects on Laminate Behavior," NASA TM-78835.

18. Pagano, N. J., Hahn, H. T., "Evaluation of Composite Curing Stresses," Composite Materials; Testing and Design, ASTM STP 617, American Society for Testing Materials, 1977, pp. 317-329.

19. Farley, G. L., Herakovich C. T., "Influence of Two-Dimensional Hygrothermal Gradients on Interlaminar Stresses Near Free Edges, Advanced Composite Materials - Environmental Effects," ASTM STP 658, American Society for Testing and Materials, 1978, pp. 143-159.

20. Kim, R. Y., Hahn, H. T., "Effect of Curing Stresses on the First Ply-failure in Composite Laminates," J. Comp. Mat., Vol. 13, 1979, pp. 2-16.

21. Pipes, R. B., Pagano, N. J., "Interlaminar Stresses in Composite Laminates under Uniform Axial Tension," J. Comp. Mat., Vol. 4, 1970, pp. 538-548.

22. Pipes, R. B., Daniel, I. M., "Moire Analysis of the Interlaminar Shear Edge Effect in Laminated Composites," J. Comp. Mat., Vol. 5, 1971, pp. 225-259.

23. Ramberg, W., Osgood, W. B., "Description of Stress-Strain Curves by Three Parameters," NASA TN 902, 1943.

24. Tsai, S. W., Wu, E. M., "A General Theory of Strength for Anisotropic Materials," J. Comp. Mat., Vol. 5, 1971, pp. 58-80.

25. Herakovich, C. T., Nagarkar, A., O'Brien, D. A., "Failure Analysis of Composite Laminates with Free Edges," Modern Developments in Composite Materials and Structures, J. R. Vinson, ed., ASME, 1979.

26. Bergner, H. W., Davis, J. G., Herakovich, C. T., "Analysis of Shear Test Methods for Composite Materials," VPI-E-77-14, April 1977.

27. Wang, J. T. S., Dickson, J. N., "Interlaminar Stresses in Symmetric Composite Laminates," J. Comp. Mat., Vol. 12, 1978, pp. 390-402.

28. Wang, A. S. D., Crossman, F. W., "Some New Results on Edge Effects in Symmetric Composite Laminates," J. Comp. Mat., Vol. 11, 1977, pp. 92-106.

29. Jones, R. M., Mechanics of Composite Materials, Scripta Book Company, Washington, D. C., 1975.

APPENDIX A

CONSTITUTIVE RELATIONS

APPENDIX A

CONSTITUTIVE RELATIONS

The constitutive relationship for an orthotropic material in the principal material directions can be written

$$\{\sigma\}_1 = [C](\{\varepsilon\}_1 - \{\alpha\}_1 \Delta T)$$

where

$$[C] = \begin{bmatrix} C_{11} & C_{12} & C_{13} & 0 & 0 & 0 \\ & C_{22} & C_{23} & 0 & 0 & 0 \\ & & C_{33} & 0 & 0 & 0 \\ & & & C_{44} & 0 & 0 \\ \text{Symmetric} & & & & C_{55} & 0 \\ & & & & & C_{66} \end{bmatrix}$$

$$\{\sigma\}_1 = \begin{Bmatrix} \sigma_1 \\ \sigma_2 \\ \sigma_3 \\ \tau_{23} \\ \tau_{13} \\ \tau_{12} \end{Bmatrix} \qquad \{\varepsilon\}_1 = \begin{Bmatrix} \varepsilon_1 \\ \varepsilon_2 \\ \varepsilon_3 \\ \gamma_{23} \\ \gamma_{13} \\ \gamma_{12} \end{Bmatrix}$$

$$\{\alpha\}_1 = \begin{Bmatrix} \alpha_1 \\ \alpha_2 \\ \alpha_3 \\ 0 \\ 0 \\ 0 \end{Bmatrix}$$

For a θ rotation about the 3 (z) axis (Fig. 1), the constitutive relationship becomes

$$\{\sigma\} = [\bar{C}](\{\varepsilon\}-\{\alpha\}\Delta T)$$

where

$$[\bar{C}] = \begin{bmatrix} \bar{C}_{11} & \bar{C}_{12} & \bar{C}_{13} & 0 & 0 & \bar{C}_{16} \\ & \bar{C}_{22} & \bar{C}_{23} & 0 & 0 & \bar{C}_{26} \\ & & \bar{C}_{33} & 0 & 0 & \bar{C}_{36} \\ & & & \bar{C}_{44} & \bar{C}_{45} & 0 \\ \text{Symmetric} & & & & \bar{C}_{55} & 0 \\ & & & & & \bar{C}_{66} \end{bmatrix}$$

$$\{\sigma\} = \begin{Bmatrix} \sigma_x \\ \sigma_y \\ \sigma_z \\ \tau_{yz} \\ \tau_{xz} \\ \tau_{xy} \end{Bmatrix} \qquad \{\varepsilon\} = \begin{Bmatrix} \varepsilon_x \\ \varepsilon_y \\ \varepsilon_z \\ \gamma_{yz} \\ \gamma_{xz} \\ \gamma_{xy} \end{Bmatrix}$$

$$\{\alpha\} = \begin{Bmatrix} \alpha_x \\ \alpha_y \\ \alpha_z \\ 0 \\ 0 \\ \alpha_{xy} \end{Bmatrix}$$

and the various matrix and vector terms as functions of the principal material properties are given below ($m=\cos\theta$, $n=\sin\theta$).

$$\bar{C}_{11} = m^4C_{11}+2m^2n^2(C_{12}+2C_{66})+n^4C_{22}$$

$$\bar{C}_{12} = m^2n^2(C_{11}+C_{22}-4C_{66})+(m^4+n^4)C_{12}$$

$$\bar{C}_{13} = m^2C_{13}+n^2C_{23}$$

$$\bar{C}_{16} = -mn[m^2C_{11}-n^2C_{22}-(m^2-n^2)(C_{12}+2C_{66})]$$

$$\bar{C}_{22} = n^4C_{11}+2m^2n^2(C_{12}+2C_{66})+m^4C_{22}$$

$$\bar{C}_{23} = n^2C_{13}+m^2C_{23}$$

$$\bar{C}_{26} = -mn(n^2C_{11}-m^2C_{22})+(m^2-n^2)(C_{12}+2C_{66})$$

$$\bar{C}_{33} = C_{33}$$

$$\bar{C}_{36} = mn(C_{23}-C_{13})$$

$$\bar{C}_{44} = m^2C_{44}+n^2C_{55}$$

$$\bar{C}_{45} = mn(C_{44}-C_{55})$$

$$\bar{C}_{55} = n^2C_{44}+m^2C_{55}$$

$$\bar{C}_{66} = m^2n^2(C_{11}+C_{22}-2C_{12})+(m^2-n^2)^2C_{66}$$

$$\alpha_x = m^2\alpha_1 + n^2\alpha_2$$

$$\alpha_y = n^2\alpha_1 + m^2\alpha_2$$

$$\alpha_z = \alpha_3$$

$$\alpha_{xy} = -2mn(\alpha_1 - \alpha_2)$$

APPENDIX B

STIFFNESS MATRIX

APPENDIX B

STIFFNESS MATRIX

Equations (B.1) represent the equilibrium equations for applied strain loading. Equ's (B.2) represent the equilibrium equations in average force loadings. In these equations, [K] is the symmetric elemental stiffness matrix, $\varepsilon_x\{S\}$ and $\{T\}$ are force vectors corresponding to the applied strain and temperature change respectively, $\{F\}$ is the vector of applied forces, and $\{x\}$ is the vector of unknown nodal displacements.

$$\underset{(9x9)}{[K]^{(\ell)}}\underset{(9x1)}{\{x\}^{(\ell)}} + \varepsilon_x\underset{(9x1)}{\{S\}^{(\ell)}} = \underset{(9x1)}{\{F\}^{(\ell)}} \tag{B.1}$$

$$\underset{(10x10)}{[K]^{(\ell)}}\underset{(10x1)}{\{x\}^{(\ell)}} - \underset{(10x1)}{\{T\}^{(\ell)}} = \underset{(10x1)}{\{F\}^{(\ell)}} \tag{B.2}$$

Defining the following terms

$$a = (Z_2-Z_3)/2$$

$$b = (Y_3-Y_2)/2$$

$$c = (Z_3-Z_1)/2$$

$$d = (Y_1-Y_3)/2$$

$$e = (Z_1-Z_2)/2$$

$$g = (Y_2-Y_1)/2$$

A^{ℓ} = the area of element (ℓ)

F^{*} = average normal force

where Y_1 through Y_3 and Z_1 through Z_3 are the coordinates of the nodal points of element ℓ in the Y-Z plane, the element of the matricies of Equ. (B.1) can be defined as follows.

$$K_{11} = (\bar{C}_{55}b^2 + \bar{C}_{66}a^2)/A^{\ell} \qquad K_{22} = (\bar{C}_{55}d^2 + \bar{C}_{66}c^2)/A^{\ell}$$

$$K_{12} = (\bar{C}_{55}bd + \bar{C}_{66}ac)/A^{\ell} \qquad K_{23} = (\bar{C}_{55}dg + \bar{C}_{66}ce)/A^{\ell}$$

$$K_{13} = (\bar{C}_{55}bg + \bar{C}_{66}ae)/A^{\ell} \qquad K_{24} = (\bar{C}_{26}ac + \bar{C}_{45}db)/A^{\ell}$$

$$K_{14} = (\bar{C}_{26}a^2 + \bar{C}_{45}b^2)/A^{\ell} \qquad K_{25} = (\bar{C}_{26}c^2 + \bar{C}_{45}d^2)/A^{\ell}$$

$$K_{15} = (\bar{C}_{26}ca + \bar{C}_{45}bd)/A^{\ell} \qquad K_{26} = (\bar{C}_{26}ec + \bar{C}_{45}dg)/A^{\ell}$$

$$K_{16} = (\bar{C}_{26}ea + \bar{C}_{45}bg)/A^{\ell} \qquad K_{27} = (\bar{C}_{36}bc + \bar{C}_{45}da)/A^{\ell}$$

$$K_{17} = (\bar{C}_{36}ba + \bar{C}_{45}ba)/A^{\ell} \qquad K_{28} + (\bar{C}_{36}dc + \bar{C}_{45}dc)/A^{\ell}$$

$$K_{18} = (\bar{C}_{36}da + \bar{C}_{45}bc)/A^{\ell} \qquad K_{29} = (\bar{C}_{36}gc + \bar{C}_{45}de)/A^{\ell}$$

$$K_{19} = (\bar{C}_{36}ga + \bar{C}_{45}be)/A^{\ell}$$

$$K_{33} = (\bar{C}_{55}g^2 + \bar{C}_{66}e^2)/A^{\ell} \qquad K_{44} = (\bar{C}_{22}a^2 + \bar{C}_{44}b^2)/A^{\ell}$$

$$K_{34} = (\bar{C}_{26}ae + \bar{C}_{45}gb)/A^{\ell} \qquad K_{45} = (\bar{C}_{22}ac + \bar{C}_{44}bd)/A^{\ell}$$

$$K_{35} = (\bar{C}_{26}ce + \bar{C}_{45}bd)/A^{\ell} \qquad K_{46} = (\bar{C}_{22}ae + \bar{C}_{44}bg)/A^{\ell}$$

$$K_{36} = (\bar{C}_{26}e^2 + \bar{C}_{45}g^2)/A^{\ell} \qquad K_{47} = (\bar{C}_{44}ba + \bar{C}_{23}ab)/A^{\ell}$$

$$K_{37} = (\bar{C}_{36}be + \bar{C}_{45}ga)/A^{\ell} \qquad K_{48} = (\bar{C}_{44}bc + \bar{C}_{23}ad)/A^{\ell}$$

$$K_{38} = (\bar{C}_{36}de + \bar{C}_{45}gc)/A^{\ell} \qquad K_{49} = (\bar{C}_{44}be + \bar{C}_{23}ag)/A^{\ell}$$

$$K_{39} = (\bar{C}_{36}ge + \bar{C}_{45}ge)/A^{\ell}$$

$$K_{55} = (\bar{C}_{22}c^2 + \bar{C}_{44}d^2)/A^{\ell} \qquad K_{66} = (\bar{C}_{22}e^2 + \bar{C}_{44}g^2)/A^{\ell}$$

$$K_{56} = (\bar{C}_{22}ce + \bar{C}_{44}dg)/A^{\ell} \qquad K_{67} = (\bar{C}_{44}ga + \bar{C}_{23}eb)/A^{\ell}$$

$$K_{57} = (\bar{C}_{44}da + \bar{C}_{23}cb)/A^{\ell} \qquad K_{68} = (\bar{C}_{44}gc + \bar{C}_{23}eg)/A^{\ell}$$

$$K_{58} = (\bar{C}_{44}dc + \bar{C}_{23}cd)/A^{\ell} \qquad K_{69} = (\bar{C}_{44}ge + \bar{C}_{23}eg)/A^{\ell}$$

$$K_{59} = (\bar{C}_{44}de + \bar{C}_{23}cg)/A^{\ell}$$

$$K_{77} = (\bar{C}_{33}b^2 + \bar{C}_{44}a^2)/A^{\ell} \qquad K_{88} = (\bar{C}_{33}d^2 + \bar{C}_{44}c^2)/A^{\ell}$$

$$K_{78} = (\bar{C}_{33}bd + \bar{C}_{44}ac)/A^{\ell} \qquad K_{89} = (\bar{C}_{33}dg + \bar{C}_{44}ce)/A^{\ell}$$

$$K_{79} = (\bar{C}_{33}bg + \bar{C}_{44}ae)/A^{\ell} \qquad K_{99} = (\bar{C}_{33}g^2 + \bar{C}_{44}e^2)/A^{\ell}$$

$$S_1 = \bar{C}_{16}\,a \qquad S_2 = \bar{C}_{16}\,c \qquad S_3 = \bar{C}_{16}\,e$$

$$S_4 = \bar{C}_{12}\,a \qquad S_5 = \bar{C}_{12}\,c \qquad S_6 = \bar{C}_{12}\,e$$

$$S_7 = \bar{C}_{13}\,b \qquad S_8 = \bar{C}_{13}\,d \qquad S_9 = \bar{C}_{13}\,g$$

$$x_1 = u_1 \qquad x_2 = u_2 \qquad x_3 = u_3$$

$$x_4 = v_1 \qquad x_5 = v_2 \qquad x_6 = v_3$$

$$x_7 = w_1 \qquad x_8 = w_2 \qquad x_9 = w_3$$

$$F_1 = f_x^1 \qquad F_2 = f_x^2 \qquad F_3 = f_x^3$$
$$F_4 = f_y^1 \qquad F_5 = f_y^2 \qquad F_3 = f_y^3$$
$$F_7 = f_z^1 \qquad F_8 = f_z^2 \qquad F_8 = f_z^3$$

where f's are nodal forces.

For Equ's. (B.2) the previously defined terms apply plus the following additional terms

$$K_{110} = \bar{C}_{16}a \qquad K_{210} = \bar{C}_{16}c \qquad K_{310} = \bar{C}_{16}e$$
$$K_{410} = \bar{C}_{12}a \qquad K_{510} = \bar{C}_{12}c \qquad K_{610} = \bar{C}_{16}e$$
$$K_{710} = \bar{C}_{13}b \qquad K_{810} = \bar{C}_{13}d \qquad K_{910} = \bar{C}_{13}g$$
$$K_{1010} = \bar{C}_{11}A^{\ell}$$

$$X_{10} = \bar{\xi}_x \qquad F_{10} = F^*$$

$$T_1 = (\bar{C}_{16}\varepsilon_x^T + \bar{C}_{26}\varepsilon_y^T + \bar{C}_{36}\varepsilon_z^T + \bar{C}_{66}\gamma_{xy}^T)a$$

$$T_2 = (\bar{C}_{16}\varepsilon_x^T + \bar{C}_{26}\varepsilon_y^T + \bar{C}_{36}\varepsilon_z^T + \bar{C}_{66}\gamma_{xy}^T)c$$

$$T_3 = (\bar{C}_{16}\varepsilon_x^T + \bar{C}_{26}\varepsilon_y^T + \bar{C}_{36}\varepsilon_z^T + \bar{C}_{66}\gamma_{xy}^T)e$$

$$T_4 = (\bar{C}_{12}\varepsilon_x^T + \bar{C}_{22}\varepsilon_y^T + \bar{C}_{23}\varepsilon_z^T + \bar{C}_{26}\gamma_{xy}^T)a$$

$$T_5 = (\bar{C}_{12}\varepsilon_x^T + \bar{C}_{22}\varepsilon_y^T + \bar{C}_{23}\varepsilon_z^T + \bar{C}_{26}\gamma_{xy}^T)c$$

$$T_6 = (\bar{C}_{12}\varepsilon_x^T + \bar{C}_{22}\varepsilon_y^T + \bar{C}_{23}\varepsilon_z^T + \bar{C}_{26}\gamma_{xy}^T)e$$

$$T_7 = (\bar{C}_{13}\varepsilon_x^T + \bar{C}_{23}\varepsilon_y^T + \bar{C}_{33}\varepsilon_z^T + \bar{C}_{36}\gamma_{xy}^T)b$$

$$T_8 = (\bar{C}_{13}\varepsilon_x^T + \bar{C}_{23}\varepsilon_y^T + \bar{C}_{33}\varepsilon_z^T + \bar{C}_{36}\gamma_{xy}^T)d$$

$$T_9 = (\bar{C}_{13}\varepsilon_x^T + \bar{C}_{23}\varepsilon_y^T + \bar{C}_{33}\varepsilon_z^T + \bar{C}_{36}\gamma_{xy}^T)g$$

$$T_{10} = (\bar{C}_{11}\varepsilon_x^T + \bar{C}_{12}\varepsilon_y^T + \bar{C}_{13}\varepsilon_z^T + \bar{C}_{16}\gamma_{xy}^T)A^{\ell}$$

where

$$\varepsilon_x^T = (m^2\alpha_1 + n^2\alpha_2)\Delta T$$

$$\varepsilon_y^T = (n^2\alpha_1 + m^2\alpha_2)\Delta T$$

$$\varepsilon_z^T = \alpha_3\Delta T$$

$$\gamma_{xy}^T = 2mn(\alpha_1-\alpha_2)\Delta T$$

For moisture analysis the vector {T} is identical except α_1, α_2 and α_3 are replaced by β_1, β_2 and β_3.

APPENDIX C

TENSOR POLYNOMIAL FAILURE CRITERION

APPENDIX C

TENSOR POLYNOMIAL FAILURE CRITERION

The tensor polynomial failure criterion in the contracted tensor notation (for an orthotropic material in the principal material directions) has the form

$$\begin{aligned} &F_1\sigma_1+F_2\sigma_2+F_3\sigma_3+F_{11}\sigma_1^2+F_{22}\sigma_2^2 \\ &+F_{33}\sigma_3^2+F_{44}\tau_{23}^2+F_{55}\tau_{13}^2+F_{66}\tau_{12}^2 \\ &+2F_{12}\sigma_1\sigma_2+2F_{13}\sigma_1\sigma_3+2F_{23}\sigma_2\sigma_3 = 1 \end{aligned} \tag{C.1}$$

where the F_i and F_{ij} terms are as previously defined in Chapter 3. In the xyz (laminate) coordinate system, the tensor polynomial failure criterion transforms (from the 1-2 to x-y by anticlockwise rotation of $+\theta$) into

$$\begin{aligned} &F'_1\sigma_x+F'_2\sigma_y+F'_3\sigma_z+F'_6\sigma_{xy}+F'_{11}\sigma_x^2 \\ &+F'_{22}\sigma_y^2+F'_{33}\sigma_z^2+F'_{44}\tau_{yz}^2+F'_{55}\tau_{xz}^2 \\ &+F'_{66}\tau_{xy}^2+2F'_{16}\sigma_x\tau_{xy}+2F'_{26}\sigma_y\tau_{xy} \\ &+2F'_{36}\sigma_z\tau_{xy}+2F'_{45}\tau_{yz}\tau_{xz}+2F'_{12}\sigma_x\sigma_y \\ &+2F'_{13}\sigma_x\sigma_z+2F'_{23}\sigma_y\sigma_z = 1 \end{aligned} \tag{C.2}$$

where the F' terms, as functions of the unprimed F's and θ, are as follows ($m = \cos\theta$, $n = \sin\theta$)

$$F'_1 = m^2F_1+n^2F_2$$

$$F'_2 = n^2F_1+m^2F_2$$

$$F'_3 = F_3$$

$$F'_6 = -2mn(F_1-F_2)$$

$$F'_{11} = m^4F_{11}+m^2n^2(F_{66}+2F_{12})+n^4F_{22}$$

$$F'_{22} = n^4F_{11}+m^2n^2(F_{66}+2F_{12})+m^4F_{22}$$

$$F'_{33} = F_{33}$$

$$F'_{44} = m^2F_{44}+n^2F_{55}$$

$$F'_{55} = n^2F_{44}+m^2F_{55}$$

$$F'_{66} = 4m^2n^2(F_{11}+F_{22}-2F_{12})+(m^2-n^2)^2F_{66}$$

$$F'_{16} = -mn[2(m^2F_{11}-n^2F_{22})-(m^2-n^2)(2F_{12}+F_{66})]$$

$$F'_{26} = -mn[2(n^2F_{11}-m^2F_{22})+(m^2-n^2)(2F_{12}+F_{66})]$$

$$F'_{36} = -mn(F_{13}-F_{23})$$

$$F'_{45} = mn(F_{44}-F_{55})$$

$$F'_{12} = m^2n^2(F_{11}+F_{22}-F_{66})+(m^4+n^4)F_{12}$$

$$F'_{13} = m^2F_{13}+n^2F_{23}$$

$$F'_{23} = n^2F_{13}+m^2F_{23}$$

These are transformations from the right handed 1-2 coordinate system into another right hand coordinate system obtained by an anticlockwise rotation of $\theta°$ about the 3 axis. If a ply is oriented at $+\theta°$ from the laminate axis, the F_{ij} are obtained by using the above equations with the sines and cosines of $-\theta°$.

APPENDIX D

USERS GUIDE FOR NONCOM 3

(Available upon request)

APPENDIX E

FINITE ELEMENT MESHES

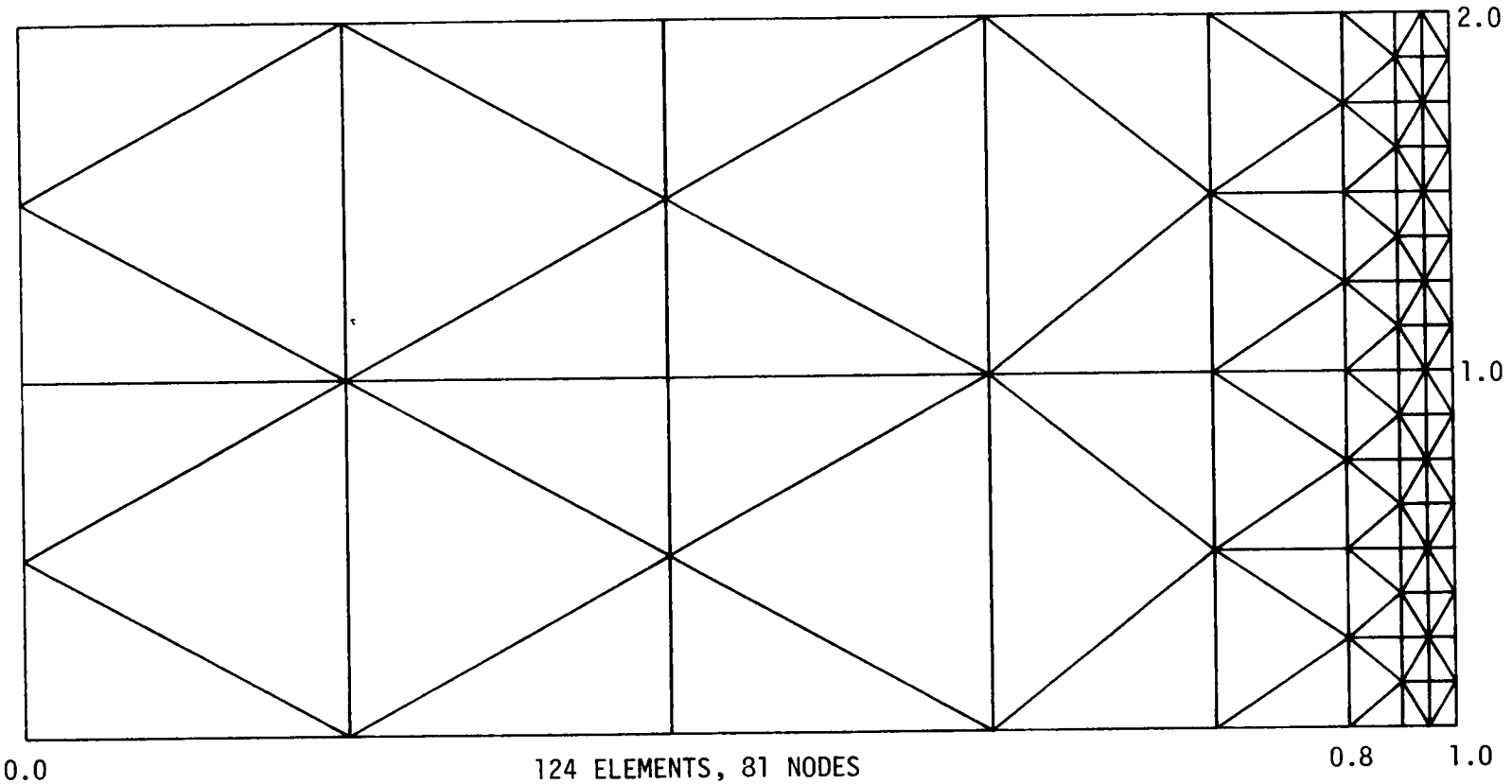

FIGURE E1. MESH E1

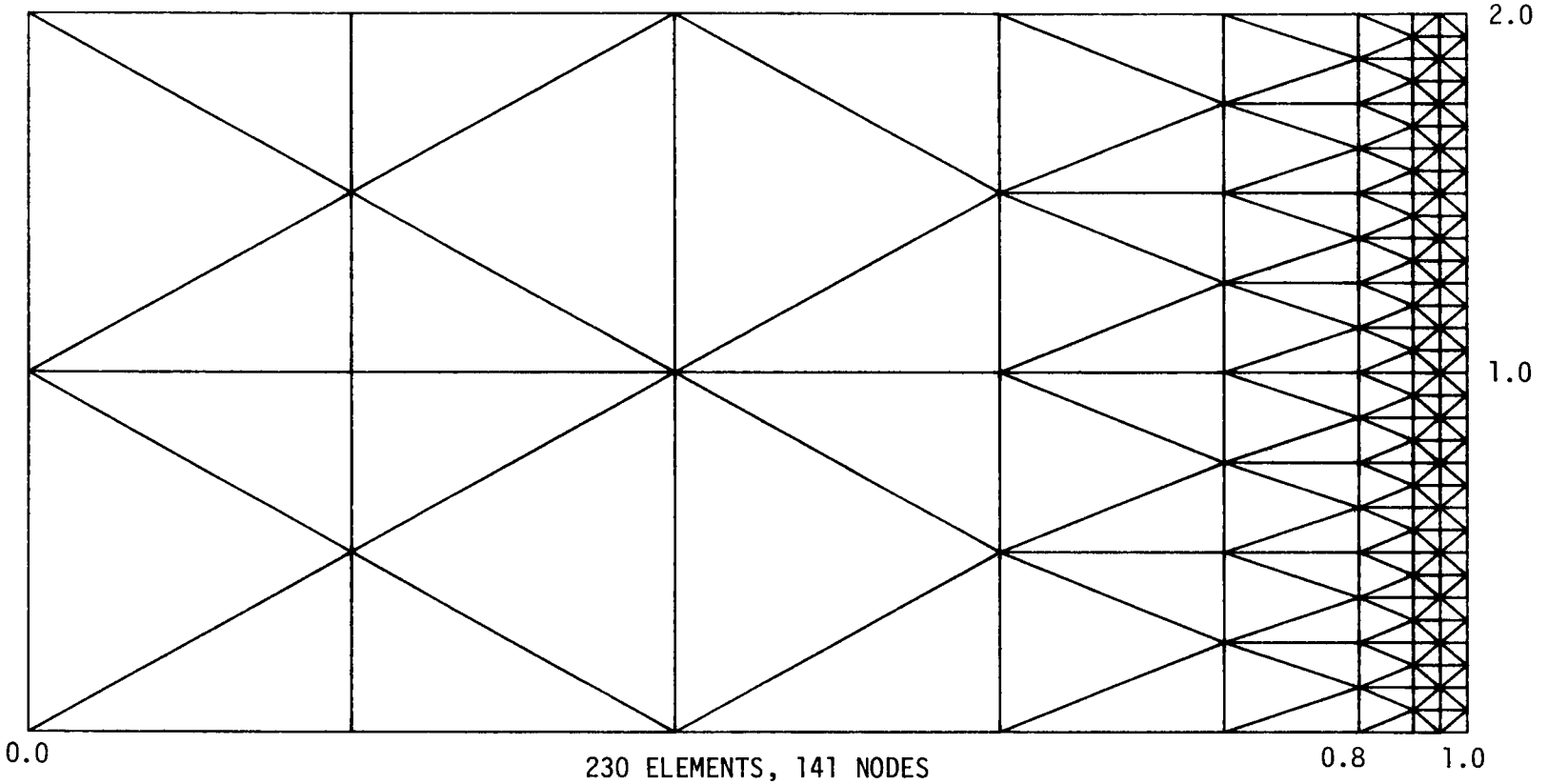

FIGURE E2. MESH E2

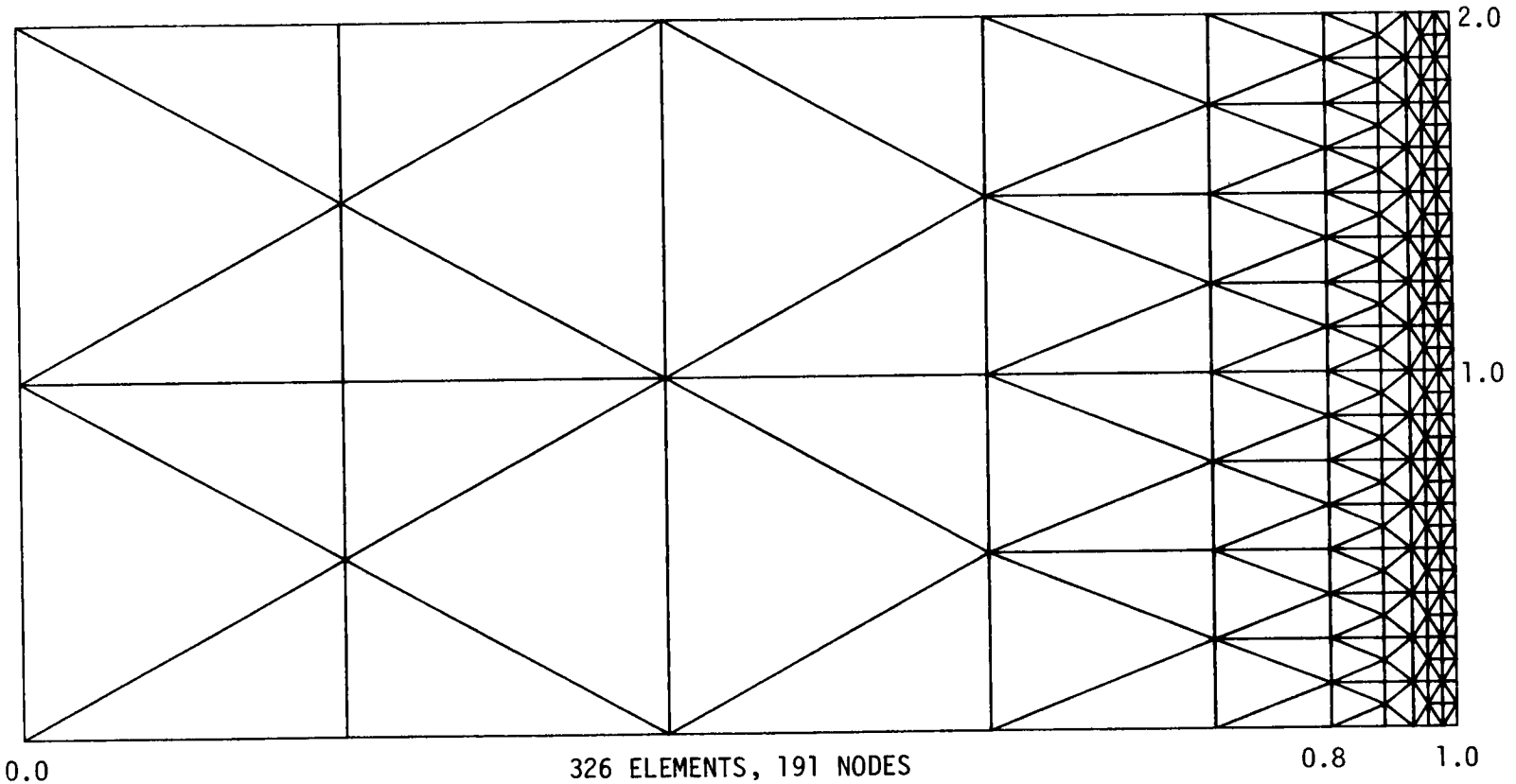

FIGURE E3. MESH E3

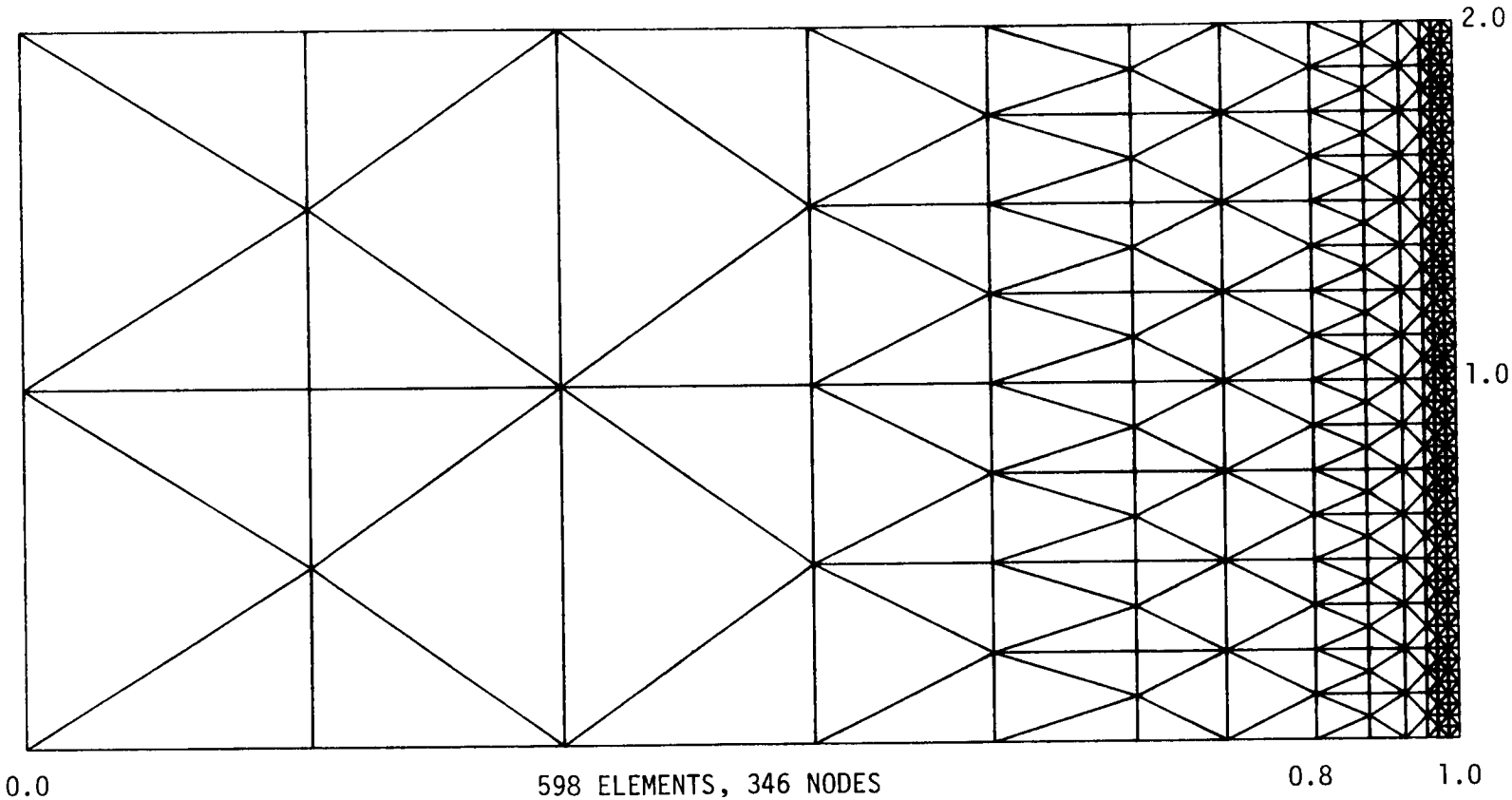

FIGURE E4. MESH E4

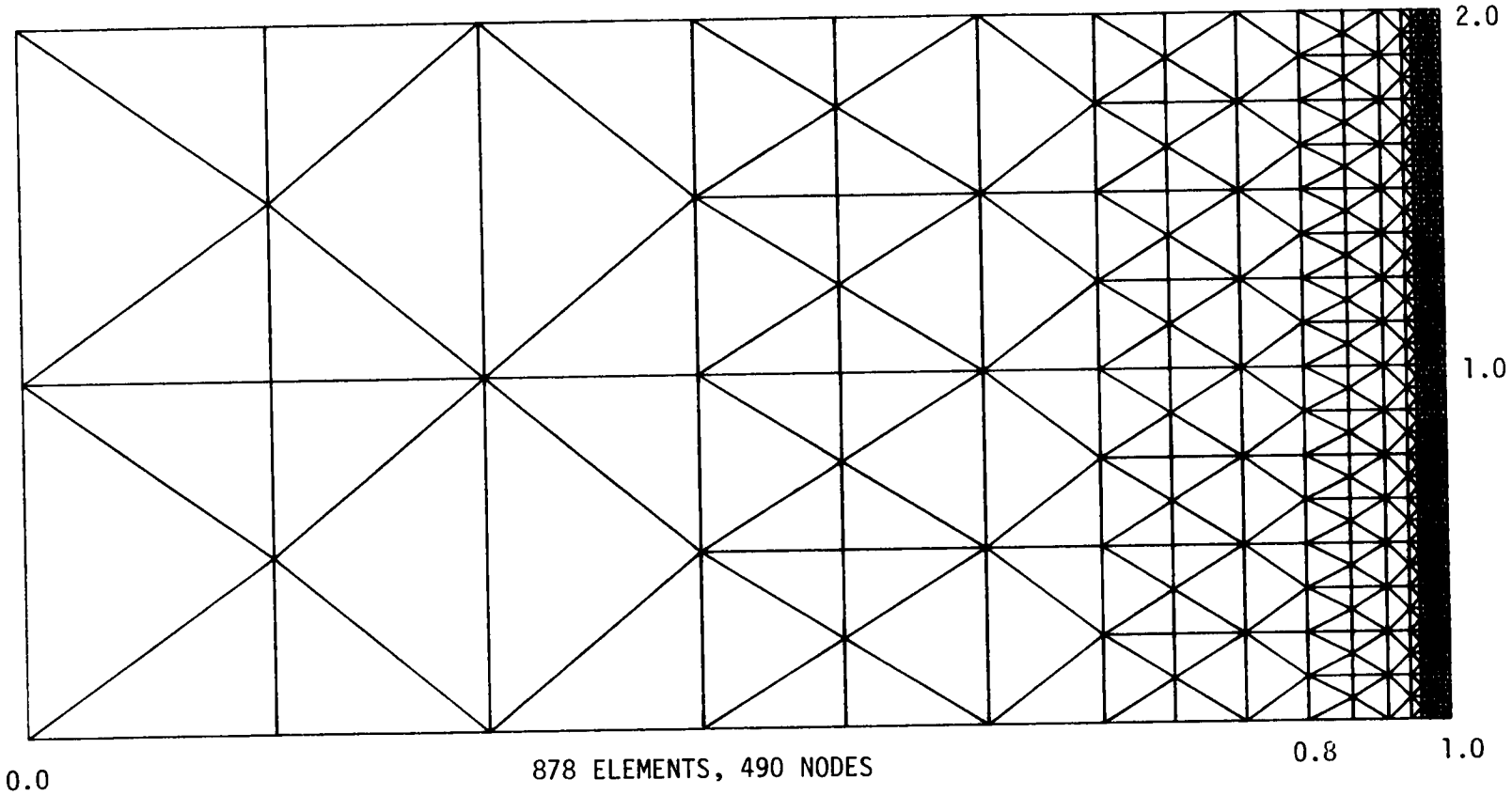

FIGURE E5. MESH E5

APPENDIX F

NONCOM3 FLOW CHART

NONCOM3 FLOW CHART

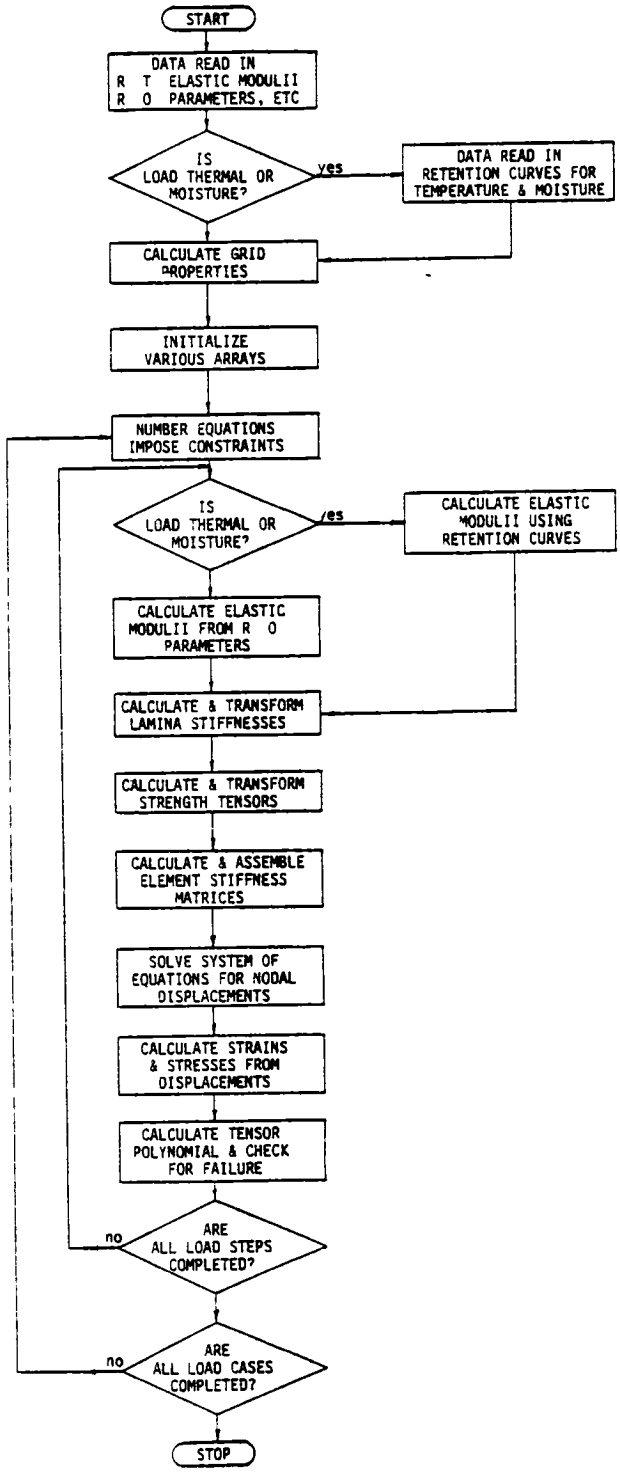

APPENDIX G

T300/5208 GRAPHITE-EPOXY PROPERTIES

TABLE G.1 Ramberg-Osgood parameters for graphite epoxy T300/5208

Curve	Elastic Modulus (MSI)	Elastic Limit (KSI)	n_1	$K_1(PSI^{-n_1})$	σ^* (KSI)	n_2	$K_2(PSI^{-n_2})$
E_{11}^T	19.2	90	2.593	$.14792 \times 10^{-16}$	-	-	-
E_{11}^C	19.2	87	2.037	$.30754 \times 10^{-13}$	-	-	-
E_{22}^T	1.56	6.3	0	$.10000 \times 10^{1}$	-	-	-
E_{22}^C	1.56	13.5	1.068	$.13324 \times 10^{-7}$	-	-	-
E_{33}^T	1.56	6.3	0	$.10000 \times 10^{1}$	-	-	-
E_{33}^C	1.56	13.5	1.068	$.13324 \times 10^{-7}$	-	-	-
G_{23}	.487	2.1	1.147	$.81419 \times 10^{-7}$	2.82	4.668	1.6842×10^{-21}
G_{13}	.82	3.5	1.147	$.44882 \times 10^{-7}$	2.82	4.688	1.6842×10^{-21}
G_{12}	.82	3.5	1.147	$.44882 \times 10^{-7}$	2.82	4.688	1.6842×10^{-21}

TABLE G.2 Hygrothermal properties for graphite epoxy T300/5208

Property	Room Temp. 0% Moisture -Elastic Modulus- (Msi)	Percent Retention of Room Temp., 0% Moisture Property								
		Temperature 70° F			Temperature 260° F			Temperature 350° F		
		Percent Weight Gain			Percent Weight Gain			Percent Weight Gain		
		0.00	0.83	1.13	0.00	0.83	1.13	0.00	0.83	1.13
E_{11}^{T}	19.2	100.0	84.1	84.1	107.3	-	85.4	112.2	-	91.0
E_{11}^{C}	19.2	100.0	91.1	80.8	97.8	84.7	-	96.4	-	-
E_{22}^{T}	1.56	100.0	88.2	92.1	93.4	-	100.0	79.3	-	-
E_{22}^{C}	1.56	100.0	-	-	-	-	-	-	-	-
E_{33}^{T}	1.56	100.0	88.2	92.1	93.4	-	100.0	79.3	-	94.9
E_{33}^{C}	1.56	100.0	-	-	-	-	-	-	-	-
G_{23}	.487	100.0	93.9	89.0	96.2	-	75.1	85.4	-	81.1
G_{13}	.82	100.0	93.9	89.0	96.2	-	75.1	85.4	-	81.1
G_{12}	.82	100.0	93.9	89.0	96.2	-	75.1	85.4	-	81.1

TABLE G.2 continued

Property	Room Temp. 0% Moisture -Strength- (ksi)	Percent Retention of Room Temp., 0% Moisture Property								
		Temperature 70° F			Temperature 260° F			Temperature 350° F		
		Percent Weight Gain			Percent Weight Gain			Percent Weight Gain		
		0.00	0.83	1.13	0.00	0.83	1.13	0.00	0.83	1.13
X_T	219.5	100.0	95.5	86.6	96.8	81.0	88.4	93.8	67.6	77.8
X_C	-246.0	100.0	94.3	96.4	92.1	90.7	96.0	88.5	-	-
Y_T	6.35	100.0	79.3	97.9	69.1	44.8	47.3	48.9	24.5	46.3
Y_C	-23.85	100.0	-	-	78.3	75.5	-	74.7	57.3	80.9
Z_T	6.35	100.0	79.3	97.9	69.1	44.8	47.3	48.7	24.5	46.3
Z_C	-23.85	100.0	-	-	78.3	75.5	-	74.7	57.3	80.9
S_{23}	9.8	100.0	132.0	132.0	76.1	81.2	90.6	64.6	75.2	87.2
S_{13}	12.6	100.0	132.0	132.0	76.1	81.2	90.6	64.6	75.2	87.2
S_{12}	12.6	100.0	132.0	132.0	76.1	81.2	90.6	64.6	75.2	87.2

TABLE G.2 continued

Property	Room Temp. 0% Moisture -ν-	Percent Retention of Room Temp., 0% Moisture Property								
		Temperature 70° F			Temperature 260° F			Temperature 350° F		
		Percent Weight Gain			Percent Weight Gain			Percent Weight Gain		
		0.00	0.83	1.13	0.00	0.83	1.13	0.00	0.83	1.13
ν_{23}^{T}	0.49	100.0	-	89.5	81.6	-	-	68.4	-	-
ν_{23}^{C}	0.49	100.0	-	-	78.9	-	-	81.6	-	-
ν_{13}^{T}	0.238	100.0	-	89.5	81.6	-	-	68.4	-	-
ν_{13}^{C}	0.24	100.0	-	-	78.9	-	-	81.6	-	-
ν_{12}^{T}	0.238	100.0	-	89.5	81.6	-	-	68.4	-	-
ν_{12}^{C}	0.24	100.0	-	-	78.9	-	-	81.6	-	-

TABLE G.2 continued

Property	Room Temp. 0% Moisture -Temperature Coefficient- (μin/in/°F)	Temperature Coefficient (μin/in/°F)								
		Temperature 70° F			Temperature 260° F			Temperature 350° F		
		Percent Weight Gain			Percent Weight Gain			Percent Weight Gain		
		0.00	0.83	1.13	0.00	0.83	1.13	0.00	0.83	1.13
α_1	0.193	0.193	-	-	0.226	-	-	0.226	-	-
α_2	13.8	13.8	-	-	13.8	-	-	13.8	-	-
α_3	13.8	13.8	-	-	13.8	-	-	13.8	-	-

α_1 has the value 0.193 from room temperature to 120°F and 0.226 from 120°F to 350°F.

TABLE G.2 continued

Property	Room Temp. 0% Moisture -Moisture Coefficient- (in/in/%Wt)	Moisture Coefficient (in/in/%Wt Gain)								
		Temperature 70° F			Temperature 260° F			Temperature 350° F		
		Percent Weight Gain			Percent Weight Gain			Percent Weight Gain		
		0.00	0.83	1.13	0.00	0.83	1.13	0.00	0.83	1.13
β_1	0.0	0.0	0.0	0.0	-	-	-	-	-	-
β_2	0.0	0.0	0.0049	0.0061	-	-	-	-	-	-
β_3	0.0	0.0	0.0049	0.0061	-	-	-	-	-	-

DISTRIBUTION LIST

Prof. Donald F. Adams
Dept. Of Mechanical Engineering
University Of Wyoming
Larmie, WY 82070

Dr. N. R. Adsit
General Dynanics Convair
P.O. Box 80837
San Diego, CA. 92138

Dr. J. A. Bailie
D81-12 Bldg. 154
Lockheed Missiles & Space Co,Inc
1111 Lockheed Way
Sunnyvale, CA. 94088

Mr. Henry W. Bergner, Jr.
The Boeing Company
Mail Stop 3707
Seattle, WA. 98124

Dr. Charles W. Bert, Director
School Of Aerospace, Mechanical
& Nuclear Engineering
The University Of Oklahoma
Norman, Oklahoma 73069

Mr. Richard Boitnott
Mail Stop 190
Nasa-Langley Research Center
Hampton, VA. 23665

Mr. David Bowles
Mail Stop 188B
NASA-Langley Research Center
Hampton, Va. 23665

Dr. H. F. Brinson
ESM Dept.
Virginia Tech
Blacksburg, VA. 24061

Mr. Ernie Brooks
ESM Dept.
Virginia Tech
Blacksburg, VA. 24061

Dr. Micharl F. Card
Mail Stop 190
NASA-Langley Research Center
Hampton, VA 23665

Dr. C. Chamis
NASA-Lewis Research Center
2100 Brook Park Rd.
Cleveland, Ohio 44135

Dr. Paul A. Cooper
Mail Stop 190
NASA-Langley Research Center
Hampton, Va. 23665

Dr. Frank Crossman
Lockheed Research Lab
Org. 52-41, Bldg. 204
3251 Hanover Street
Palo Alto, CA. 94304

Dr. I. M. Daniel, Manager
IIT Research Institute
10 West 35 Street
Chicago, IL. 60616

Dr. John R. Davidson
Mail Code 188E
MD-Structural Integrity Branch
Langley Research Center
Hampton, VA. 23665

Dr. John G. Davis, Jr.
Mail Stop 188A
Langley Research Center
Hampton, VA. 23665

Mr. Jerry W. Deaton
Mail Stop 188A
NASA-Langley Research Center
Hampton, VA. 23665

Mr. H. Benson Dexter
Mail Stop 188A
NASA-Langley Research Center
Hampton, VA. 23665

Mr. O. Earl Dhonau
Section 2-53400
Vought Corp.
P.O. Box 5907
Dallas, TX. 75222

Dr. S. C. Dixon
Mail Stop 395
NASA-Langley Research Center
Hampton, VA. 23665

Dr. J. E. Duberg
Mail Stop 103
NASA-Langley Research Center
Hampton, Va. 23665

Dr. M. F. Duggan
52-33/205/2
Lockheed Palo Alto Lab.
3251 Hanover St.
Palo Alto, Ca. 94304

Dr. Wolf Elber
Mail Stop 188E
NASA-Langley Research Center
Hampton, VA. 23665

Mr. Dave Erb
Aero & Ocean Engr. Dept.
Virginia Tech
Blacksburg, VA. 24061

Mr. Gary L. Farley
Mail Stop 188A
NASA-Langley Research Center
Hampton, VA. 23665

Mr. Larry Fogg
Lockheed-California
Dept. 7572, Bldg. 63, Plant A1
P.O. Box 551
Burbank, CA. 91520

Dr. R. L. Foye
USAMRDL
SAUDLAS (207-5)
Moffet Field, CA. 94035

Dr. D. Frederick
ESM Dept.
Virginia Tech
Blacksburg, VA. 24061

Mr. Samuel P. Garbo
McDonnell Aircraft Co.
Bldg. 34, Post 350
St. Louis, MO. 63166

Mr. Ramon Garica
Mail Stop 190
NASA-Langley Research Center
Hampton, VA. 23665

Prof. Jim Goree
Dept. of Mechanical Engr.
Clemson University
Clemson, S.C. 29631

Dr. Login B. Greszczuk
McDonnell Douglas Astr. Co.
5301 Bolas Avenue
Huntington Beach, CA. 92647

Mr. Glen C. Grimes, Engr. Spec.
Structures R & T, Dept 3780/62
Northrop Corp., Aircraft Div.
3901 W. Broadway
Hawthorne, CA. 90250

Dr. H. T. Hahn
Washington University
St. Louis, MO. 63130

Dr. J. C. Halpin
Flight Dynamics Lab
Wright-Patterson AFB
Ohio 45433

Professor Z. Hashin
School of Engineering
Solid Mech. Materials & Struc.
Tel Aviv University
Tel Aviv, Israel

Dr. R. A. Heller
ESM Dept.
Virginia Tech
Blacksburg, VA. 24061

Dr. E. G. Henneke
ESM Dept.
Virginia Tech
Blacksburg, VA. 24061

Professor Phil Hodge
107 Aeronautical Engr. Bldg.
University of Minnesota
Minneapolis, MN 55455

Dr. K. E. Hofer
IIT Research Institute
10 West 35 Street
Chicago, Illinois 60616

Mr. Edward L. Hoffman
Mail Stop 188A
NASA-Langley Research Center
Hampton, VA. 23665

Dr. Peter W. Hsu
Mail Stop 1-1-12
Hamilton Standard Division
Windsor Locks, CT. 06096

Mr. Edward A. Humphreys
Materials Science Corporation
Blue Bell Office Campus
Blue Bell, PA. 19422

Dr. Michael W. Hyer
ESM Dept.
Virginia Tech
Blacksburg, VA. 24061

AVCO, Systems Division
Subsystems & Meth. Structures
201 Lowell Street
Wilmington, MA. 01887

Dr. Eric R. Johnson
ESM Dept.
Virginia Tech
Blacksburg, VA. 24061

Dr. N. J. Johnson
Mail Stop 226
NASA-Langley Research Center
Hampton, VA. 23665

Dr. M. P. Kamat
ESM Dept.
Virginia Tech
Blacksburg, VA. 24061

Dr. Keith T. Kedward
1768 Granite Hills Dr.
El Cajon, CA. 92021

Mr. John M. Kennedy
Mail Stop 188E
NASA-Langley Research Center
Hampton, VA. 23665

Mr. Eric Klang
1313 Rosemary
Columbia, MO. 65201

Mr. James F. Knauss
Section 2-30400
Vought Corp.
P.O. Box 225907
Dallas, TX. 75265

Dr. Ronald D. Kriz
Dept. Com. NBS Bldg. 2
Boulder, CO. 80302

Dr. S. V. Kulkarni
L342 Lawrence Livermore Lab
P. O. Box 808
Livermore, Ca. 94550

Dr. M. R. Louthan
Materials Engineering
Virginia Tech
Blacksburg, VA. 24061

Mr. Vic Mazzio
General Electric Co.
P.O. Box 8555
Bldg. 100, Rm. M4018
Philadelphia, PA. 19101

Mr. Robert R. McWithey
Mail Stop 190
NASA-Langley Research Center
Hampton, VA. 23665

Dr. Martin M. Mikulas
Mail Stop 190
NASA-Langley Research Center
Hampton, VA. 23665

Mr. J. Steve Mills
6100 Edinger Ave., Apt. 525
Huntington Beach
CA 92647

Dr. D. H. Morris
ESM Dept.
Virginia Tech
Blacksburg, VA. 24061

Mr. Anya Nagarkar
Material Sciences Corp.
Blue Bell Office Campus
Blue Bell, PA. 19422

NASA Scientific & Technical
Information Facility
P.O. Box 8757
Baltimore/Washington Inter. Air.
Baltimore, MD. 21240

Mr. Michael Nemeth
ESM Dept.
Virginia Tech
Blacksburg, VA. 24061

Newman Library - Virginia Tech

Mr. David A. O'Brien
5902 Kingsford Pl.
Bethesda, MD 20034

Dr. Donald W. Oplinger
Army Materials & Mechanics
Research Center
Department of the Army
Watertown, MA. 02171

Dr. Nicholas J. Pagano
WPAFB/MBM
Wright Patterson AFB
Ohio 45433

Mr. Michael Parin
3M Co., 3M Center
Bldg. 230-1F
St. Paul, MN. 55101

Dr. Nicholas Perrone, Director
Structural Mechanics Program
Department of the Navy
Office of Naval Research
Arlington, VA. 22217

Prof. T. H. H. Pian
Mass. Inst. of Tech.
Dept. of Aero. & Astr.
Cambridge, MA. 02139

Mr. Marek-Jerzy Pindera
Mail Stop 188A
NASA-Langley Research Center
Hampton, VA. 23665

Dr. R. Byron Pipes
Dept. of Mech. & Aero. Engr.
107 Evans Hall
University of Delaware
Newark, DE. 19711

Prof. Robert Plunkett
Aero 107
University of Minnesota
Minneapolis, MN. 55455

Dr. K. L. Reifsnider
ESM Dept.
Virginia Tech
Blacksburg, VA. 24061

Dr. Gary D. Renieri
McDonnell Douglas Astro. Co-East
P.O. Box 516
Bldg. 106, Level 4, Post C-5
St. Louis, MO. 63166

Dr. Michael W. Renieri
McDonnell Aircraft Co.
Bldg. 34, Post 350
St. Louis, MO. 63166

Dr. Larry Roderick
Mail Stop 188E
NASA-Langley Research Center
Hampton, VA. 23665

Dr. B. W. Rosen
Materials Science Corporation
Blue Bell Office Campus
Blue Bell, PA. 19422

Dr. R. E. Rowlands
Dept. of Engineering Mechanics
University of Wisconsin
Madison, WI. 53706

Dr. Edmund F. Rybicki
Battelle
Columbus Laboratories
505 King Avenue
Columbus, OH. 43201

Mr. Harminder Saluja
Boeing Vertol Company
Structural Technology
P.O. Box 16858
Philadelphia, PA. 19142

Dr. J. Wayne Sawyer
Mail Stop 190
NASA-Langley Research Center
Hampton, VA. 23665

Dr. George P. Sendeckyj
Structures Division
Air Force Flight Dynamics Lab.
Wright-Patterson AFB
Ohio 45433

Mr. Steven M. Serabian
28 Berkeley Drive
Chelmsford, MA. 01824

Mr. John S. Short, Jr.
1223 Pond Street
Cary, N.C.

Mr. Mark J. Shuart
Mail Stop 188
NASA-Langley Research Center
Hampton, VA. 23665

Dr. James H. Starnes, Jr.
Mail Stop 190
NASA-Langley Research Center
Hampton, VA. 23665

Prof. Yehuda Stavsky
Gerard Swope Prof. of Mech.
Technion-Israel Inst. of Tech.
Technion City, Haifa, Israel

Dr. W. W. Stinchcomb
ESM Dept.
Virginia Tech
Blacksburg, VA. 24061

Dr. Darrel R. Tenney
Mail Code 188B
MD-Materials Research Branch
Langley Research Center
Hampton, VA. 23665

Dr. S. W. Tsai
Nonmetallic Materials Division
Air Force Materials Laboratory
Wright-Patterson AFB
Ohio 45433

Dr. J. R. Vinson
6242 Urey Hall
Applied Mechanics & Science Dept
Univ. of California-San Diego
La Jolla, CA. 92037

Mr. M. E. Waddoups
General Dynamic Corp.
Fort Worth, TX 76101

Dr. T. A. Weisshaar
Aero & Ocean Engr. Dept.
Virginia Tech
Blacksburg, VA. 24061

Dr. J. M. Whitney
Nonmetallic Materials Division
Air Force Materials Laboratory
Wright-Patterson AFB
Ohio 45433

Dr. Ernest G. Wolff
The Aerospace Corp.
P.O. Box 92957
Los Angeles, CA. 90009

Mr. Thomas A. Zeiler
Aerospace Engr.
Virginia Tech
Blacksburg, VA. 24061

Dr. Carl H. Zweben
General Electric Co.
Space Division
P.O. Box 8555
Philadelphia, PA. 19101

End of Document